Development of the DEPICT System for Gamma-ray Imaging in Molecular Radiotherapy

Thesis submitted in accordance with the requirements of

the University of Liverpool for the degree of Doctor of Philosophy

by

Lucy H. McAreavey

Oliver Lodge Laboratory

July 2019

Acknowledgements

Firstly, a massive thank you goes to Dr Laura Harkness-Brennan. I could not have asked for a better supervisor. It was your encouragement and support that made this thesis possible. A huge thank you also goes to those that helped along the way; Drs. Helen Boston, Andy Boston, Samantha Colosimo, Prof. Paul Nolan and especially Dr. Dan Judson - the Nuclear Physics group would fall apart without you!

I loved my time as a PhD student and that was no doubt down to the other students in the department. Thank you for daily crossword breaks and many, many pub trips. A special mention has to go to Tadam and Ellis. I think we have come a long way since the 'how do I open my macbook?' incident...

To those that mean the most to me - Mum, Dad and Beth, your unending love and support means so much and I will never be able to thank you enough, and Calvin, I would never have got through those last few months if it weren't for you. Thank you for always looking after me.

A final special mention has to go to Barry King. Thank you for making me believe I was good enough to do a PhD; I wish you could have been there at the end to celebrate.

Abstract

The development and evaluation of a gamma-ray imaging system for dosimetry of Molecular Radiotherapy (MRT) is presented. MRT is a cancer treatment that aims to deliver high radiation doses to targeted tumour or disease sites, with minimal dose to surrounding healthy tissue. This is achieved through the administration of radiopharmaceuticals, typically with a fixed activity or adjusted for patient weight or body surface area. These activities are often several gigabecquerels (GBq). The administered radionuclide decays via the emission of charged particles which damage the cancerous or diseased cells, ideally alongside gamma rays that can be used to image the distribution of the radiopharmaceutical. The absorbed dose in regions of interest can then be calculated by extracting activity from these images. However, the energy resolution, spatial resolution and count rate performance of current clinical gamma-ray imaging systems result in inaccurate activity calculations. The Dosimetric Imaging with Cadmium Zinc Telluride (DEPICT) project aims to overcome these performance limitations through the development of an optimised gamma camera system, configured with a 3D printed tungsten collimator and Cadmium Zinc Telluride (CZT) detectors. This thesis focuses on the optimisation of the DEPICT system for ^{131}I, which is used for MRT treatment of the thyroid. This will provide improved verification of these treatments and information that allows subsequent personalisation of the otherwise generic treatment plans. A pixelated CZT detector was selected because of its excellent energy resolution and spatial resolution. The DEPICT CZT detector was characterised and an experimental study undertaken to optimise the energy resolution and throughput of gamma rays. The optimum energy resolution at 364.5 keV was shown to be 2.94% for a maximum count rate of 160 kcps. A 3D printed high-energy parallel-hole tungsten collimator suitable for imaging the 364.5 keV gamma rays from ^{131}I was developed. Experimental data were acquired with medical phantoms to determine the imaging capability DEPICT, as accurate area delineation is necessary for measurements of activity within a region of interest. The spatial resolution of DEPICT was shown to be

2 mm, which is superior to 13.4 mm for clinical systems that are configured with high-energy collimators. Methodology for quantifying the sizes of artefacts in an image are described. The experimental performance of DEPICT for imaging ^{131}I distributed in a thyroid phantom was shown to surpass that of a clinical Siemens gamma camera. It was possible to identify regions of interest in the DEPICT thyroid phantom image that were not visible in the clinical image, due to the improved spatial and energy resolution. Quantification of the activity in vials containing ^{131}I has been achieved using DEPICT to within 9% of the known activity for data acquired with 1 vial and 3% for data with 3 vials. Distributed sources have also been visualised in 3D using tomography, to show the capability of accurately reconstructing volumes of interest. The future of MRT relies on the development of innovative radiopharmaceuticals. The radionuclides ^{177}Lu, ^{111}In, ^{223}Ra and ^{227}Th are being increasingly considered in MRT and have been investigated in this thesis through acquisition of experimental gamma-ray spectra. Monte-Carlo simulations have been developed so that modifications to the DEPICT system can be recommended for imaging radionuclides other than ^{131}I.

Contents

List of Figures

List of Tables

List of Publications

Peer Reviewed Papers

L.H. McAreavey, L.J. Harkness-Brennan, S.J. Colosimo, D.S. Judson, A.J. Boston, H.C. Boston, P.J. Nolan, G.D. Flux, A.M. Denis-Bacelar, B. Harris, I. Radley and M. Carroll, Characterisation of a CZT Detector for Dosimetry of Molecular Radiotherapy, *Journal of Instrumentation*, Vol. 12, March 2017.

L.H. McAreavey, L.J. Harkness-Brennan, S.J. Colosimo, D.S. Judson, A.J. Boston, H.C. Boston, P.J. Nolan, G.D. Flux, A.M. Denis-Bacelar, B. Harris, I. Radley and M. Carroll, Developing a Gamma Camera System for Dosimetry of Radionuclide Therapy, *Nuclear Future*, Volume 13 Issue 6, December 2017.

Oral Presentations

L.H. McAreavey, L.J. Harkness-Brennan, S.J. Colosimo, D.S. Judson, A.J. Boston, H.C. Boston, P.J. Nolan, G.D. Flux, A.M. Denis-Bacelar, B. Harris, I. Radley and M. Carroll, Characterisation of a CZT Detector for Dosimetry of Molecular Radiotherapy, *24^{th} International Conference on the Application of Accelerators in Research and Industry (CAARI) book of abstracts*, Fort Worth, Texas, November 2016.

L.H. McAreavey, L.J. Harkness-Brennan, S.J. Colosimo, D.S. Judson, A.J. Boston, H.C. Boston, P.J. Nolan, G.D. Flux, A.M. Denis-Bacelar, B. Harris, I. Radley and M. Carroll, Characterisation of a CZT Detector for Dosimetry of Molecular Radiotherapy, *17th AGATA week and First Position Sensitive Germanium Detectors and Application Workshop*, Orsay, France, October 2016.

L.H. McAreavey, L.J. Harkness-Brennan, S.J. Colosimo, D.S. Judson, A.J. Boston, H.C. Boston, P.J. Nolan, G.D. Flux, A.M. Denis-Bacelar, B. Harris, I. Radley and M. Carroll, The DEPICT Project - Developing a gamma camera system for dosimetry of molecular radiotherapy, *IOP Nuclear Physics Conference*, Paisley, Scotland, April 2018.

L.H. McAreavey, L.J. Harkness-Brennan, D.S. Judson, S.J. Colosimo, A.J. Boston, H.C. Boston, P.J. Nolan, G.D. Flux, A.M. Denis-Bacelar, B. Harris, I. Radley and M. Carroll, Development of a Quantitative Gamma-Camera System for Molecular Radiotherapy Dosimetry, *2018 IEEE Nuclear Science Symposium and Medical Imaging Conference*, Sydney, Australia, November 2018.

Acronyms

ADC Analogue to Digital Converter.

ASIC Application Specific Integrated Circuit.

CZT Cadmium Zinc Telluride.

DEPICT Dosimetric Imaging with Cadmium Zinc Telluride.

EBRT External Beam Radiotherapy.

FDA Food and Drug Administration.

FOV Field of View.

FPGA Field Programmable Gate Array.

FWHM Full Width at Half Maximum.

GAMOS Geant4-based Architecture for Medicine-Oriented Simulations.

IRD Internal Radiation Dosimetry.

LET Linear Energy Transfer.

LSF Line Spread Function.

MIRD Medical Internal Radiation Dose.

MLEM Maximum Likelihood Expectation Maximisation.

MRT Molecular Radiotherapy.

OSEM Ordered Subset Expectation Maximisation.

PET Positron Emission Tomography.

SPECT Single Photon Emission Computed Tomography.

TAC Time-Activity Curve.

Chapter 1

Introduction

Molecular Radiotherapy (MRT) is a cancer treatment technique that involves the internal administration of radiopharmaceuticals to deliver high absorbed doses to targeted tumour tissue, whilst minimising the dose to surrounding healthy tissue. Although MRT has been used clinically for around 75 years, there are no standardised dosimetry practises to calculate the absorbed dose delivered to tumour or benign disease targets, or the surrounding organs at risk from the administered activity. Current MRT treatment plans are undesirably generic as the administered activity is often fixed for a given procedure or scaled according to the weight or body surface area of the patient [1]. However, the uptake and retention of the MRT therapeutic agents and hence the absorbed dose can vary by up to two orders of magnitude between patients [2, 3], due to the wide range of biokinetics and disease status. The outcome of the treatment is therefore somewhat uncertain and can lead to unnecessary expense.

The archetypal example of MRT is the radioiodine (^{131}I) treatment of thyroid cancer and diseases. The efficacy of MRT is evaluated through knowledge of absorbed dose and this is ideally calculated through accurate real-time quantitative imaging of the ^{131}I distribution in the patient. Single Photon Emission Computed Tomography (SPECT) is the modality that is used to image the 364.5 keV gamma rays emitted by ^{131}I. Uncertainties arise however, as clinical diagnostic SPECT systems are not optimised for imaging the high activities administered in ^{131}I MRT (typically 1.1 – 7.4 GBq) and therefore suffer from count rate saturation. A further inadequacy of these systems for dosimetry is the image quality arising from poor spatial and energy resolution of the collimated detector system, and from the scattering of the gamma rays as they leave the body of the patient or interact within the collimator. Therefore,

a custom gamma-ray imaging system has been developed to overcome these limitations. The detector system discussed in this thesis is based on Cadmium Zinc Telluride (CZT) room temperature semiconductor detectors with Application Specific Integrated Circuit (ASIC) readout. The good energy resolution of CZT will facilitate excellent scatter correction and the detector pixelation will allow high count rate operation and improved spatial resolution compared to current clinical gamma cameras used in SPECT. The detector is coupled to a high-resolution, low-efficiency parallel-hole collimator that is optimised for imaging the high-energy gamma rays from ^{131}I. This custom-designed collimator will improve count rate saturation and overcome some of the factors that degrade image quality. The collimated detector system will be used to accurately calculate cumulated activity and absorbed dose estimations. Development of this optimised system will tend towards a future of personalised patient treatment based on absorbed dose measurements, and potentially make MRT a more safe and effective treatment modality. The benefit to society will be improved treatment efficacy, increased patient throughput and vital funds being saved within the National Health Service.

There are currently a small number of CZT-based commercial SPECT products globally; the GE Healthcare Discovery NM 530C [4] and the Spectrum Dynamics Medical D-SPECT® [5] for cardiac imaging, the mobile declipse® SPECT imaging probe by SurgicEye [6], the CMR Naviscan LumaGEM molecular breast imaging system [7] and the whole body Molecular Dynamics Valiance X12 [8]. All of these systems are optimised for diagnostic imaging of low energy gamma rays such as ^{99m}Tc (140.5 keV) and ^{123}I (159 keV), and are therefore not suitable for ^{131}I imaging. There is currently no dedicated system for dosimetry in MRT.

1.1 The DEPICT Project

The Dosimetric Imaging with Cadmium Zinc Telluride (DEPICT) project is a collaboration between The University of Liverpool, The Royal Marsden Hospital, The Royal Liverpool and Broadgreen University Hospital and the commercial partner Kromek. This collaboration allows an multidisciplinary team of physicists, clinical medical physicists and engineers to work together with the aim of developing a gamma-ray imaging system that will facilitate quantitative dosimetry in MRT. There are four main interlinking work packages in the DEPICT project:

- Optimisation of a CZT detector for ^{131}I MRT applications.
- Development of a custom-designed high-energy collimator for imaging ^{131}I.
- Evaluation of the system using medical phantoms.
- Implementation of appropriate SPECT reconstruction algorithms to visualise radionuclide distributions in 3-dimensions and obtain quantitative activity information for dose calculations.

1.2 Thesis Overview

An in-depth discussion on the Monte-Carlo modelling for developing the custom-designed collimator is outside the scope of this thesis. The main objectives of the work of this thesis were to:

- Optimise and characterise a CZT detector for MRT applications.
- Obtain planar images with the CZT detector and custom-designed high-energy parallel-hole collimator with high activities of ^{131}I.
- Extract quantitative activity information from planar images.
- Perform tomographic reconstruction to obtain 3-dimensional (3D) activity distribution.
- Evaluate the feasibility of using the detector system with radionuclides other than ^{131}I.

Chapter 2 details a literature review of MRT treatment and the process of performing dosimetry for MRT. Chapter 3 describes the principles of gamma-ray interactions with matter, gives an overview of SPECT, outlines the fundamentals of CZT semiconductor detectors and concludes by discussing the factors affecting activity quantification. Chapter 4 describes the methodology used to characterise and optimise the CZT detector for MRT applications, and Chapter 5 investigates the imaging capability of the optimised CZT detector with a variety of phantoms filled with ^{131}I. The methods to perform planar activity quantification and 3D reconstruction are discussed in Chapter 6. Finally, the feasibility of using the CZT detector system for treatments with radionuclides other than radioiodine is explored in Chapter 7.

Chapter 2

Molecular Radiotherapy

Cancer is a disease caused by the uncontrolled division of abnormal cells that have the ability to invade surrounding tissues, form a malignant primary tumour and spread to other organs (metastasise). There are several treatment options for cancer including surgery, chemotherapy, radiotherapy, immunotherapy and hormone therapy, which can be used for curative, palliative or adjuvant purposes. Although a combination of the available therapies is usually employed, surgery is often the first treatment option if a tumour can be removed from the body. Radiotherapy and chemotherapy may be used separately or together to shrink the tumour before surgery, or used post-operatively to treat residual or metastasised tumour cells. Chemotherapy uses anti-cancer drugs to kill cancer cells, whereas radiotherapy delivers high doses of radiation to the tumour volume. Both aim to stop or slow the proliferation of cancer cells.

There are two ways to deliver radiotherapy; external and internal, as highlighted in Figure 2.1. External beam radiotherapy (EBRT) is the most common method of delivering radiation to a tumour, and involves directing a beam of high-energy photons (gamma or x-rays) or charged particles (electrons or protons) at the area to be treated. In EBRT, the source of radiation is generally a linear accelerator and the shape of the beam can be dynamically adjusted to optimise the dose to the tumour volume. Brachytherapy and MRT are two types of internal radiotherapy. MRT is also known as radionuclide therapy or targeted radionuclide therapy. Brachytherapy involves the administration of sealed radioactive sources, whereas MRT utilises unsealed sources to impart a radiation dose. Both EBRT and MRT aim to deliver a high radiation dose to tumour tissue whilst minimising the dose to the surrounding healthy tissue.

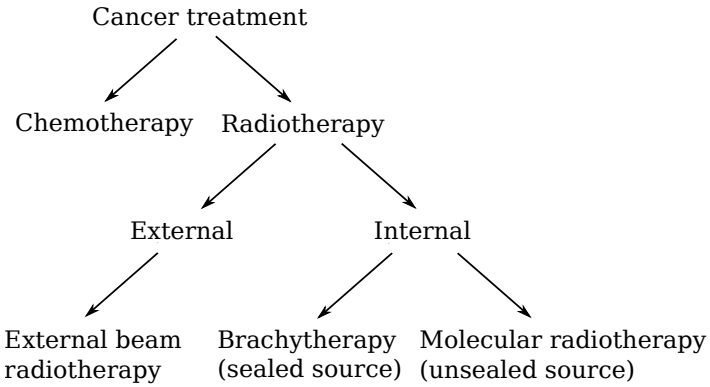

Figure 2.1: Diagram highlighting common cancer treatment modalities.

MRT is a systemic therapy that involves the internal administration of unsealed radiopharmaceuticals, either orally or intravenously. The administration of these radiopharmaceuticals is minimally invasive and the duration of treatment is shorter than that of chemotherapy [9]. The radiopharmaceuticals incorporate a radioactive tracer atom, with appropriate physical characteristics to impart a radiation dose, coupled to a larger pharmaceutically-active molecule that has a relative specificity for tumour tissue, for delivery to the target tissue [10]. As it is a systemic treatment, the radioactive material can travel throughout the body to reach the primary tumour site and distant metastases [11]. MRT is advantageous in the treatment of systemic malignancy such as bone metastases, as whole body irradiation using EBRT is impossible. MRT has therefore become one of the most preferred types of cancer treatment for specific clinical applications due to its selective ability.

2.1 Radionuclides in Molecular Radiotherapy

There are many radiopharmaceuticals used in MRT, to address a variety of clinical needs. The radionuclide coupled to the pharmaceutical will have been selected because it possesses the necessary physical properties for use in therapeutic nuclear medicine. The most important property for a therapeutic radionuclide is to decay via particle emission, therefore radionuclides that emit charged particles such as alpha (α) or beta (β^-) particles are used in MRT. These decay processes are discussed in more detail in Sections 2.1.1 and 2.1.2. The emission of charged particles with a high linear energy transfer (LET) that deliver localised cytotoxic ionising radiation can lead to double strand breaks in the DNA. This irreversible damage in-

hibits further proliferation of these tumour cells. α particles have an LET of $\sim$100 keV/µm, with $\sim$0.2 keV/µm for β^- particles [12]. A unique feature of these radionuclides is that they can exert a 'bystander' effect, unlike the drugs and toxins administered in chemotherapy which kill only the directly targeted cells. Radiation-induced bystander effects are defined as biological responses occurring in cells that are not traversed by an ionizing radiation track i.e. the responses take place in unirradiated cells. Therefore, adjacent tumour cells can potentially be destroyed even if they are not targeted by the radiopharmaceutical [13].

α and β^- particles have different physical and nuclear properties so a radionuclide can be chosen with appropriate characteristics to match the tumour type. For example, the range of α particles in tissue is about 50 – 100 µm, compared to a few mm travelled by a β^- particle [14]. Therefore, the size of the tumour or tissue mass being treated can be matched with a radionuclide that emits charged particles with the appropriate effective radiation range. The short range of these charged particles means that high activities can be administered that concentrate in small volumes, reducing the radiation dose to surrounding healthy tissue.

2.1.1 Alpha Decay

The spontaneous emission of a helium ion from a nucleus is known as α decay, with the parent nucleus losing both mass and charge in order to become stable. The decay process is illustrated in Figure 2.2 and expressed as

$$ {}^{A}_{Z}X \rightarrow {}^{A-4}_{Z-2}Y + {}^{4}_{2}\alpha, \tag{2.1} $$

where A is the atomic mass number, and X and Y are the parent and daughter nuclei. As the atomic number Z has changed, the parent and daughter nuclei are different chemical elements. α particles are emitted with discrete energies that range between 4 and 10 MeV [15] and provide a highly targeted treatment due to their high LET and short range. They are more likely to cause double-strand breaks in the DNA of cancer cells than other types of radiation and double-strand breaks are effective at causing cell death as they are more resistant to normal repair [16].

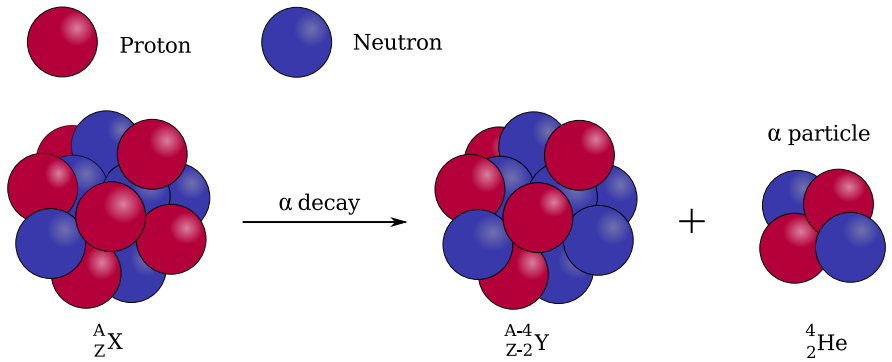

Figure 2.2: Schematic illustrating the emission of a $^{4}_{2}$He nucleus (α particle).

2.1.2 Beta Decay

The emission of β^- particles (fast energetic electrons) from unstable neutron-rich radionuclides causes damage to cancer cells. In β^- decay, a neutron within the unstable nucleus transforms into a proton and a β^- particle and an electron antineutrino ($\bar{\nu}_e$) are emitted. This is expressed in Equation 2.2 and illustrated in Figure 2.3.

$$^{A}_{Z}X \rightarrow {}^{A}_{Z+1}Y + \beta^- + \bar{\nu}_e \tag{2.2}$$

The emission of a β^- particle results in the atomic number Z increasing by one, while the atomic mass number A remains the same. The energy of the emitted β^- particle is not discrete, but a continuum. Energy conservation is maintained by the emission of the antineutrino $\bar{\nu}_e$. Antineutrinos are elementary particles that have an extremely small mass, are uncharged and only weakly interact with matter. Thus, only the β^- particle causes any significant ionisation. The maximum energy (or end-point energy of the β^-) is the energy expected according to the mass-energy relationship and is typically a few MeV. The average β^- energy is only about a third of this.

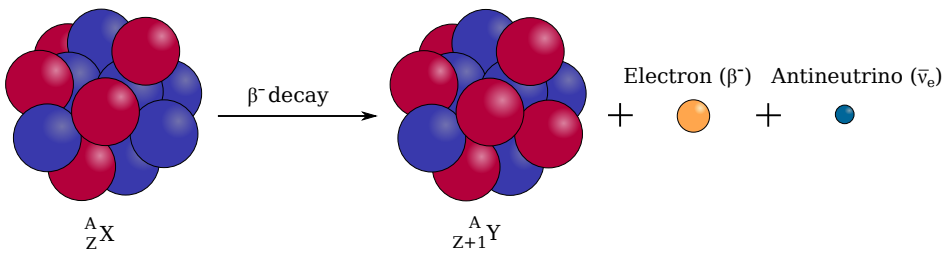

Figure 2.3: β^- decay schematic illustrating the emission of an energetic electron (β^- particle) and an electron antineutrino ($\bar{\nu}_e$).

2.1.3 Gamma Decay

In addition to charged particle decay, an excited nucleus can also decay via the emission of gamma (γ) radiation. In γ decay, the radionuclide loses energy by transitioning from an excited state to a lower energy state in the same nucleus. The energy difference between the initial and final states may appear in the form of an uncharged γ ray, as illustrated in Figure 2.4. As the atomic mass number A remains the same, the emission of a γ ray does not change the element:

$$ {}^{A}_{Z}X^{*} \rightarrow {}^{A}_{Z}X + \gamma, \tag{2.3} $$

where X^* is an excited state of nucleus X. The energy of the emitted γ ray is discrete and characteristic of the excited nucleus. It can vary from a few eV to around 8 MeV. γ rays are only weakly ionising but highly penetrating when compared to α and β particles. They therefore do not cause significant damage to cancer cells, but if emitted from the body can be imaged.

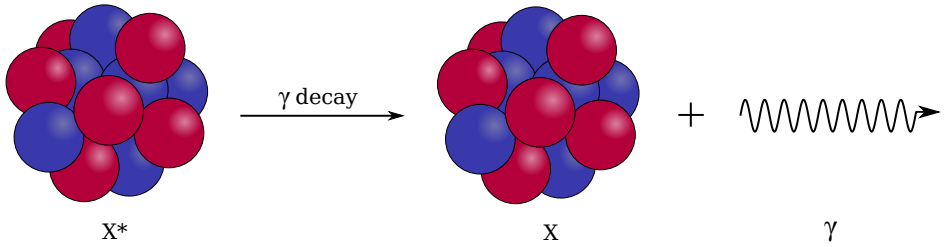

Figure 2.4: Schematic illustrating the emission of a γ ray from a nucleus in an excited state, X^*.

2.1.4 Further Criteria for Therapeutic Radionuclide Selection

Alongside undergoing charged particle decay, other properties that determine the suitability of a radionuclide for MRT include:

- Radionuclide half-life

  The period of time required for the activity level of a radionuclide to reduce to half its initial value is known as the physical half-life $t_{1/2phys}$. The half-life of the chosen radionuclide should be long enough such that a sufficient radiation dose is delivered to the tumour before physical decay and biological excretion. However, the half-life should also be short enough that the activity has decayed to minimal levels to allow the patient to be discharged from hospital within a reasonable time. The type of tumour, method

of administration, uptake mechanism and time for transportation from the production site should be taken into account. A $t_{1/2phys}$ of around 1 – 14 days is deemed to be optimum [12].

- Radionuclide decay products

  The daughter radionuclide decay product should ideally be stable, or decay with low-energy emissions and have a short half-life to avoid the patient receiving an unnecessary radiation dose.

- Radionuclide purity

  Radionuclides used for MRT should have a high grade of chemical purity and should either be carrier-free (every atom is that of the chosen radionuclide/undiluted with a stable isotope carrier) or with a very high specific activity (activity per unit mass).

- Gamma emissions

  The emission of γ radiation, alongside charged particles, provides the ability to track the biodistribution of activity in the body with a gamma camera for personalised dosimetry calculations. This will be discussed in further detail in Section 2.1.6.

- Economic factors

  Large-scale, cost-effective production feasibility will decide on the success of a radionuclide for therapy.

- Chemical Properties

  The radionuclide must be non-toxic and when coupled to an appropriate pharmaceutical, stable in vivo.

2.1.5 Suitable Radionuclides for MRT

Table 2.1 highlights radionuclides deemed suitable for MRT, given the previous requirements. This table is not exhaustive but lists the radionuclides that are frequently detailed in literature. It illustrates the type of decay, the radionuclide, the energy of the principal charged particle emitted (end-point energy if β^- emitter), the energy of the principal γ ray (if any emitted) and the physical half-life $t_{1/2\text{phys}}$. The radionuclides highlighted in bold are approved by the Medicines and Healthcare products Regulatory Agency (MHRA), the UK equivalent

of the Food and Drug Administration (FDA), or the European Medicines Agency (EMA) [17] and can therefore be used clinically in the UK. ^{223}Ra dichloride (trade name Xofigo), ^{89}Sr chloride (trade name Metastron) and ^{153}Sm (trade name Quadramet) are all used as a palliative treatment for the relief of cancer-induced bone pain and ^{90}Y treats liver cancer. For the treatment of thyroid cancer and benign thyroid diseases, ^{131}I is administered as sodium iodide ^{131}I-NaI. ^{131}I can also be coupled to the tracer metaiodobenzylguanidine (mIBG) for the management of neuroendocrine tumours (NETs), particularly neuroblastoma [18]. The radionuclide ^{177}Lu (trade name Lutathera) was approved by the EMA in 2017 and is also used in the treatment of NETs [19]. A multicentre clinical trial assessing the use of ^{177}Lu for prostate cancer is currently ongoing, with an estimated completion date of 2020 [20].

2.1.6 Theranostics

In many β^- emitting MRT radionuclides, the β^- decay populates an excited state of the daughter nucleus which leads to the emission of de-excitation γ rays alongside the β^- particles. If they escape the body, the emitted γ rays can be detected by a gamma camera to track the biodistribution of radioactivity in the body and perform dosimetry. This decay chain has been utilised in the recent concept of 'theranostics' (also known as 'theragnostics') [24]. Theranostics refers to an integrated approach to therapy and diagnosis using appropriate combinations of radionuclides and molecular targeting pharmaceuticals [25]. There are two approaches to theranostics. In the first method, a radionuclide is selected that simultaneously emits charged particles for therapy and γ rays for imaging such as ^{131}I, ^{153}Sm and ^{177}Lu, and allows real-time monitoring of the treatment. The second method involves administering pairs of radionuclides, in which one is a γ-ray or positron emitter for imaging with SPECT or PET, and the other is a therapeutic particle emitter. An example would be the imaging/therapeutic pair of ^{111}In/^{90}Y [26], where each nuclide is bound to the DOTATATE pharmaceutical [27] and administered simultaneously. The radionuclide ^{131}I is the theranostic of interest in this thesis.

Decay	Radionuclide	Energy of principal charged particle (keV) [% intensity]	Energy of principal γ ray(s) (keV) [% intensity]	Half-life $t_{1/2\text{phys}}$
α	^{211}At†	5870 (42%)	–	7.2 hours
α	^{225}Ac*†	5830 (51%)	–	10.0 days
α	^{149}Tb	3967 (17%)	165 (26%), 352 (29%)	4.1 hours
α	^{212}Bi	6051 (25%)	727 (7%)	60.6 mins
α	^{213}Bi†	5875 (2%)	440 (26%)	45.6 mins
α	**^{223}Ra***	**5716 (5%)**	**270 (14%)**	**11.5 days**
α	^{224}Ra	5685 (95%)	241 (4%)	3.7 days
α	^{227}Th*	6038 (24%)	236 (13%)	18.7 days
β^-	^{32}P†	1710 (100%)	–	14.3 days
β^-	**^{89}Sr**†	**1500 (100%)**	–	**50.5 days**
β^-	**^{90}Y*†**	**2280 (100%)**	–	**2.7 days**
β^-	^{143}Pr	934 (100%)	–	13.6 days
β^-	^{169}Er†	343 (45%), 351 (55%)	–	9.4 days
β^-	^{47}Sc	441 (68%)	159 (68%)	3.4 days
β^-	^{67}Cu†	377 (57%)	185 (49%)	2.6 days
β^-	^{77}As	683 (97%)	239 (2%)	1.6 days
β^-	^{105}Rh	567 (75%)	319 (19%)	1.5 days
β^-	^{111}Ag	1037 (92%)	342 (7%)	7.5 days
β^-	**^{131}I*†**	**606 (90%)**	**364.5 (82%)**	**8.0 days**
β^-	^{149}Pm	1071 (96%)	286 (3%)	2.2 days
β^-	**^{153}Sm*†**	**704 (49%)**	**103 (30%)**	**2.0 days**
β^-	^{155}Tb	519 (66%)	87 (32%), 105 (25%)	6.9 days
β^-	^{156}Sm	431 (44%), 700 (48%)	88 (24%), 204 (21%)	9.4 hours
β^-	^{161}Tb	518 (65%)	26 (23%), 49 (17%)	6.9 days
β^-	^{165}Dy	1286 (83%)	95 (4%)	2.3 hours
β^-	^{166}Ho†	1774 (50%), 1855 (49%)	81 (7%)	1.2 days
β^-	^{170}Tm	968 (82%)	84 (3%)	128.6 days
β^-	^{175}Yb	470 (73%)	396 (13%)	4.2 days
β^-	**^{177}Lu*†**	**498 (79%)**	**208 (11%)**	**6.7 days**
β^-	^{186}Re†	1069 (80%)	137 (9%)	3.8 days
β^-	^{188}Re†	2120 (70%)	155 (16%)	16.9 hours
β^-	^{198}Au	961 (99%)	412 (96%)	2.7 days
β^-	^{199}Au	294 (72%)	158 (40%)	3.1 days
β^-	^{212}Pb*†	331 (83%)	239 (44%)	10.6 hours

Table 2.1: Table of radionuclides for therapy. Radionuclides given in bold are FDA approved and those highlighted will be discussed in this thesis. *Spotlight on Radiotherapeutics: A Pharma Matters Report [21], †Radionuclides for Imaging and Therapy in Oncology [22]. Charged particle energies extracted from the NUDAT database [23].

2.2 Radioiodine Thyroid Treatment

The archetypal example of MRT is the radioiodine, ^{131}I, treatment of malignant and benign thyroid diseases and this is the radionuclide of interest for the DEPICT project. Since the 1940s [28], it has been used extensively for treatment of thyroid diseases. Out of the 37 known isotopes of iodine, four are used as tracers and therapeutic agents in medicine. These are ^{123}I, ^{124}I, ^{125}I, and ^{131}I, with the two most commonly used isotopes being ^{123}I and ^{131}I. ^{123}I has a half-life $t_{1/2phys}$ of 13.2 hours and decays via electron capture to ^{123}Te, emitting γ radiation (159 keV). This makes it a suitable isotope for diagnostic imaging as the γ ray is of ideal energy to be detected by a gamma camera, as discussed in Section 3.1. It causes less internal damage to the patient as a lower radiation dose is received than if the isotope also emitted particulate radiation. ^{131}I has a physical half-life $t_{1/2phys}$ of 8.04 days and decays via both β^- and γ-decay modes. Therefore, it is suitable for use as a theranostic for therapy and imaging. The primary emissions of ^{131}I highlighted in red in Figure 2.5a are β^- particles with an end-point energy of 606.3 keV ($P_\beta = 89.9\%$), average energy of 192.6 keV and mean path length of ~1 mm in soft tissue and 364.5 keV γ rays ($P_\gamma = 81.7\%$). The main decay product of ^{131}I is stable ^{131}Xe. The continuous beta spectrum is shown in Figure 2.5b.

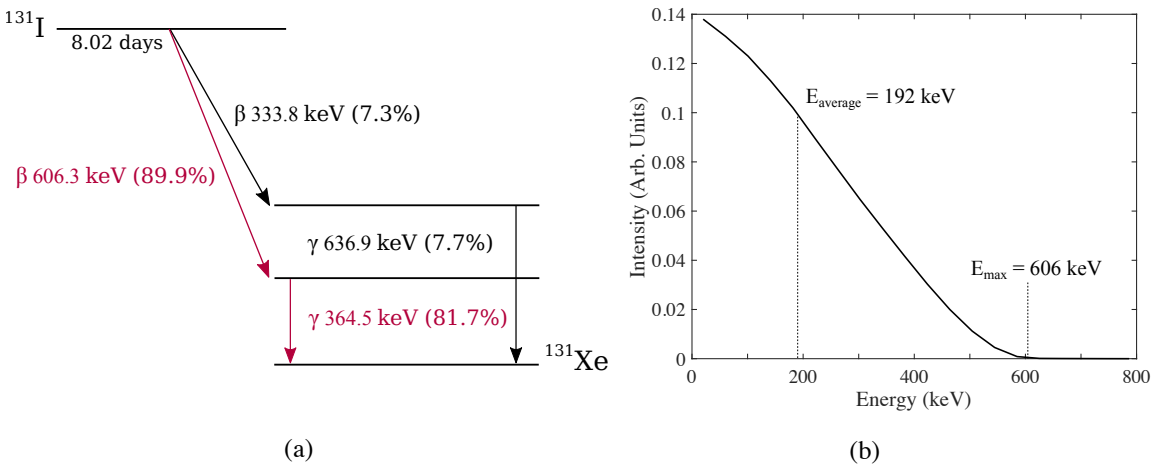

Figure 2.5: (a) ^{131}I decay scheme with the primary β^- and γ emissions highlighted in red. Only the major transitions are shown. The full decay scheme is shown in Appendix A.1 and (b) the continuous β particle energy spectrum for ^{131}I decay [29].

In MRT practice across 26 countries in Europe in 2016, approximately 72% of all therapies involved ^{131}I [30]. There are a broad range of administered ^{131}I activities, but many agree

on the limits [31, 32, 33]. Following thyroidectomy (removal of all, or part of the thyroid gland), activities of ^{131}I in the range 1.1 – 3.7 GBq (30 – 100 mCi) are prescribed for post-operative ablation of thyroid bed remnants. In patients with thyroid cancer and lymph node metastases, generally higher activities of up to 5.5 GBq (150 mCi) are administered, and this increases to 7.4 GBq (200 mCi) for the treatment of distant metastases.

2.3 Dosimetry of Molecular Radiotherapy

Dosimetry is the process of relating the administered activity to the absorbed radiation dose of an organ or whole body. In EBRT, it is possible to precisely calculate the absorbed dose from the point at which the radiation enters the body to the tumour target. MRT however, relies on the accumulation of radiopharmaceuticals in the target tissue, that deliver a low and continuously decreasing dose. This accumulation depends on the physiological mechanisms that govern the distribution of the radiopharmaceutical in the body [34]. The calculation of radiation energy deposited by radionuclides in the body during MRT is known as internal radiation dosimetry (IRD). Performing IRD would ideally follow a number of simplified steps:

- Quantitative imaging of the patient at multiple times post administration of the radiopharmaceutical.
- Modelling the distribution of activity within the patient over time from these images.
- Converting this cumulative activity in different volumes into an absorbed dose.

2.3.1 The MIRD Schema

The MIRD Schema, proposed by the Medical Internal Radiation Dose (MIRD) Committee of the Society of Nuclear Medicine, is the most widely used methodology for providing guidance on how to calculate the mean absorbed dose from distributed sources of radioactivity in MRT [35, 36]. The mean absorbed dose is often used to quantify the efficacy of a therapeutic procedure. The MIRD Schema assumes the body is composed of source s and target t organs. Source organs are organs in which the radiopharmaceutical is localised, whereas target organs are those that are irradiated by a source organ. A proportion of the emitted energy will be absorbed in other organs, and some will escape the body completely. The absorbed dose is defined as the energy absorbed per unit mass and is calculated through the knowledge of the

cumulated source activity $\tilde{A}_s$ (Bq·sec or μCi·hr) in organ s over the time interval of interest t_1 to t_2 by

$$\tilde{A}_s = \int_{t_1}^{t_2} A_s(t)dt. \tag{2.4}$$

The mean absorbed dose $\bar{D}(t \leftarrow s)$ (in Gy or Rad) to a target organ t from a source organ s is then defined by the MIRD schema as,

$$\begin{aligned} \bar{D}(t \leftarrow s) &= \frac{\tilde{A}_s}{m_t} \sum_i \Delta_i \phi_i(t \leftarrow s) \\ &= \tilde{A}_s \sum_i \Delta_i \Phi_i(t \leftarrow s), \end{aligned} \tag{2.5}$$

where m_t is the mass of the target organ (kg) and Δ_i (Gy·kg/Bq·s) is the equilibrium absorbed dose constant, which is the mean energy emitted per nuclear transition for radiation type i. The absorbed fraction and the specific absorbed fraction of energy for target organ t for particles i emitted by source organ s are represented by $\phi(t \leftarrow s)$ and $\Phi(t \leftarrow s)$ respectively. For a given radionuclide and specific source-target organ combination in a mathematical model, the quantity $\sum_i \Delta_i \Phi_i(t \leftarrow s)$ is constant. The MIRD Schema simplifies these values and refers to them as S factors, defined as the mean absorbed dose in the target per unit cumulated activity (Gy/Bq · sec or rad/μCi · hr),

$$S(t \leftarrow s) = \sum_i \Delta_i \Phi_i(t \leftarrow s). \tag{2.6}$$

This S factor allows simplification of the mean absorbed dose formula, Equation 2.5, to

$$\bar{D}(t \leftarrow s) = \tilde{A}_s \, S(t \leftarrow s). \tag{2.7}$$

There are generally a number of source organs, therefore the total dose to the target organ is the sum of the absorbed doses from all source organs. The estimation of mean absorbed dose is thus dependent upon two types of information: time-dependent biokinetic factors (incorporated within $\tilde{A}$) and time-independent physical factors (represented within S) [37]. The biokinetic factors incorporate characteristics of uptake and retention of activity in the regions of interest, and include consideration of the physical and biological decay of the radiopharmaceutical. The physical S factor considers the types and energies of the radiations emitted, size and shape of the source and target organs, and the composition of the absorbing

and intervening media. Tables of S factors are available for many situations of interest in nuclear medicine [38].

2.3.2 Limitations in Molecular Radiotherapy Dosimetry

There are three main limitations in MRT dosimetry. The first limitation is the MIRD Schema assumes a homogeneous distribution of radioactivity in the target tissue, whereas in reality there is a non-uniform activity distribution due to variations in pharmacokinetics (delivery, uptake, site-specific binding and clearance) [39]. Inhomogeneous radiation distributions may also arise as the tumour can shrink during treatment, increasing the complexity of dosimetry in MRT. In addition, the MIRD specific absorbed fractions [40] assume a monoenergetic γ-ray source, which is not the reality for many radionuclides. ^{131}I is not a monoenergetic source as it emits γ rays with energies 80.2 keV (2.6%), 284.3 keV (6.1%), 364.5 keV (81.7%) and 636.9 (7.2%), although not all of these are shown on the simplified decay scheme in Figure 2.5b.

The second limitation is the use of generic S factors. A MIRD total-body phantom was developed for Monte-Carlo calculations of specific absorbed fractions for photons of 12 energies from 10 keV to 4 MeV [40]. The MIRD phantom was designed to represent a reference adult and consisted of three principal sections: an elliptical cylinder representing the arms, torso and hips; two truncated circular cones representing the legs and feet, and an elliptical cylinder representing the head and neck, with an overall mass of approximately 70 kg. The sizes and shapes of the internal volumes resembling the organs and tissues of an average person are defined by mathematical equations. Monte-Carlo methods are subsequently used to determine absorbed fractions because of the complicated geometric configurations that must be considered. Problems with S factors arise when dosimetry needs to be performed on a patient not resembling the 'reference man' phantom. S factors that are based on a standard anthropomorphic phantom make assumptions about anatomy (standard weights, sizes and distance between source and target organs) and radiopharmaceutical distribution (uniformity of source and uptake) that aren't necessarily valid in individual patients. Although more sophisticated and anatomically accurate phantoms have been developed over the years [41], there is an obvious need for patient specific S factors as the space between source and target organs, and size and weight of organs will differ between patients.

Finally, limitations arise in dosimetry calculation as there are uncertainties in measuring radioactivity over time in a patient. As shown in Equation 2.4, the first step for calculating the mean absorbed dose is determining the cumulated source activity. This is determined by imaging the patient at certain time points following administration of the radiopharmaceutical and converting image counts into activity, to calculate a time-activity curve (TAC). The TAC is described by

$$\tilde{A}_s = A_0 \int_0^\infty e^{-\frac{ln(2)t}{t_{1/2\text{eff}}}} dt, \tag{2.8}$$

where $t_{1/2\text{eff}}$ is the effective half-life. The effective half-life $t_{1/2\text{eff}}$ is the period of time required for the radioactivity level to reduce to half the initial level, due to radioactive decay (physical half-life $t_{1/2\text{phys}}$) and biological elimination (biological half-life $t_{1/2\text{biol}}$) where $\frac{1}{t_{1/2\text{eff}}} = \frac{1}{t_{1/2\text{phys}}} + \frac{1}{t_{1/2\text{biol}}}$. The effective half-life of ^{131}I is approximately one week. The cumulated activity is then given by integrating the TAC over a number of days. Figure 2.6a illustrates an ideal TAC showing the rapid uptake of the radiopharmaceutical and then exponential decay due to the physical and biological effects. In reality, a TAC similar to Figure 2.6b is obtained. Due to dead time in current gamma cameras, discussed in detail in Section 3.4.4, there is often a limit placed on the earliest imaging time point of a day or two post administration of gigabecquerels of activity. In addition, ideally a minimum of 5 points would be acquired for the TAC, however in reality only 2 or 3 images are acquired with each patient. This limit on the earliest imaging point, along with only obtaining a few measurements of the activity, makes extrapolation to the initial administered activity very challenging. Often, straight lines are drawn across to both the y- and x-axes from the first and last time points respectively, and the cumulative activity is then obtained from the area created by these lines. This leads to large uncertainties in the calculation of cumulated source activity.

It is therefore very evident that with such large uncertainties in both the values of $\tilde{A}_s$ and S, that this will lead to errors in the value of absorbed dose $\bar{D}$. Due to this lack of accurate dosimetry protocols, current MRT treatment plans are undesirably generic, in which the administered activity is often fixed for a given procedure or scaled according to the weight or body surface area of the patient [1]. MRT is typically prescribed to patients on the basis of

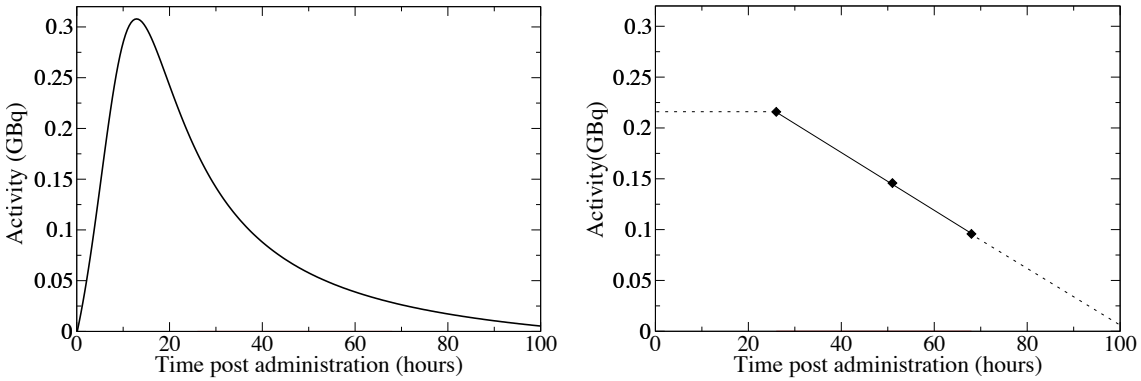

Figure 2.6: (a) Ideal time-activity curve and (b) an example time-activity curve from The Royal Marsden Hospital where only three images were collected following the administration of the radiopharmaceutical.

the maximum activity of the therapeutic radiopharmaceutical that has been shown in clinical trials to minimise the incidence of damage to critical normal tissues to an acceptable fraction of the trial population (typically 5%). This implies the other 95% potentially could have received a higher activity, and therefore a more effective treatment [42]. For the same initial administered activity, the absorbed dose to the normal tissue has been found to vary by up to an order of magnitude [43], and by up to two orders of magnitude between patients for absorbed dose to the target tissue [2, 3] due to differences in uptake and retention of the therapeutic agent. Therefore, treatments could be improved dramatically by measurement of absorbed dose to the critical tissues on an individual patient basis. A recent EU directive 2013/59/EURATOM Article 56 also states, *'For all medical exposure of patients for radiotherapy purposes, exposures of target volumes shall be individually planned and their delivery appropriately verified'*. Personalised treatment planning and verification is clearly essential and needs to replace these simplified MIRD internal dosimetry models, to produce better and more reliable outcomes. MRT will then move from being largely a last-resort palliative treatment, to a frontline cancer therapy.

Chapter 3

Nuclear Medicine

Since the discovery of x-rays by Wilhelm Röntgen in 1895 [44], electromagnetic radiation has been used in medical imaging for non-invasive investigations of the internal structures of the body. Nuclear medicine is a branch of medical imaging that involves the administration of radioactive material for both diagnostic and therapeutic purposes. It differs from other imaging modalities such as x-ray Computed Tomography (CT), as the physiological functions of the body are investigated rather than the anatomical structure. Nuclear medicine imaging modalities include Positron Emission Tomography (PET) and Single Photon Emission Computed Tomography (SPECT), which are used to visualise the 3D distribution of the radioactive material in the body. Positron emitting radionuclides are administered in PET, from which two annihilation photons are detected. For SPECT γ-ray emitting radionuclides are utilised and this modality can therefore be used to image the γ rays emitted during ^{131}I MRT.

3.1 Single Photon Emission Computed Tomography

Modern SPECT systems are based on the gamma camera principle by Hal Anger [45] and the main components are a collimator, scintillation crystals (typically thallium doped sodium iodide NaI(Tl)) and photomultiplier tubes (PMTs), illustrated in Figure 3.1. γ rays emitted from the body of a patient interact with the scintillation crystal, causing fluorescence and the emission of visible light that is detected by the PMTs. The light is then converted into electrical signals that are processed by readout electronics and sent to a computer to produce an image. One of the basic problems suffered in 2D (or planar) gamma camera imaging is that internal information can be lost due to overlying or underlying organs. 3D imaging is

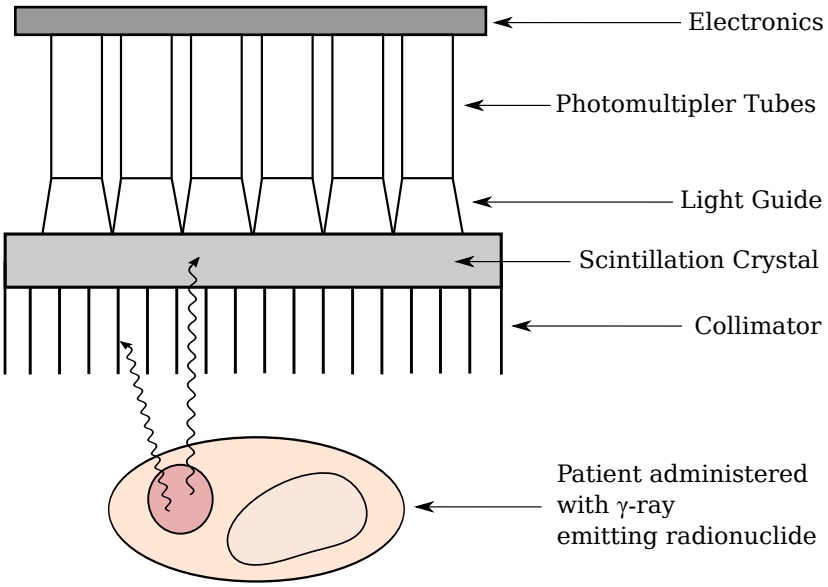

Figure 3.1: Schematic diagram of γ rays emitted from the body of a patient. One γ ray passes through the collimator to the detector and one is absorbed by the collimator.

required for accurate quantification of the 3D radionuclide distribution within the body, and this is achieved by reconstructing 2D images (projections) collected at multiple angles around the body. There are typically two gamma cameras mounted on a rotating gantry, reducing the scan time over a single gamma camera by acquiring two images simulataneously. The most common method of data acquisition is known as 'step and shoot', where images are obtained at predefined angular positions over a 360° rotation around the patient. Typically, 120 projections are acquired at 3° increments with a total scan time of around 20 – 30 minutes [46]. 3D radionuclide distributions are then reconstructed from these 2D projections and should accurately correspond to the activity distribution within the patient. SPECT systems are optimised for imaging the low-energy radionuclide ^{99m}Tc, with its photopeak at 140.5 keV. ^{99m}Tc is the most commonly used radionuclide in medicine and provides diagnostic information. NaI(Tl) scintillator detectors are most commonly used in SPECT as large crystal sizes can be produced relatively inexpensively, giving good efficiency in the 50 – 250 keV range. Typically, NaI(Tl) crystals are between 6.4 mm to 12.7 mm thick, with 9.5 mm thick crystals suitable for imaging ^{99m}Tc.

3.2 Gamma Ray Interactions with Matter

In order to image γ rays using SPECT, they must pass through a collimator and interact within the radiation detectors positioned around the patient. γ rays are massless and chargeless, and therefore transfer energy to charged electrons in the detection material during ionisation or excitation to create a signal in the radiation detector. In spectroscopic detectors, the electrical signal produced has an amplitude that is proportional to the energy deposited in the detecting medium. There are three primary interaction mechanisms that a γ ray can undergo; photoelectric absorption, Compton scattering and pair production. The work in this thesis focuses on γ rays with energies of less than 400 keV and the detector material of interest for the DEPICT project is CZT, which has an effective atomic number Z_{eff} ~50. Photoelectric absorption and Compton scattering are therefore the only possible interaction processes, as shown by the dotted grey diagonal lines in Figure 3.2. It can be seen in Figure 3.2 by the red circle that Compton scatter interactions are slightly dominant in this material for 364.5 keV ^{131}I γ rays. Above approximately $Z = 60$, the photoelectric effect dominates at 364.5 keV. The DEPICT collimator discussed in Section 5.1 is made of tungsten. Tungsten has $Z = 74$ and it can be seen by the blue diamond in Figure 3.2 that the photoelectric effect dominates at this atomic number with 364.5 keV ^{131}I γ rays. This effect is utilised by gamma camera collimators to preferentially absorb γ rays not travelling in the desired direction and will be discussed in detail in Section 3.3.

Photoelectric absorption is the process in which a γ ray interacts with a bound atomic electron, transferring all of its energy to the electron as illustrated in Figure 3.3a. A photoelectron e^- is subsequently emitted from the atom with kinetic energy

$$E_{e^-} = E_\gamma - E_b, \tag{3.1}$$

where E_γ is the original γ-ray energy and E_b represents the binding energy of the photoelectron in its original shell. This process leaves the atom in an ionised state with a vacancy in one of its bound shells. Rearrangement of the electrons from other higher lying shells filling the inner shell vacancy can cause the emission of one or more characteristic x-ray photons. These x-rays are typically reabsorbed close to the original site, but can also be emitted from the material.

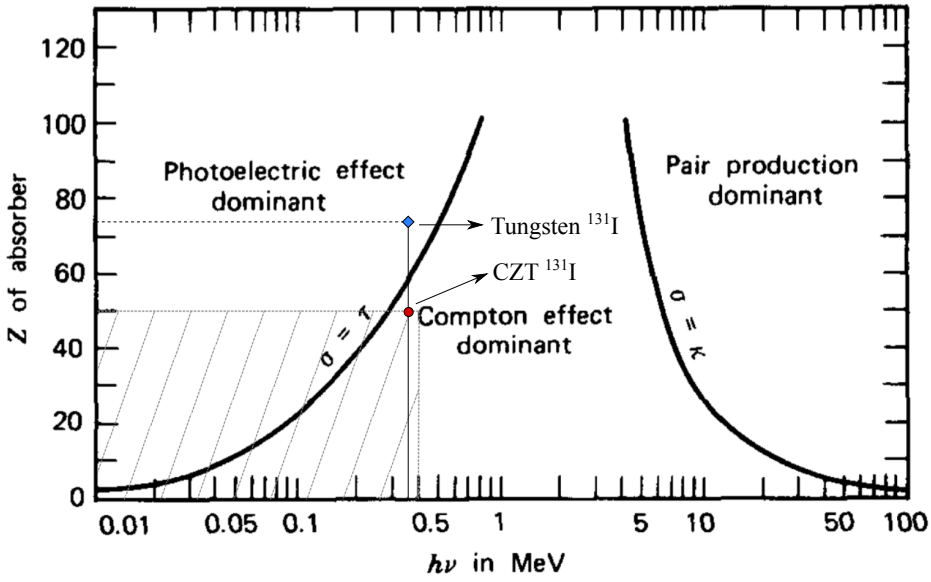

Figure 3.2: A plot showing the probability of a γ ray interacting via photoelectric absorption, Compton scattering or pair production as a function of γ-ray energy ($E = h\nu$) and absorber atomic number, Z [47]. Dotted grey lines highlight the interaction mechanisms of interest in this work. Although pair production is included here, γ rays emitted from therapeutic radionuclides (Table 2.1) never reach the minimum energy required (1022 keV) for pair production. The blue diamond highlights the dominant interaction effect at the atomic number of tungsten ($Z = 74$) and the red circle highlights the dominant effect for CZT (Z_{eff} ~50) for ^{131}I 364.5 keV γ rays.

Compton scattering occurs when an incident γ ray is deflected by a weakly bound atomic electron, transferring a fraction of its energy to the electron, shown in Figure 3.3b. The equation that relates the incident γ-ray energy E_γ, scattering angle θ, and energy of the scattered γ ray $E_{\gamma'}$ is

$$E_{\gamma'} = \frac{E_\gamma}{1 + \frac{E_\gamma}{m_0 c^2}(1 - \cos\theta)}, \tag{3.2}$$

where $m_0 c^2$ is the rest-mass energy of the electron (0.511 MeV). The γ ray cannot deposit all of its energy during Compton scattering. The maximum energy is transferred to the electron when the incident γ ray is scattered through an angle of 180°, and for the 364.5 keV γ ray from ^{131}I, the maximum energy that can be transferred to an electron is 214.3 keV. The probability of Compton scattering increases with electron density (number of electrons per unit mass) and therefore increases linearly with atomic number Z.

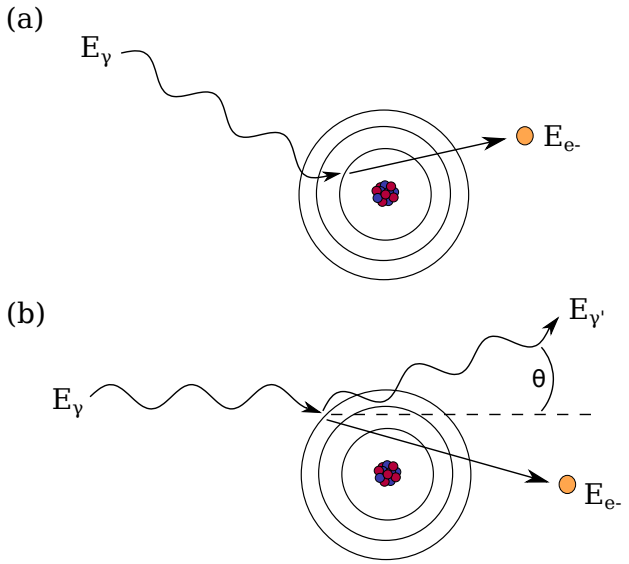

Figure 3.3: A schematic illustration of (a) photoelectric absorption and (b) Compton scattering.

3.3 Collimators

Collimators form the primary layer of the gamma camera and are essential for image formation. In the absence of a collimator, no relationship can be formed between the position at which a γ ray interacts within the detector and from where the γ ray was emitted from within the patient. As γ rays are uncharged and cannot be focused, collimators operate via the principle of absorptive collimation. This is the principle that γ rays not travelling in the desired direction are absorbed by the collimator before reaching the detector, as shown in Figure 3.4a. Materials of high atomic number Z and high density ρ are required for the collimator to increase the likelihood of absorbing γ rays, as in the energy range of interest in SPECT ($\sim$100 – 400 keV γ rays), photoelectric absorption increases with increasing Z, as shown in Figure 3.2. Collimators are therefore typically made of lead ($Z = 82$, $\rho = 11.34$ g/cm^3) or tungsten ($Z = 74$, $\rho = 19.24$ g/cm^3).

There are four basic collimator types used with a gamma camera: pinhole, parallel-hole, diverging and converging. Pinhole collimators are cone-shaped with a single pinhole at the apex that generates a magnified, inverted image of the organ of interest, whereas parallel-hole collimators have a large array of holes parallel to one another and perpendicular to the detector face. Diverging and converging collimators have multiple holes that either diverge

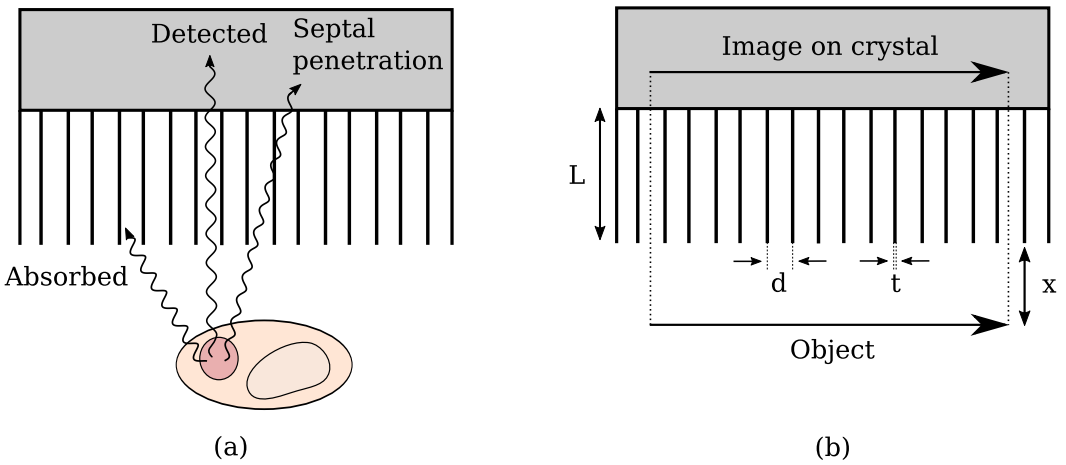

Figure 3.4: Parallel-hole collimator schematics illustrating (a) absorption of a γ ray by the septa, detected γ ray following a straight line trajectory from patient to detector, and a γ ray undergoing septal penetration before being detected, and (b) hole length L, hole diameter d, septa thickness t, and distance from object to collimator x.

or converge with respect to the detector face, allowing minimisation or magnification of an organ or interest, respectively. The most common type and the collimator of interest for the DEPICT project is the parallel-hole collimator. Parallel-hole collimators are defined by hole length L, hole diameter d and septa thickness t, where septa are the high Z material walls between the collimator holes, illustrated in Figure 3.4b. A direct projection of the radionuclide distribution in the object being imaged is formed on the detector crystal. Parallel-hole collimators can have various geometries for use with a range of medical radionuclides with different γ-ray energies. A low-energy collimator is used for γ-ray energies less than 140 keV, a medium-energy for less than 260 keV and a high-energy for less than 400 keV [48]. Imaging the 364.5 keV γ rays following ^{131}I MRT requires the use of a high-energy collimator, and a typical clinical high-energy parallel-hole collimator has hexagonal holes with $L = 59.7$ mm, $d = 4.0$ mm and $t = 2$ mm [49].

Collimator spatial resolution R_{coll} depends on L, d and the distance from the object being imaged to the collimator x:

$$R_{coll} \approx \frac{d}{L}(L + x). \tag{3.3}$$

The collimator spatial resolution increases as a function of x, therefore the image quality degrades with increasing distance to the object being imaged. This is due to collimator holes

not being infinitely long or thin, so γ rays that are travelling close to perpendicular to the crystal can be accepted and included in the image. This results in a blurring of the image. It also increases with d, indicating smaller collimator holes improve the resolution. The total spatial resolution of the system R_{sys} is a combination of both the intrinsic detector spatial resolution R_{int}, which will be discussed later, and the collimator spatial resolution R_{coll}:

$$R_{sys} = \sqrt{R_{int}^2 + R_{coll}^2}. \tag{3.4}$$

The collimator is usually the limiting factor in gamma camera system spatial resolution as the collimator spatial resolution is typically worse than the intrinsic detector spatial resolution. For example, the GE Healthcare Infinia Hawkeye® SPECT system configured with a high-energy parallel-hole collimator and standard 9.5 mm-thick crystals has an intrinsic spatial resolution of 3.8 mm FWHM, and a system spatial resolution at 10 cm of 12 mm FWHM [50]. In diagnostic SPECT, administered activities range from a few MBq up to ∼900 MBq [51, 52], therefore collimators are often designed to maximise detection efficiency to ensure sufficient statistics are produced for a high quality image. This is achieved by increasing the hole size to allow more γ rays through. However, the corresponding decrease in septal thickness can lead to γ rays either passing through the septa material before being detected or being scattered and detected with a reduced energy. This is known as septal penetration and is shown in Figure 3.4a. Septal penetration results in decreased image contrast, degradation of spatial resolution and increased image artefacts, leading to difficulties in accurate activity distribution quantification [53]. The transmission of γ rays through an absorber material such as the collimator septa is described by the exponential equation:

$$I(x) = I(0)\ e^{-(\mu x)} \tag{3.5}$$

where $I(x)$ is the intensity of γ rays transmitted through thickness x of the absorber material, $I(0)$ is the intensity recorded with no absorber material present, and μ is the linear attenuation coefficient of the absorber material. For 364.5 keV γ rays, the linear attenuation coefficient of lead is 3.12 cm^{-1} [54] therefore when using a high-energy parallel-hole collimator with a typical septal thickness of 1.8 mm, 57% of the γ rays would pass through the septa of a lead collimator (with the possibility of then being attenuated by further septa). Septal penetration degrades the final image as this incomplete attenuation decreases the signal-to-noise ratio resulting in a loss of image contrast. A reasonably small level of septal penetration

is accepted, around 5% [55], to allow for adequate detection efficiency.

3.4 Detector Properties

Once the γ rays have passed through the collimator, they interact with the detector. There are several properties that are important for a γ-ray detector to be used in SPECT. The following sections provide a description of these performance characteristics.

3.4.1 Energy Resolution

Energy resolution is a measure of the ability to precisely determine the energy deposited in the detector. The intrinsic energy resolution of a radiation detector ΔE_i is given by the full width at half maximum (FWHM) of a photopeak E_0 (the peak formed when a γ ray deposits all of its energy in the detector). The FWHM of a photopeak is influenced by three terms:

$$(\Delta E_i)^2 = (\Delta E_s)^2 + (\Delta E_{col})^2 + (\Delta E_{el})^2. \tag{3.6}$$

The first term $(\Delta E_s)^2$ is due to the statistics associated with the charge production process in the detector, and arises because the charge is generated by discrete charge carriers:

$$(\Delta E_s)^2 = (2.35)^2(F.E_\gamma.\epsilon), \tag{3.7}$$

where F is the Fano factor, which accounts for deviation of the observed statistical fluctuations in the number of charge carriers from pure Poisson statistics, E_γ is the γ-ray energy, and ϵ is the average energy required to produce a pair of charge carriers. The second term $(\Delta E_{col})^2$ and the third term $(\Delta E_{el})^2$ correspond to the contribution to the energy resolution from incomplete charge collection and electronic noise, respectively. The contribution from electronic noise E_{el} is independent of the γ-ray energy and determined largely by the detector capacitance and front-end electronics. In SPECT, γ-ray events are selected for imaging from the γ-ray spectrum only if their energy falls within a user specified energy window, which is typically around the photopeak of interest. A smaller photopeak FWHM indicates superior energy resolution and allows for narrow energy windows to be set around a γ-ray energy of interest. This reduces the number of scattered events included in the image, increasing the signal-to-noise ratio. In turn, this improves delineation of tumour volumes which is an important aim of the DEPICT project.

3.4.2 Spatial Resolution

The spatial resolution of a gamma camera quantifies how well a detector system can localise a γ-ray interaction within the detector crystal. It is related to the dimensions of the read-out segments, be it the pixel size or strip pitch. The position sensitivity of pixelated detectors is of interest in this work and will be expanded upon in Section 3.5.3. The intrinsic spatial resolution depends on the detector crystal and electronics however the total system resolution has to also take into account the properties of the collimator, discussed in more detail in Section 3.3. Being able to determine the origin of a γ ray is essential in SPECT for accurate measurements of the activity within a patient.

3.4.3 Detection Efficiency

The probability that a γ ray will interact in the detector and produce a signal is known as the detector efficiency. There are several methods to describe efficiency including absolute ϵ_{abs} and intrinsic ϵ_{int}, which are defined as

$$\epsilon_{abs} = \frac{\text{Number of } \gamma \text{ rays recorded}}{\text{Number of } \gamma \text{ rays emitted by the source}} \tag{3.8}$$

and

$$\epsilon_{int} = \frac{\text{Number of } \gamma \text{ rays recorded}}{\text{Number of } \gamma \text{ rays incident on the detector}}. \tag{3.9}$$

The number of γ rays recorded can refer to either the total number of γ rays detected, or those contained within the photopeak. The absolute efficiency, unlike the intrinsic efficiency, depends on the solid angle subtended by the detector. The relative efficiency of a detector can also be quoted and compares the absolute efficiency of the detector to a 76 x 76 mm NaI(Tl) detector, irradiated by a ^{60}Co (1332 keV γ ray) source at 25 cm from the detector face (ϵ_{abs} = 1.2 x 10^{-3} cps/Bq). A highly efficient detector is usually desirable in diagnostic procedures to reduce the time required for patient imaging. This is not as essential for imaging following MRT as very high activities are administered.

3.4.4 Dead time

At high count rates there is an increased likelihood of two γ rays interacting in the detector crystal within the response time of the detector. These events can be lost because of the

short but finite time interval required to process each recorded event. The minimum time separation is known as the dead time τ of the system. The detector itself can induce an intrinsic dead time, alongside contributions from the electronics, and readout and storage of the event information. There are two types of dead time; paralysable and non-paralysable, illustrated in Figure 3.5. In a non-paralysable detector, an event that occurs during the dead time is lost but has no effect on subsequently occurring events. However, in a paralysable detector an interaction that occurs during the dead time would not be counted and extends the dead time.

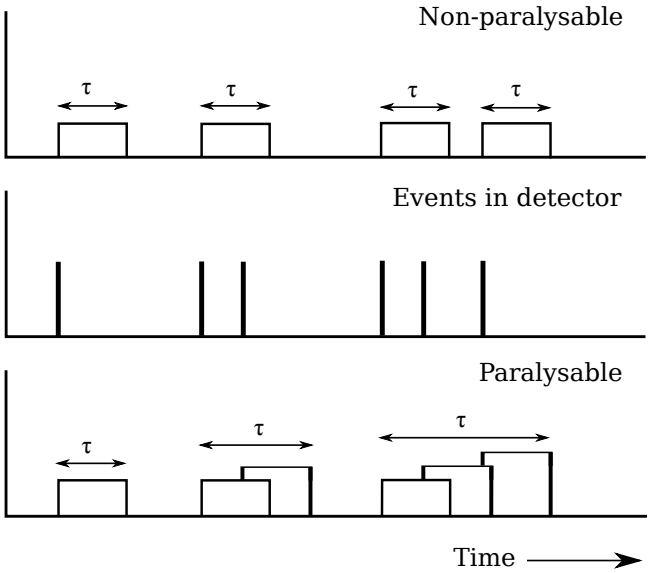

Figure 3.5: Illustration showing non-paralysable and paralysable models of dead time τ for radiation detectors.

For each model of dead time, the measured m count rate of a γ-ray detector can be related to the true, or incident, count rate n and the detector dead time τ. For the non-paralysable model, this relationship is expressed by

$$m = \frac{n}{1 + n\tau}. \tag{3.10}$$

The equation expressing the relationship between m, n and τ for the paralysable model is

$$m = ne^{-n\tau}. \tag{3.11}$$

Derivations for Equations 3.10 and 3.11 can be found in [47]. A plot of measured count rate m versus the true count rate n is shown in Figure 3.6 for both models, alongside a dashed black line showing $m = n$; the count rate response of an ideal detector.

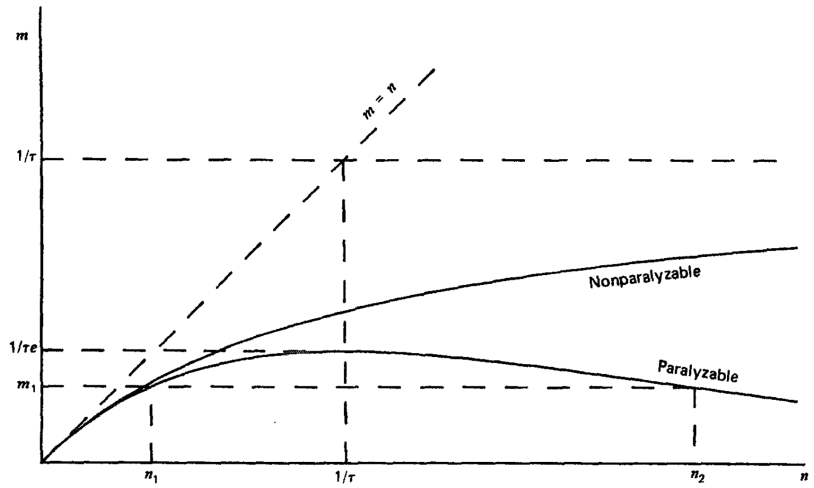

Figure 3.6: Variation of the measured rate m as a function of the true rate n for the two models of dead time [47].

Figure 3.6 shows that at low counting rates, the two models predict similar behaviour; at high count rate the models begin to diverge. At the high count rates associated with MRT, dead time losses may be extreme and can mean that the detected count rate can no longer be accurately corrected to the administered activity. A detector that can function at high count rates and has minimal dead time is therefore required for use in the DEPICT project.

3.5 Semiconductor Detectors

Semiconductor detectors are the most recent class of radiation detectors to have been developed, and many report on their suitability for use in nuclear medicine imaging systems [56, 57, 58, 59]. Compared to scintillator based cameras that first convert incident γ rays to visible light that is then subsequently detected by PMTs and converted into an electronic signal, semiconductors directly convert the absorbed γ ray into an electronic current. This improves the detectors energy resolution and spatial resolution through direct conversion of the energy and location of the detected γ ray [60]. The following sections describe the principles of semiconductors for use as radiation detectors.

3.5.1 Band Structure

Semiconductor materials have crystalline structures in which electrons are confined to energy bands and the material properties depend on the structure of these bands. The two bands are the valence and conduction bands. Electrons in the valence band are bound to specific

lattice sites within the crystal, whereas electrons in the conduction band are free to migrate through the crystal structure. An energy band gap E_g separates the two bands. The structure of the bands dictates whether a material acts as an insulator, semiconductor or conductor, illustrated in Figure 3.7.

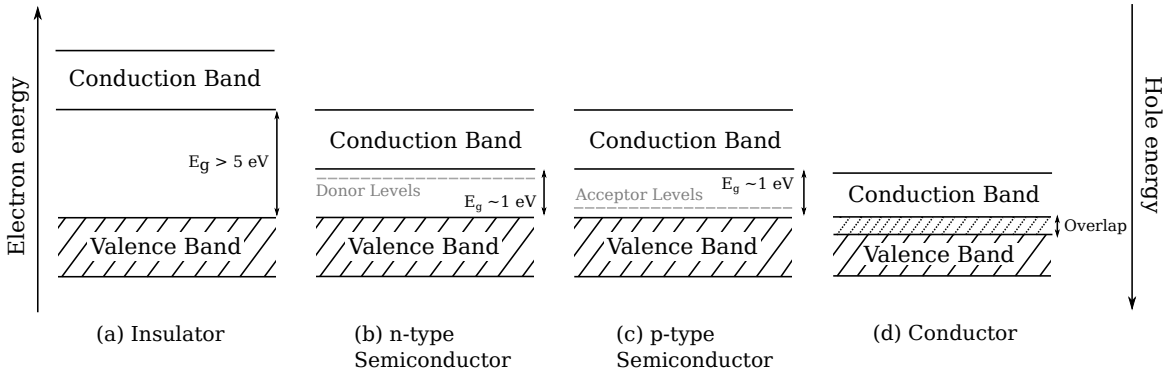

Figure 3.7: Schematic illustration of insulator, semiconductor and conductor energy band gaps.

Insulators have the largest energy band gap, with a minimum gap of 5 eV between the valence and conduction bands. They have a completely filled valence band and empty conduction band, meaning all the electrons are bound and the energy generated by thermal excitations is insufficient to promote electrons from the valence band. Semiconductors have a band structure similar to insulators, but a smaller band gap of ∼1 eV between the top of the valence band and the bottom of the conduction band allows thermal excitation of electrons. When a valence electron is excited into the conduction band, a positively charged vacancy is left in the valence band, called a hole. The excited electron and hole are known as electron-hole pairs and are the charge carriers in semiconductors. In conductors, the conduction band and valence band overlap, and there is no band gap. Intrinsic semiconductors have equal numbers of excited electrons n and holes p; $n = p$. Figure 3.7b and Figure 3.7c highlight the difference in p- and n-type semiconductors. Extra electron energy levels called donor levels sit beneath the conduction band in n-type, and extra hole energy levels sit above the valence band in p-type semiconductors. These extra electrons and holes are known as dopant impurities. Dopant impurities that add excess electrons $n > p$ to the material are called donors, and those that lack electrons (or add holes) $n < p$ are called acceptors. In n-type semiconductors, the electrons outnumber the holes and are therefore named majority carriers and the holes are the minority carriers. The converse applies in in p-type semiconductors. These donor impurities are often intentionally added during fabrication to alter the electrical

properties of the semiconductor material as a higher concentration of charge carriers increases conductivity.

3.5.2 Charge Carriers

When incident γ rays interact with the detection material, energy can be transferred to an electron in the valence band exciting it to the conduction band, which creates an electron-hole pair. The excited electrons are now mobile and can flow through the material. Neighbouring electrons can subsequently fill the vacant hole in the valence band, leaving a new hole in its original position that can also then be filled by an electron. This filling of holes gives the impression of the holes migrating through the material. A large number of electron-hole pairs are created. The number of electron-hole pairs N created is dependent upon the energy of the incident γ ray E_γ and the ionisation energy ϵ_{pair} of the detection material, as shown in Equation 3.12.

$$N = \frac{E_\gamma}{\epsilon_{pair}} \tag{3.12}$$

The ionisation energy ϵ_{pair} is the average energy required to produce one electron-hole pair. On average, 3 – 5 eV is required to produce an electron-hole pair in a semiconductor. By comparison, approximately 100 eV is required to produce a photoelectron from a PMT in a typical scintillator detector.

If the semiconductor crystal is placed between two electrodes and a potential difference is applied, an electric field $\mathcal{E}$ is produced. When ionising radiation interacts within the semiconductor crystal and electron-hole pairs are created, the negatively charged electrons and positively charged holes then migrate to the oppositely charged electrode where an electrical signal is induced on the contacts and read out. The motion of a charge carrier through the crystal can be influenced by diffusion and magnetic and electric fields, and the strength of this influence is characterised by the carrier mobility. Electron mobility is denoted μ_e and hole mobility is μ_h ($\mathrm{cm}^2/\mathrm{V{\cdot}s}$). The velocity v of a charge carrier can be expressed as:

$$v_{e,h} = \mu_{e,h}\mathcal{E} \tag{3.13}$$

Holes have reduced mobility, typically orders of magnitude smaller than electrons, as they cannot move as freely in the valence band and have a greater effective mass. The charge

transport properties of a semiconductor are also characterised by the electron and hole lifetimes, denoted τ_e and τ_h respectively. The charge carrier lifetime refers to the average time taken for a minority charge carrier (either electron or hole) to either become 'trapped' or to recombine with a charge carrier of the opposite charge. The presence of impurities, irregularities (e.g. dislocations) and structural defects (e.g. vacancies) in the crystal act as trapping centres. Often the charge carrier mobility and lifetime properties are expressed as a single parameter, denoted as either the electron $\mu_e\tau_e$ or hole $\mu_h\tau_h$ (cm^2/V) mobility lifetime product, and are key parameters in the development of radiation detectors.

3.5.3 Position Sensitivity

Position sensitivity can be achieved by segmenting or pixelating the negative (cathode) or positive (anode) electrodes. For radionuclide imaging, the segmentation is often in the form of square pixels. The electron-hole pairs that have been created travel along the electric field lines and induce a signal on the closest electrode. Pixelated detectors allow increased spatial resolution compared to planar detectors, and this effect improves as the pixel size decreases due to the small pixel effect [61]. The pixelated electrodes are bonded to a readout integrated circuit that reads out each pixel individually. Detectors using pixelated electrodes have several advantages including smaller leakage current, lower electronic noise, and lower capacitance per pixel electrode. Detectors with a pixel pitch of a few hundred μm have been reported [62, 63]. One drawback of pixelated detectors is that the device can suffer from charge sharing problems between pixels [64]. This occurs when the pixel size is decreased to be comparable in size to the electron charge cloud created when a γ ray interacts. The charge may be shared between multiple pixels or lost in the gap between the pixels, degrading the spatial resolution.

3.5.4 Cadmium Telluride and Cadmium Zinc Telluride

The two best semiconductors are generally considered to be silicon (Si) and germanium (Ge), with excellent resolution and charge transport properties. However, the low stopping power of Si means it is inefficient at detecting γ rays with energy over a few tens of keV [65], and the small band gap of Ge (0.66 eV at room temperature) mean cryogenic cooling is required to reduce thermal excitations. Therefore, room temperature semiconductors with high atomic numbers and a wide band gap have long been investigated for use as γ-ray detectors for

nuclear medicine. The most attractive semiconductors for use in gamma cameras include Cadmium Telluride (CdTe) and Cadmium Zinc Telluride ($Cd_{1-x}Zn_xTe$ where x = 0.1 – 0.2, or CZT). CdTe has been studied as an x-ray and γ-ray detector since the 1960's [66] and has been evaluated for medical applications since the 1970's [67]. CdTe combines high atomic numbers of 48 (Cd) and 52 (Te) giving a high quantum efficiency suitable for detecting γ rays typically in the 10 – 500 keV range [68]. CdTe and CZT are compound semiconductors, semiconductors that are composed of at least two chemical elements, with densities of 5.85 and 5.78 g/cm^3, respectively [68]. II-VI semiconductor compounds are composed of a metal from either Group 2 or 12 of the periodic table (the alkaline earth metals and Group 12 elements) and a non-metal from Group 16 (formerly called group VI). Cadmium and zinc are elements from Group 12 of the periodic table, while tellurium is Group 16. II-VI compound semiconductors generally have a wide band gap compared to Si and Ge and can therefore operate at room temperature without excessive thermally generated electronic noise.

CZT is one of the most promising materials for semiconductor detectors in nuclear medicine. It is formed by alloying CdTe with ZnTe, and is found to be better than CdTe for spectroscopic applications. Alloying CdTe with ZnTe increases the band gap from ∼1.45 eV in CdTe to around 1.6 eV in CZT [69]. CdTe can also suffer from noise due to leakage current, a small current that flows as there is not infinite resistance, degrading the energy resolution. This increase in band gap alongside the high electrical resistivity of CZT ($\rho = 10^9$ – 10^{11} Ωcm) [68] overcomes this. CZT crystals can be grown to larger sizes at a reduced but still expensive cost compared to CdTe and therefore CZT detectors are deemed more desirable than CdTe. The number of impurities or defects increases with increasing size of the crystals, therefore multiple small crystals are often tiled together in an array to increase the detection surface area. Good detection efficiency for γ rays above 300 keV requires the detectors to be 5 – 10 mm-thick. The ionisation energy is ∼5 eV for CZT, compared to around 100 eV in typical scintillator detectors meaning more charge carriers are produced from the primary ionisation event and the statistical fluctuation signal response is reduced. As shown by Equation 3.6 in Section 3.4.1, a reduction in ΔE_s improves the energy resolution of the detector.

The excellent statistics concerning charge carrier numbers are counterbalanced by effects that prevent complete charge collection. CZT detectors that are pixelated have boundaries

where signal collection is weaker than in the pixel centre. Compound semiconductors such as CZT are also characterised by poor charge transport properties due charge trapping and recombination, leading to incomplete charge collection. Typical values for mobility lifetime products in CZT materials are $\mu_h\tau_h = 10^{-6}$ – 10^{-4} cm^2/V and $\mu_e\tau_e = 10^{-3}$ – 10^{-2} cm^2/V [70]. As the CZT crystal thickness increases, a considerable amount of charge is lost due to the low mobility, long drift times and short lifetime of the charge carriers. Loss of signal at pixel boundaries and by hole trapping reduces the detectors charge collection efficiency, and the effect of this is characteristic tailing on the low energy side of the photopeak. Equation 3.6 illustrates a larger ΔE_{col} degrades the detectors spectroscopic performance.

3.5.5 Ohmic Contacts

CZT crystals are fabricated with very thin metalised electrode geometries deposited on the detector surfaces to extract the electrical signals. Due to their high resisitivity and low leakage currents ($<$ 10 nA at room temperature), CZT detectors are usually fabricated with ohmic contacts [70]. High work-function metals such as gold or platinum will form ohmic (charge injecting) contacts on p-type semiconductors, whereas low work-function metals such as indium will form ohmic contacts on n-type semiconductors. Ohmic contacts form an electrical junction between the metal and semiconductor that has a linear current-voltage (I - V) relationship, following Ohm's law [71]. A low resistivity would lead to high bulk leakage current, potentially greater than the current produced from radiation events in the detector. To overcome this, blocking contacts must be used. An example of a blocking contact is that produced from a p-n junction, typical in Si and Ge. The metal electrodes can be applied through either thermal evaporation, sputtering or electroless deposition [72]. The contacts are then bonded to readout electronics to read and process the electrical signals.

3.5.6 Application Specific Integrated Circuits

Application Specific Integrated Circuits (ASICs) have been developed to read out and process electrical signals from pixelated CZT radiation detectors [73, 74]. ASICs process information such as the amplitude and timing of the signal that is produced when charge is induced on either the cathode or pixelated anode. They contain a preamplifier that is designed to amplify the small output pulses (mV) from semiconductor detectors and match impedance between the detector and pulse processing electronics. The preamplifier must also operate

in a linear fashion; that is, the amplitude of the signal out must be directly proportional to the amount of charge delivered to it by the detector. This preserves the relationship between pulse amplitude and energy of the incident γ ray and is achieved by using a charge sensitive preamplifier. The charge Q is collected on a capacitor C_i. The charge pulse is then integrated onto a second capacitor C_f and discharged via a feedback resistor R_f. The output voltage from the preamplifier has amplitude V_{out}:

$$V_{out} = \frac{Q}{C_f}. \tag{3.14}$$

The output pulse from a preamplifer is characterised by a fast rise time (a few µs) and long exponential decay time (typically 50 – 100 µs). The rise time is determined by the charge collection time in the detector, while the decay time is determined by the time constant ($\tau = R_f C_f$) of the shaping circuit. As long as τ is long compared to the duration of the input pulse, the output voltage is proportional to the total integrated charge in the pulse. The pulse is then processed by an shaping amplifier. The shaping amplifier further amplifies the still relatively small pulses from the preamplifier to a sufficient amplitude (V), and subsequently shapes it into a Gaussian-shaped pulse. This removes the long pulse tail that can cause pulses to pile up on the tail from a preceding pulse. The PMTs used to process the signals in conventional gamma cameras occupy considerable volume and must be surrounded by lead. Semiconductors that are read out by ASICs eliminate the need for PMTs and therefore have considerable advantages in weight and manoeuvrability for use in a SPECT system.

3.6 SPECT Activity Quantification

As detailed in Section 2.3, accurate measurements of the activity distribution within a well-defined volume are essential for performing patient dosimetry, leading to to the need for absolute quantification with SPECT [75]. Ideally this would be achieved by: imaging the volume of interest within the patient using SPECT, correcting for the factors that degrade the image, obtaining a measured count rate distribution within the volume and finally calibrating this to obtain a measured activity distribution, as illustrated in Figure 3.8. This process would be repeated at multiple time points to obtain a time-activity curve and a value of cumulative activity.

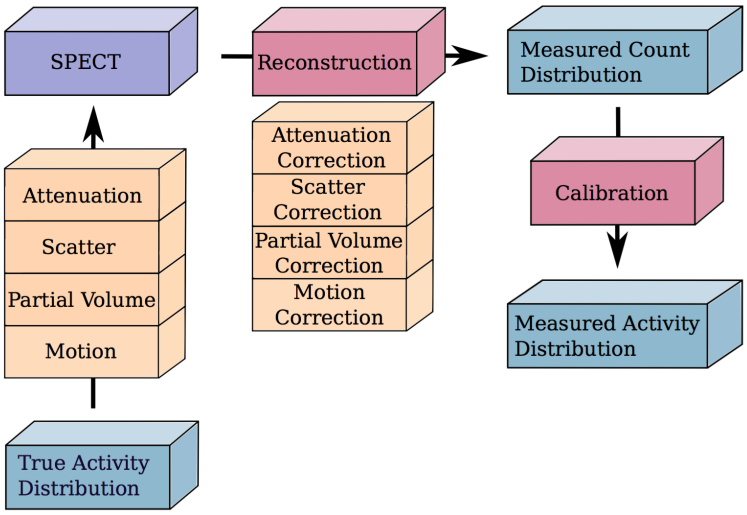

Figure 3.8: Illustration of a simplified image formation chain, reproduced from [76].

The following sections describe the factors that degrade SPECT image quality and lead to loss of true activity information.

Attenuation

Attenuation, the loss of γ rays due to absorption or scattering, will prevent γ rays from leaving the body and reaching the detector leading to an underestimation of the activity within the body. The reduction in the number of detected γ rays varies with the thickness and the nature of the material through which the γ rays must travel before being imaged. The amount of attenuation is also energy dependent, with greatest attenuation occurring at lower γ-ray energies. The linear attenuation coefficient of soft tissue is 0.11 cm^{-1} at 364.5 keV, therefore Equation 3.5 shows γ rays that are emitted from a depth of 2 cm (the approximate thickness of tissue covering the thyroid gland is 1 – 3 cm [77]) would have a probability of 80% of emerging from the body in their original direction. For ^{99m}Tc where the linear attenuation coefficient is 0.15 cm^{-1}, this falls to 74%. The aim of attenuation correction is to recover the lost events.

Scatter

Unlike attenuation correction where the aim is to recover the attenuated events to determine activity, the aim of scatter correction is to remove the scattered events to improve image quality. Compton scattering is the dominant interaction process in soft tissue ($Z_{\text{eff}} = 7.4$) for

γ rays with energy between 40 keV to 10 MeV. γ rays that are scattered either whilst leaving the body of the patient or within the collimator do not represent the true position in which the γ ray originated in the body, compromising the ability to obtain a precise map of the radioactivity distribution. If a γ ray scatters in the body or collimator, it cannot deposit all its original energy in the detector. Therefore, an energy window can be used to remove these scattered events. Typical scintillator SPECT systems have an energy resolution of $\sim$10% [78], therefore during imaging an energy window of width 15% – 20% centred around the photopeak is recommended [79]. Only these events within the energy window will be used for imaging. An example ^{131}I energy spectrum with a 20% (328 – 400 keV) energy window is illustrated in Figure 3.9a. Although it is important to have an adequately wide energy window to avoid excessive count losses, γ rays that are Compton scattered through small angles within the body can also be recorded within the photopeak window, degrading the signal-to-noise ratio. This is a more significant problem with 140.5 keV γ rays, compared to 364.5 keV, as for an energy window of 20% (127 – 155 keV) γ rays scattered up to 50° will fall into the energy detection window and will be accepted. For 364.5 keV, only γ rays scattered up to 30° will be accepted into a 20% energy window. However, multiple Compton scattering processes are more likely at higher energies, and these scattered events may also be accepted into the ^{131}I energy window. Improved detector energy resolution is required to discriminate photopeak events from unwanted scatter. Down-scatter is also an issue if the nuclide emits γ rays higher in energy than the γ ray of interest and is a problem with ^{131}I due to the presence of 637 keV (7.2%) and 723 keV (1.8%) γ rays. Scattering degrades the signal-to-noise ratio and hence the contrast in the image, as the Compton scattered γ rays will give an increased background signal that is closer to that of the absorbed γ rays. As CZT has better energy resolution compared to NaI(Tl) scintillator detectors, a smaller energy window can be set. Figure 3.9b shows a ^{131}I spectrum acquired with a CZT detector and a 5% energy window (355 – 375 keV) highlighted around the 364.5 keV photopeak.

Partial Volume and Motion

Partial volume effects occur when the region of interest (e.g. tumour) is smaller than approximately twice the FWHM of the spatial resolution. Objects smaller than the resolution volume will have all their counts detected, but over a larger volume than their true size. The counts will be 'spread out', thus the recorded concentration of activity will be lower

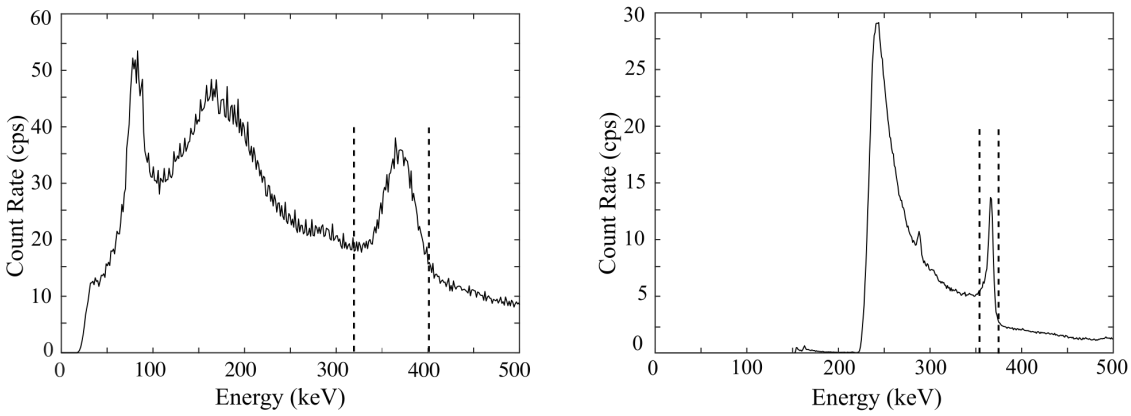

Figure 3.9: ^{131}I γ-ray spectra acquired with (a) a NaI(Tl) scintillator gamma camera with 20% ($\pm$ 10%) energy window around the 364.5 keV photopeak and an energy threshold set at 25 keV and (b) a CZT detector with 5% ($\pm$ 2.5%) energy window around the 364.5 keV photopeak and an energy threshold of 220 keV.

than the actual concentration. Improvements in the spatial resolution of a system can help avoid partial volume effects. Patient movement during data acquisition due to respiratory or cardiac motion can cause aretefacts in the reconstructed 3D image of the organ. This can be corrected for with sufficiently long scanning times and a large number of projection images acquired during the SPECT scan.

3.6.1 Limitations for ^{131}I Imaging

Further problems arise with obtaining accurate quantitative activity information following therapeutic applications such as MRT, as current gamma cameras are optimised for diagnostic imaging with low-energy radionuclides such as ^{99m}Tc, not high-energy therapeutic radionuclides such as ^{131}I. At high energies, the performance of gamma cameras with standard 9.5 mm-thick NaI(Tl) crystals is limited by decreasing detection efficiency as well as increasing collimator septal penetration. Alongside this, poor image quality arising from poor system spatial resolution and energy resolution leads to uncertainties in volume delineation and errors in the measured values of activity. As SPECT systems are also optimised for imaging following the administration of activities up to a maximum of $\sim$900 MBq in diagnostic procedures, they suffer from count rate saturation when imaging following therapy. The effects of dead time on quantitative SPECT with commercial systems have been reported with therapeutic activities of 2 – 6 GBq of ^{131}I [80], and this is an issue as typical adminsitered

activities of ^{131}I in MRT can be up to 7.4 GBq. ^{131}I has multiple high-energy γ-ray emissions that will also contribute to dead time, even when they are outside the acquisition energy window [81]. As mentioned in Section 2.3.2, often when imaging after the administration of several gigabecquerels of activity there is a limit placed on the earliest imaging time point of around a couple of days after injection due to the effects of camera dead time [82]. This means an accurate initial calculation of the activity distribution cannot be performed. Quantitative activity information is therefore lost due to this dead time leading to uncertainties in absorbed dose calculations.

3.6.2 Reconstruction Algorithms

The final stage in SPECT imaging is the implementation of a reconstruction algorithm to achieve 3D images from the acquired 2D projection images. In general, there are two groups of reconstruction methods used to obtained a 3D radiation distribution from 2D projection images: iterative and analytic methods. The most conventional method and an example of an analytic technique is Filtered Back Projection (FBP). However for quantitative studies, iterative methods such as Ordered Subset Expectation Maximisation (OSEM) [83] or Maximum Likelihood Expectation Maximisation (MLEM) [84] are required. These methods include explicit corrections for the factors detailed in Section 3.6 that degrade the quantitative accuratry of a SPECT image. Most iterative algorithms fit into the general model following the image (projection) acquisition process of: generating a simple initial guess of the image, estimating a set of projection data from the initial estimate using a mathematical process called forward projection (it is in this step where corrections can be made) and comparison of the resulting projection with measured projection data, with the difference between the two used to update the estimated image. The iterative process is repeated until a condition predefined by the algorithm is satisfied and the final image is generated that closely matches the true distribution in the 3D structure [85, 86]. Iterative reconstruction methods have been found to offer both superior image quality [87] and potentially quantification [88] compared to FBP, at the expense of being more computationally intensive. OSEM is a simple modification of the MLEM algorithm and works by breaking up the full set of projection data into a series of mutually exclusive subsets and applying the algorithm to each subset sequentially [72]. This is often achieved in far fewer iterations compared to MLEM. Due to its speed, the OSEM algorithm has quickly become the reconstruction method of choice in nuclear medicine [89].

Chapter 4

CZT Detector Characterisation

Pixelated CZT has been shown to possess superior qualities, including improved energy resolution and position resolution, compared to the scintillator detectors typically used in clinical gamma cameras [90] [91]. A pixelated CZT detector was therefore selected for use in the DEPICT project for investigating the feasibility of obtaining quantitative activity information following MRT. This chapter will discuss the DEPICT CZT detector characterisation involving investigations into the following:

- Electronic noise
- Operating voltage
- Linearity
- Stability
- Peaking time
- Dead time

Optimisation of these performance parameters will allow the detector to meet the high γ-ray throughput and good energy resolution requirements of the DEPICT project.

4.1 DEPICT CZT Detector

The DMatrix Nuclear Imager [92], manufactured by eV Products, is a fully integrated, γ-ray counting, pixelated, 12-bit energy discriminating CZT detector. Its end-user applications include gamma spectroscopy for nuclear security and as a SPECT demonstrator in the medical

industry. The CZT detectors and associated electronics are encased in aluminium, shown in Figure 4.1a, to allow shielding from visible light that would otherwise induce noise. The fundamental building block of the DMatrix, shown in Figure 4.1b, is an array of four (2 x 2) CZT detector modules each coupled to an ASIC (to process and read out the signals), analogue-to-digital converters (ADCs) and an aggregator field programmable gate array (FPGA). The design enables large field of view scaling by tiling multiple 2 x 2 modules. Each individual CZT crystal is 22 x 22 x 5 mm with 11 x 11 pixels at 2 mm pitch, illustrated in Figure 4.1c, allowing high count rate operation. Highlighted in grey are two pixels that are exessively noisy in the DEPICT CZT detector, and therefore were manually switched off for all data collection. Each ASIC, which is based on the H3D ASIC [93], has 128 anode channels (121 used) for anode pixels and 2 cathode channels (1 used) which perform charge amplification and shaping, and provide energy and timing information. The anode and cathode channels utilise charge sensitive preamplifiers[1] with adaptive reset, a 5^{th} order unipolar shaping amplifier, baseline stabiliser and discriminator with trimming. After shaping, the analogue outputs of the ASIC are digitised. The 2 x 2 modules communicate with the aggregator FPGA over a low-voltage differential signaling (LVDS) tether where data are formed into packets. These packets are received by a PC where the DMatrix Application Programming Interface (API) decodes them, and presents the end-user with list-mode data. These data include the detector module number, individual pixel number, uncalibrated γ-ray energy and time stamp. Software was written in MATLAB [94] that produces a user-friendly graphical user interface (GUI) that allows the raw list-mode data to be input alongside a calibration file. Individual γ-ray spectra (calibrated or uncalibrated) can then be viewed for each pixel, alongside a 'sum' spectrum produced by binning all single pixel events into one spectrum. In addition, the data can be viewed as a 2-dimensional intensity map or 'pixel map', where each square pixel has a colour assigned to it, depending on the total counts in the individual pixel spectra. For the 2 x 2 detector configuration, Gigabit Ethernet is sufficient for communication with a PC. A carbon fibre window covers the active area of the detector at a height of 1.36 cm from the closest face of the detector, and this can be removed to allow a mechanical collimator to be mounted.

[1] Rise time $\sim$ 50 ns

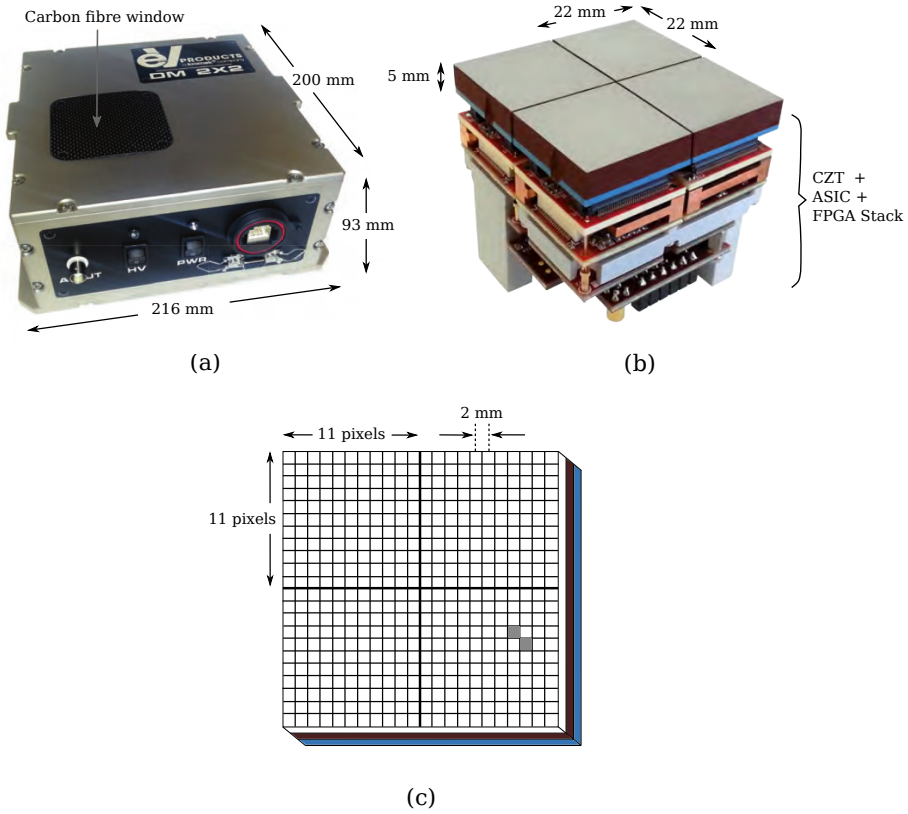

Figure 4.1: Photograph of (a) DMatrix Nuclear Imager external housing, (b) DMatrix fundamental building block with four individual CZT detector modules, ASICS, ADCs and an FPGA and (c) illustration of the pixelation of the CZT crystals.

4.2 Detector Characterisation

Measurements were undertaken to optimise and evaluate the performance of the DEPICT CZT detector for MRT applications, by determining settings that facilitate good energy resolution and high γ-ray throughput. Good energy resolution is required to discriminate γ rays that are scattered as they are emitted from the body and within the collimator before reaching the detector face. High throughput is essential due to the high activities of radionuclides administered in MRT. The DMatrix 'basic sparsified photon collection mode' was used, which entails only collecting data from the anode channels that exceed a user-defined threshold. For a pixel to trigger data readout, its voltage pulse height must be greater than the threshold set in mV for that pixel, which is adjustable by a 10-bit DAC. A global threshold sets the same value for all pixels, and a threshold of 380 mV was applied that was calculated to be equivalent to ~15 keV. The threshold was used to remove electronic noise contributions at low energy, and characteristic low-energy x-rays.

4.2.1 Electronic Noise

An internal digital test pulser was used to estimate the electronic noise contribution to the total energy resolution, allowing noise contributions from charge production and collection to be excluded. Pulser circuitry is internal to the ASIC and charge is injected to the front of the preamplifier. A typical pulser peak from a single pixel is shown in Figure 4.2. The pulser amplitude is controlled by a 10-bit DAC in the ASIC. A test pulse of amplitude 185 mV was induced for 60 seconds, allowing a peak in each pixel to be produced with approximately 20,000 gross counts. Data were collected and the position and FWHM of the pulser peak were noted in four typical pixels from each of the four detector modules. This allowed an average FWHM for each individual module to be calculated. The average FWHM over all the detector modules was then calculated to be 3.32 $\pm$ 0.22 keV. Electronic noise of around 3 keV in pixelated CZT detectors have been reported in [63, 95].

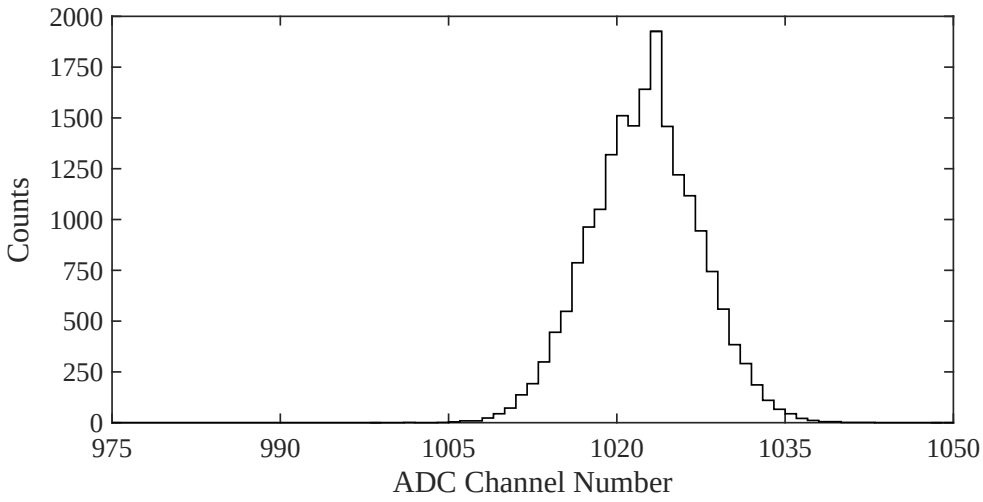

Figure 4.2: Example pulser peak from a single detector pixel.

4.2.2 Energy Resolution as a Function of Operating Voltage

Measurements were made at bias voltages between 300 V to 1000 V, in steps of 100 V, to determine the voltage that produced the best energy resolution of an ^{131}I 364.5 keV photopeak. A skewed Gaussian fit is required for calculation of the FWHM due to low-energy tailing on the photopeak, which is characteristic of incomplete charge collection in the CZT detector due to hole trapping [96, 97]. The least-squares peak-fitting programme GF3 [98] was utilised to apply a skewed Gaussian fit to the photopeak. Figure 4.3 shows ^{131}I photo-

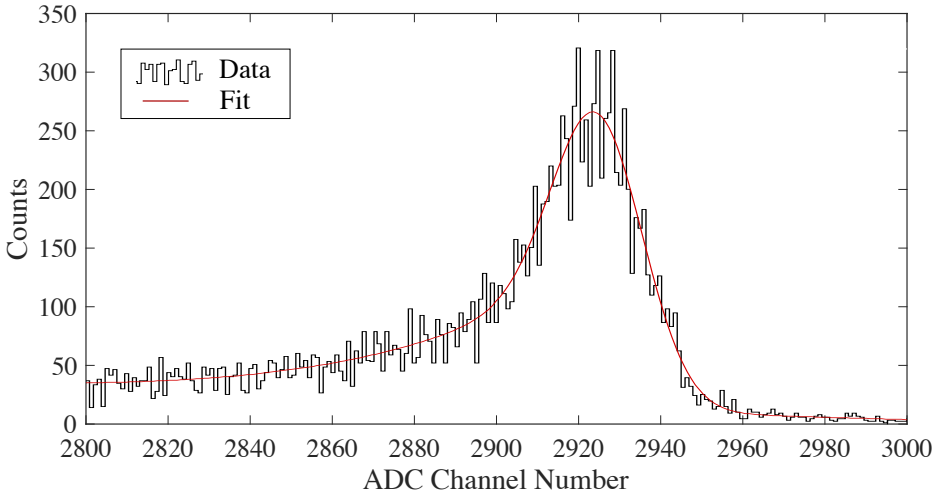

Figure 4.3: Example GF3 fit to skewed ^{131}I photopeak generated from a DEPICT detector pixel at 600 V.

peak data generated from a DEPICT detector pixel at 600 V in black, and the fit illustrated by the smooth red line.

Photopeak centroid positions and FWHM values were measured in ADC channel numbers at each bias voltage. The data plotted in Figure 4.4 show the FWHM (%) of a photopeak from a single pixel, and from the sum spectra produced by binning all single pixel events in one spectrum. The FWHM (%) was calculated using Equation 4.1.

$$\text{FWHM (\%)} = 100 \times \frac{\text{FWHM (ADC channels)}}{\text{photopeak centroid position (ADC channel)}} \tag{4.1}$$

The results presented in Figure 4.4 demonstrate that as the voltage is increased from 300 V to 600 V, the FWHM (%) for a single pixel decreases from 7.8% to 2.9%, due to improved charge collection. However, as the bias voltage is increased above 600 V, the FWHM (%) degrades due to increasing leakage current. Although the FWHM measured at each bias voltage is larger than the summed pixel spectra, decreasing from 10.3% to 6.5% across 300 to 600 V, the trend is reproduced with the best energy resolution again being achieved at 600 V. The operating voltage of 600 V was therefore selected as the optimum and will be set for all future measurements.

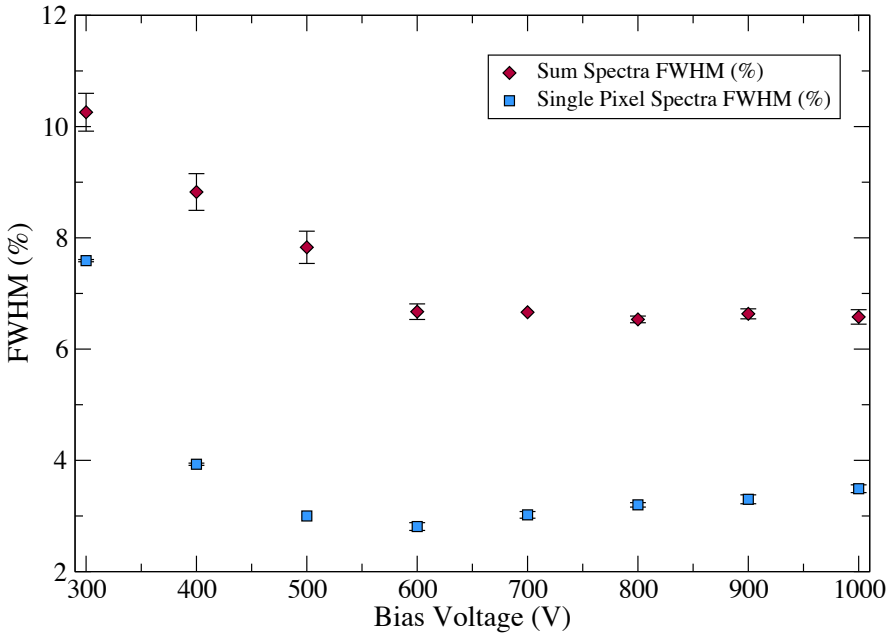

Figure 4.4: FWHM (%) calculated for a ^{131}I photopeak produced in a single pixel (blue) and from summing all individual pixel spectra (red) as a function of bias voltage.

4.2.3 Detector Linearity

Data were acquired with ^{241}Am (59.5 keV γ ray, 179.5 kBq), ^{133}Ba (81, 356 keV γ rays, 138.9 kBq), ^{57}Co (122 kev γ ray, 343.3 kBq) and ^{139}Ce (165.9 keV γ ray, 26.4 kBq) point sources and an ^{131}I (364.5 keV γ ray, $\sim$8 MBq) distributed source to determine if the detector and associated electronics were linear in energy response and to apply any corrections, if necessary. The energy range provided by these sources [99, 100] corresponds to the energy region of interest for the DEPICT project ($<$ 364.5 keV). The gain on the anode channel can be set to one of four values in the ASIC; 20, 40, 60 and 120 mV/fC, so these were investigated to optimise the use of the dynamic range. The sources were sequentially placed 4 cm from the carbon fibre window for 600 seconds at each gain setting.

Figure 4.5 shows the ADC channel number of the measured photopeak centroid plotted as a function of known γ-ray energy for all acquired data sets. The 20 mV/fC setting was found to decrease the dynamic range such that with the global threshold applied, no spectrum could be collected for these sources. Therefore, data were only acquired at the three higher settings. It can be seen that the energy response is linear below 364.5 keV for all three gain settings. A linear calibration can therefore applied across the energy range. A calibration file

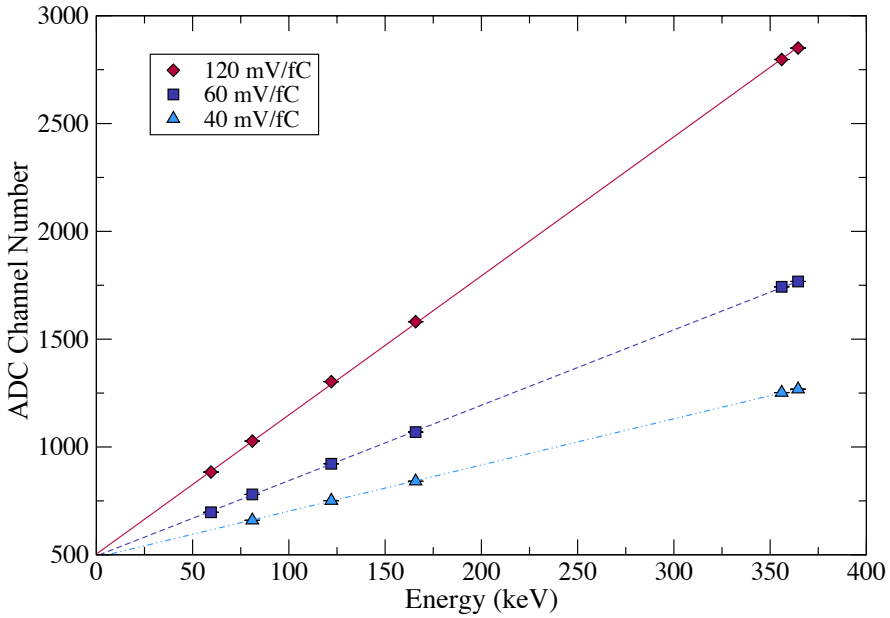

Figure 4.5: Measured ADC channel number of various photopeak centroids as a function of known γ-ray energy.

was created using the MATLAB GUI. The user input list-mode data acquired with sources known to have γ emissions across the energy region of interest (^{241}Am - 60 keV and ^{133}Ba - 81, 277, 302, 356 and 384 keV). The user was then able to match the uncalibrated channel number to the known γ-ray energy. A text file was then output with two columns of values; the first column contained values of m, and the second values of c, to convert every channel into an a value of keV using $y = mx + c$. Figure 4.5 shows the intercept at ADC channel 500, which is due to a known baseline offset of 230 mV in the pulses and is highlighted in Figure 4.8. The dynamic range is known to be approximately 2 V from this baseline and the total range consists of 4096 channels. The 120 mV/fC setting is optimum in this energy region as the data best fills the dynamic range and will be used for all measurements.

The deviation (%) of the measured ADC channel from the ADC channel calculated from the linear fit for the 120 mV/fC data is plotted in Figure 4.6. The equation of the linear fit for the 120 mV/fC data in Figure 4.5 is $y = 6.43x + 509.2$. The measured ADC channel numbers for all energies are within $\pm$ 0.5% of the calculated ADC channel numbers. The maximum energy that can be resolved at this gain setting has been calculated to be 558 keV, however it is unlikely that the detector would have suitable efficiency at detecting γ-ray energies above 364.5 keV due to the 5 mm crystal thickness.

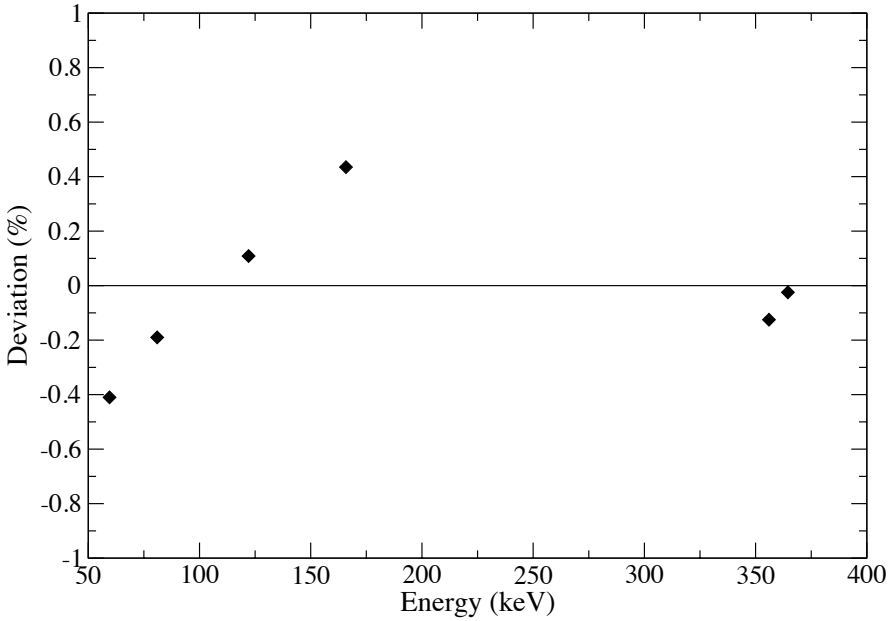

Figure 4.6: Deviation (%) of measured photopeak ADC channel from ADC channel calculated from the linear fit at the chosen gain setting of 120 mV/fC.

4.2.4 Detector Stability

A medical imaging detector is required to behave consistently throughout the day in a hospital, as patient images need to be reproducible and comparable. Data were therefore acquired to investigate the stability of the detector by measuring the position of a ^{133}Ba photopeak (ADC channel number) and FWHM (%) as a function of temperature. ^{133}Ba is often used a surrogate for ^{131}I as it emits a 356 keV γ ray, which is comparable in energy to the 364.5 keV ^{131}I γ ray. It also has a much longer half-life (10.51 years compared to 8.02 days) making it practical for experimental data collection. The DMatrix software provides a reading of the temperature of each detector module. The detector was switched on and the average temperature of the four detector modules was noted. The detector was left switched on, increasing the temperature of the detector over time, and a ^{133}Ba energy spectrum was acquired at various temperatures. The FWHM (%) of a ^{133}Ba photopeak and the photopeak centroid position (ADC channel number) as a function of temperature is plotted in Figures 4.7a and 4.7b.

It was found that both the FWHM (%) and photopeak centroid position increased with increasing temperature. The FWHM (%) increased from 2.94% to 3.66% with a 10°C increase in temperature and the photopeak centroid position increased by 20 channels, corresponding

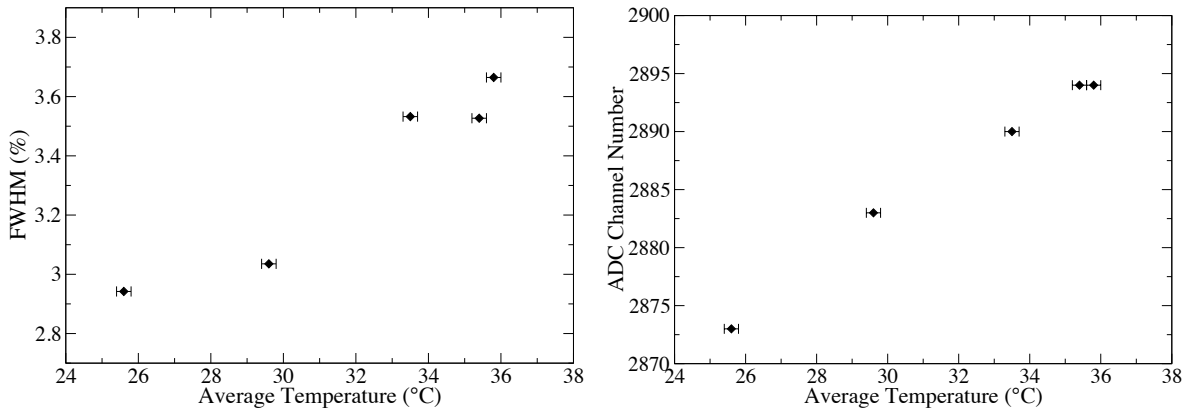

(a) (b)

Figure 4.7: (a) FWHM (%) of ^{133}Ba photopeak as a function of temperature (b) ADC channel number of ^{133}Ba as a function of temperature.

to ∼3 keV. An increase in temperature decreases the band gap, allowing more electrons to become excited from the valence band to the conduction band. This increase in the number of electrons N shifts the photopeak position to a higher ADC channel as the number of electrons N produced is directly proportional to incident γ-ray energy. The equation $FWHM = 2.35\sigma$ where $\sigma = \sqrt{N}$ shows that the energy resolution is also directly proportional to the number of electrons N produced. Therefore, at higher temperatures, the energy resolution will degrade. In addition this decrease in band gap will allow thermal excitation of electrons that will induce a signal when a γ ray has not actually interacted within the detector crystal, increasing the noise in the detector and decreasing the signal-to-noise ratio. The detector's internal cooling fans were therefore switched on for all data collection to reduce this photopeak shift and improve the energy resolution. The temperature variation measured over 3 hours with the fans on was 0.4 °C.

4.2.5 Peaking Time

To determine the energy of an incident γ ray, the voltage pulse produced by the detector must be shaped. The amount of shaping depends on the time allowed for a shaped pulse to reach its maximum amplitude, known as the peaking time. If the pulse width is too large, there will be pile-up of successive pulses. Reducing the peaking time allows the first pulse to return to the baseline before a second pulse arrives, but if the peaking time is shorter than the charge induction time on the anode pixel, the signal will be shaped before the full charge has registered, resulting in ballistic deficit. Four peaking time values can be set by the user in

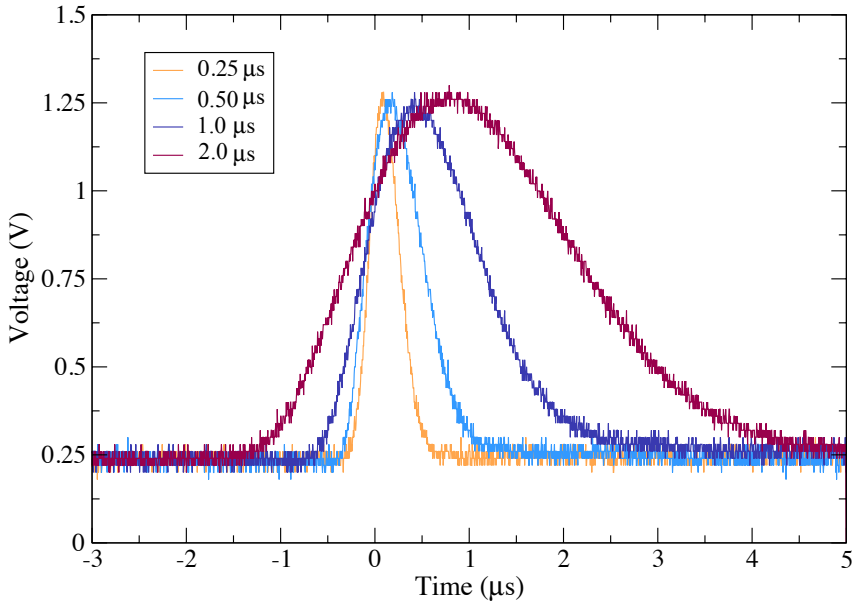

Figure 4.8: Shaped pulses at peaking times of 0.25, 0.50, 1.0 and 2.0 µs. The 230 mV offset of the pulses from the baseline is evident.

the ASIC; 0.25, 0.50, 1.0 and 2.0 µs. Figure 4.8 illustrates the shaped pulse produced at each peaking time. The signals were acquired by connecting the detector an oscilloscope, allowing analogue signals to be directly monitored, bypassing the D-Matrix readout electronics. The pulse width increases with increasing peaking time. The 230 mV baseline offset of the pulses is evident.

The energy spectra acquired at each peaking time are shown in Figures 4.9a-d. The energy resolution (FWHM %) of the ^{131}I 364.5 keV photopeak from a single pixel was measured to be 8.66 ± 0.05%, 2.94 ± 0.02% and 4.56 ± 0.21% at peaking times of 0.25, 0.50, and 1.0 µs respectively. At 2.0 µs peaking time, the photopeak was no longer resolvable. It is known that lowering the threshold helps to recover the spectrum at the longer peaking time, although this is not desirable for the high count rate application of DEPICT. The best energy resolution of 2.94 ± 0.02% was observed at a peaking time of 0.50 µs, therefore this setting will be used for subsequent measurements. In Figure 4.9b, the photopeak centroids are labelled. The 80.2 keV ($P_\gamma = 2.6\%$), 284.3 keV ($P_\gamma = 6.1\%$) and 364.5 keV ($P_\gamma = 81.7\%$) ^{131}I photopeaks are clearly identified. There are multiple unresolvable low-energy x-rays with energies between 29.5 – 34.5 keV, and a combined intensity of approximately 4.86%. For comparison, the typical energy resolution for NaI(Tl) scintillator detectors currently used

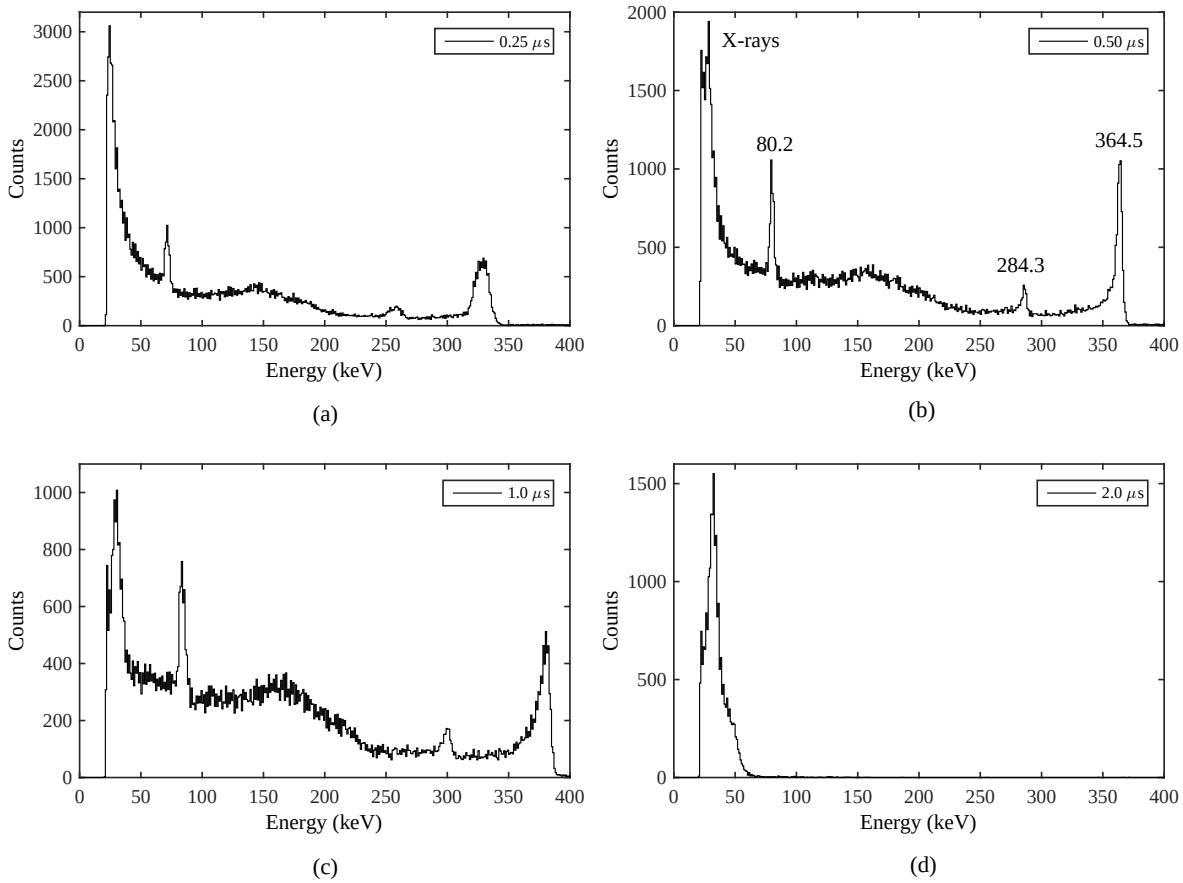

Figure 4.9: Example ^{131}I energy spectra acquired at peaking times of (a) 0.25 μs, (b) 0.50 μs, (c) 1.0 μs and (d) 2.0 μs. Figure 4.9 has the photopeak centroids labelled.

in SPECT systems is approximately 10% FWHM at 364.5 keV. The superior CZT detector energy resolution will facilitate improved scatter correction over scintillator SPECT systems, improving quantitative imaging and volume delineation, which are key aims of the DEPICT project.

The setup parameters of bias voltage and peaking time have been selected so far to optimise energy resolution for discrimination of scattered γ rays. However, the DEPICT project also requires the detector to operate with high γ-ray throughput, due to the high activities of nuclides administered in MRT. This could potentially be achieved by reducing the peaking time. Therefore, the γ-ray throughput was compared at peaking times of 0.25 and 0.50 μs. The detector was exposed to a 3.54 MBq ^{133}Ba point source for measurement periods of 300 seconds, at a range of distances from 0 cm (on the carbon fibre window) to 14 cm, to vary the incident count rate. The incident count rate was calculated using the activity of the

source, the time taken for data collection and a solid angle Ω correction for a square detector shown in Equations 4.2 and 4.3, at each distance.

$$\Omega = (1 - f_s) \cdot 4 \cdot arcsin\,(sin^2\,\alpha) \tag{4.2}$$

where

$$\alpha = arctan\left(\frac{w}{2d}\right) \tag{4.3}$$

and where f_s is a pre-factor to account for any physical shadowing of the detector area by ancillary windows, w is the active width of the detector and d is the distance from the detector to the source [101]. A ^{133}Ba point source was used for this measurement due to the uncertainties that would arise in the solid angle correction to be applied to the ^{131}I distributed source. The measured count rate was determined from the total counts in the sum spectra at each source distance, and is shown as a function of the incident count rate for data acquired at peaking times of 0.25 and 0.50 µs in Figure 4.10. The error on the measured γ-ray count rate is statistical, whereas the error on the incident count rate takes into account geometrical uncertainties. The results show reducing the peaking time to 0.25 µs slightly decreased the γ-ray throughput, which may be due to ballistic deficit effects. Since the peaking time is not the limiting factor for throughput, the detector can be operated at 0.50 µs to ensure best spectroscopic performance.

4.2.6 Dead Time

The dead time of a SPECT system has always been a main limitation for quantitative imaging in MRT and it is therefore essential to minimise this where possible. ^{131}I is a complex gamma emitter as it emits γ rays both lower and higher in energy than the main 364.5 keV photopeak, shown in Figure A.1, that will all contribute to dead time. If large count losses occur due to dead time, the scaling from measured counts to activity by a calibration factor will underestimate the activity and the absorbed dose to the patient [34]. Figure 4.10 shows the measured count rate versus incident count rate for the DEPICT detector when exposed to a ^{133}Ba source. The data have a non-linear relationship and appears to be entering a plateau region, indicating the detector behaviour follows a non-paralysable model for dead time. In order to confirm that the detector does follow a non-paralysable model, it is necessary to calculate the detector dead time τ. To calculate τ, the minimum time interval that two consecutive counts must be separated in order to be recorded as two different events, the

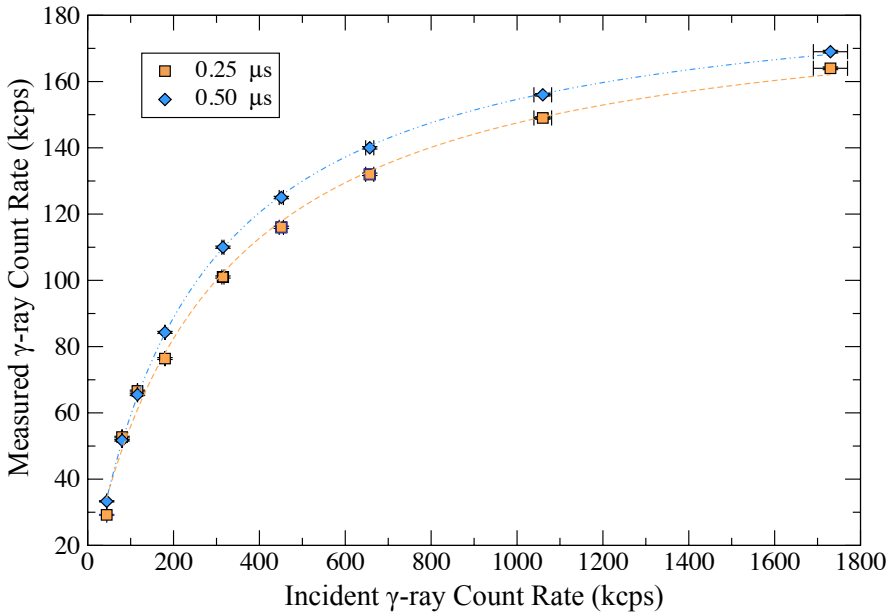

Figure 4.10: Measured γ-ray count rate as a function of incident γ-ray count rate at peaking times of 0.25 and 0.50 µs.

two-source method [47] was used. Two ^{133}Ba point sources with activities 3.54 MBq and 0.95 MBq were used at the optimised peaking time of 0.50 µs, to calculate the detector dead time. The two-source method is based on observing the counting rate from two sources individually and in combination. Because the counting losses are non-linear, the observed rate due to the combined sources will be less than the sum of the rates due to the two sources counted individually, and the dead time can be calculated from the discrepancy. The count rates and hence the system dead time was measured with the sources placed at 8 cm above the carbon fibre window. Each measurement was acquired for 600 seconds. A background measurement with both sources removed was also acquired. The dead time τ of the system can be calculated from the following equation:

$$\tau = \frac{X(1-\sqrt{1-Z})}{Y} \tag{4.4}$$

where

$$X \equiv m_1 m_2 - m_b m_{12}, \tag{4.5}$$

$$Y \equiv m_1 m_2 (m_{12} + m_b) - m_b m_{12}(m_1 + m_2), \tag{4.6}$$

$$Z \equiv \frac{Y(m_1 + m_2 - m_{12} - m_b)}{X^2}, \tag{4.7}$$

and where m_1 = measured count rate of source 1, m_2 = measured count rate of source 2, m_{12} = measured count rate of sources 1 and 2 combined and m_b is a measure of the background counts. The values for m_1, m_2, m_{12}, m_b and τ are shown in Table 4.1. The dead time τ was calculated to be 4.87 ± 0.18 µs.

m_1 (cps)	m_2 (cps)	m_{12} (cps)	m_b (cps)	τ (µs)	Error (µs)
6.43 x 10^4	2.36 x 10^4	7.59 x 10^4	3.29 x 10^1	4.87	0.18

Table 4.1: Values used for calculation of dead time τ.

If the detector is non-paralysable, it is known the system will approach an asymptote for a measured count rate of $1/\tau$, which represents the situation in which the device essentially just completes one dead time period before starting another. In the paralysable case, the measured count rate reaches a maximum value at an incident count rate of $1/\tau$, before the measured count rate starts to decrease with increasing incident count rate, as illustrated in Figure 3.6. For the DEPICT system, $1/\tau$ is equal to just over 205 kcps. Above an incident count rate of 205 kcps, the data do not fall off (decrease with increasing incident count rate) confirming it follows a non-paralysable model. The measured count rate will tend towards an asymptotic value of 205 kcps. Using Equation 3.10, it was determined that a measured count rate of 205 kcps would be reached at 30,000 kcps for a dead time τ of 4.87 µs. When the detector enters a plateau region and there is no unique correlation between the measured and incident count rate, it is not possible to apply corrections. Therefore, a measured count rate of 160 kcps was chosen as the maximum operating count rate as it is still possible to correlate to the incident count rate. This maximum operating count rate will used in the design of a high-energy parallel-hole collimator for the DEPICT system. The development of the collimator is discussed in Section 5.1.

4.3 Summary of Characterisation Measurements

The characterisation measurements undertaken in this chapter ensure the detector has been optimised for therapeutic imaging. Internal cooling fans were switched on and a reverse bias voltage of 600 V, gain setting of 120 mV/fC, peaking time of 0.5 µs were selected to give optimum energy resolution and γ-ray throughput. The detector was characterised as following a non-paralysable dead time model and the dead time was calculated to be 4.87 µs.

Often, characterisation of pixelated detectors involve an investigation into charge sharing. That is, measurement of the proportion of charge that gets shared between neighbouring pixels, degrading the spatial resolution. Data were acquired to ascertain the charge sharing suffered in the DEPICT detector, however a ^{241}Am source was used. The energy of the γ rays emitted by ^{241}Am (60 keV) is much lower than that of ^{131}I and therefore the value of the charge that gets shared would not be representative of that when using the detector for radioiodine MRT and is therefore not included here. The methodology followed has however been included in Appendix A.2 for completeness.

Chapter 5

Phantom Imaging

A medical imaging system with good image quality is essential for patient dosimetry. A clear image with contrast between regions with different activity uptake is needed for area delineation and calculation of activity within a region of interest. Medical imaging phantoms are used to evaluate the performance of imaging systems, such as clinical gamma cameras. Phantoms can be designed for testing detector performance characteristics, such as system spatial resolution. Alternatively, they can be made to resemble organs or anatomical features with materials that mimic the attenuating properties of human tissue. In order to evaluate the imaging capability of the DEPICT system, data were acquired with ^{131}I at various activities and with a mix of phantoms. Table 5.3 summarises the aims of the imaging tests performed in this chapter and the type of phantom used to achieve each aim. The custom designed DEPICT collimator will also be described in this chapter as it is used to produce images of line, Jaszczack and thyroid phantoms. In this chapter, data were also acquired with a Siemens Intevo gamma camera at The Royal Marsden Hospital, to allow comparison of some phantom data sets acquired with DEPICT.

Aim	Phantom
Acquire a matrix of uniformity factors	Uniformity
Determine system spatial resolution	Line
Perform area delineation	Jaszczak
Acquire a thyroid image and resolve features of differing activity	Thyroid

Table 5.1: Experimental aims with associated phantom type.

5.1 Custom-Designed Parallel-Hole Collimator

As detailed in Section 3.3, collimators are an integral part of a γ-ray imaging system and are essential for image formation. A custom-designed high-energy parallel-hole collimator was developed to couple to the DEPICT detector, optimised for imaging ^{131}I 364.5 keV γ rays. It was designed using Geant4 based Architecture for Medicine Oriented Simulation (GAMOS) [102]. Although the Monte-Carlo optimisation study of this parallel-hole collimator was not the work of this thesis, its final design will be discussed here. Hole length and diameter, and collimator material were varied in the GAMOS Monte-Carlo simulations in order to optimise collimator design given the detectors maximum operating count rate of 160 kcps and typical ^{131}I administered activity of 3.7 – 7.4 GBq. The collimator was designed to have a low efficiency, in order to eliminate dead time issues arising from high count rates used in MRT. In the GAMOS simulations, the length of the circular collimator holes L was varied between 30 – 65 mm and the hole diameter d between 0.6 – 1.4 mm. The final parallel-hole collimator design parameters were: $L = 55$ mm, $d = 0.6$ mm and septa thickness $t = 1.4$ mm. The long collimator holes with small diameter enable high-resolution images to be acquired, whilst reducing the efficiency, and the thick septa reduced septal penetration. Tungsten and lead were both studied for the collimator material. Although both were deemed to be suitable material for the collimator, tungsten was chosen as the final collimator material due to its high density (19.25 g/cm^3 compared to 11.34 g/cm^3 for lead) and as lead is a hazardous material that is difficult to machine due to its softness. The DEPICT collimator was manufactured by M&I Materials [103] via selective laser melting (SLM), a form of additive manufacturing. The process utilises a high powered laser to fuse successive layers of tungsten powder until a complex component is built in a configuration specified by a CAD file. A case study of the collaboration between M&I Materials and the University of Liverpool is found in [104]. Applications of tungsten collimators have been proposed for high-energy ^{131}I imaging in [105, 106], with the attenuation and manufacturing accuracy of SLM tungsten discussed in [107]. Figures 5.1a and 5.1b show photographs of the collimator design. The 15.5 mm solid tungsten edge of the collimator reduces the number of γ rays interacting with the CZT detector from outside the field of view (FOV). CAD images of the top, bottom and cross sectional views of the collimator are shown in Appendix B.1.

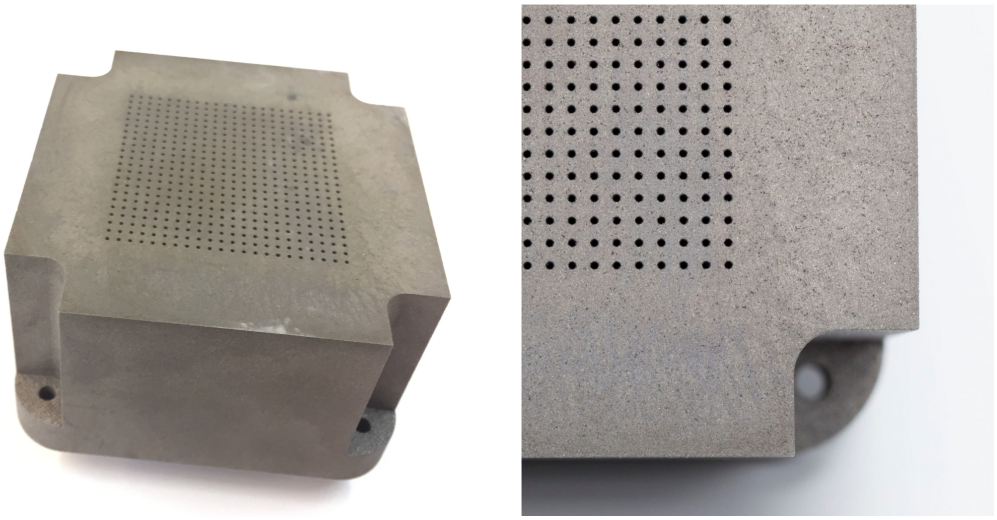

(a) (b)

Figure 5.1: Photographs of the high-energy parallel-hole DEPICT collimator.

To verify the collimated system did not suffer from dead time at therapeutic activity levels, the count rate detected in DEPICT as a function of activity was experimentally investigated in this thesis work. A 25 mm inner diameter vial was filled with ^{131}I of activities varying from 0.1 – 3.5 GBq. The count rate measured at each activity was calculated by dividing the total counts from the acquired sum spectra across all four modules of DEPICT by the acquisition time. The activities of the ^{131}I vial were measured by a dose calibrator, with an uncertainty of $\pm$ 3%. The energy threshold was set at 220 keV to reduce unwanted measurement of x-rays and low-energy γ rays that would otherwise contribute to the dead time. The results are shown in Figure 5.2. It can be seen the count rate increases linearly as a function of activity, indicating no measurable dead time. This result demonstrates the system can be used to calculate the activity uptake in localised regions up to 3.5 GBq. DEPICT therefore meets the design criteria of being able to operate at therapeutic activities, beyond the capabilities of some conventional gamma cameras, as discussed in Section 3.6.1. Unless otherwise stated, all future measurements will be acquired with the DEPICT collimator.

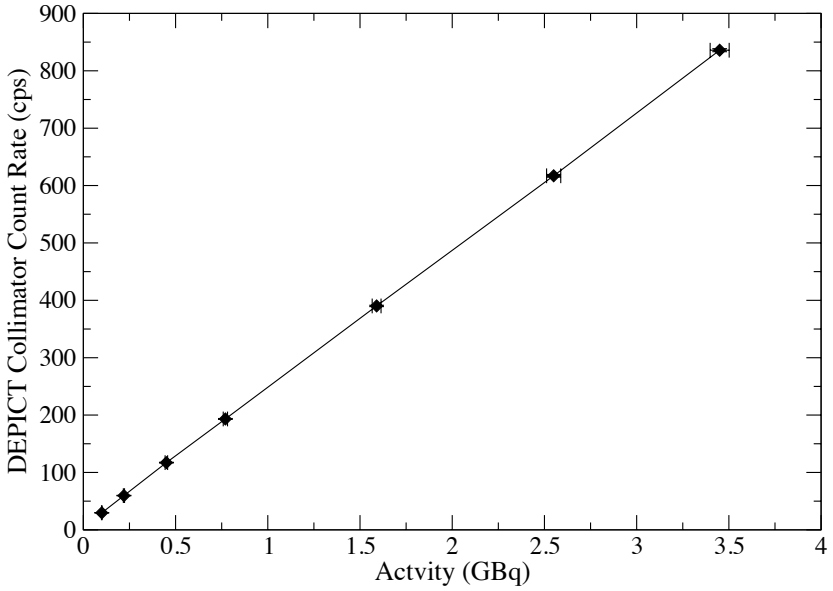

Figure 5.2: System count rate as a function of activity indicating the detector does not enter dead time up to ∼3.5 GBq with the DEPICT high-energy parallel-hole collimator.

5.2 Uniformity Phantom

It has been shown that the total count rate measured in DEPICT is directly proportional to the activity of ^{131}I, up to at least 3.5 GBq. However, localised variations in measured count rate have not yet been investigated. Knowledge and correction of any detector count rate non-uniformities are essential as these would otherwise lead to inaccurate measurements of activity within a region of interest, and hence of the absorbed dose calculated. To correct for non-uniformities, a matrix of uniformity correction factors was created. This was achieved using a flood field phantom, illustrated in Figure 5.3. A photograph of the phantom above the DEPICT detector is shown in Appendix B.3. The phantom was designed in the work of this thesis to have a fillable cavity that is 50 x 50 mm in area and 5 mm in height. The phantom was filled with 21.0 ± 0.8 MBq of ^{131}I in 12.5 ml and placed 5 cm from the detector face. Data were collected with and without the collimator for 24 hours and 300 seconds, respectively, at Thode Royal Liverpool University Hospital. The long acquisition time when the collimator is present in these measurements is required to collect sufficient statistics because the collimator is designed to operate for activities a factor of 100 higher. A matrix of detected counts per pixel was generated from the data, creating uniformity maps. It is expected that the number of γ rays incident on each pixel is equal, within statistical uncertainties accounting for the radioactive decays of $\sqrt{N}$, therefore any further variation in the number of detected counts

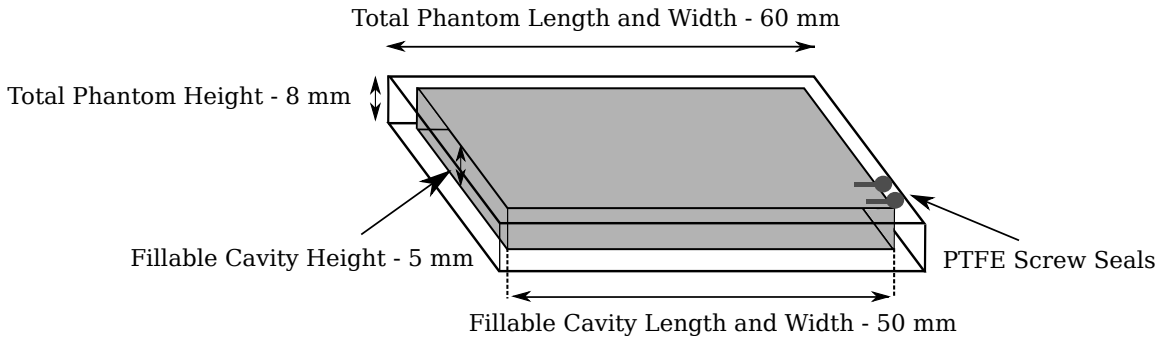

Figure 5.3: Schematic of the uniformity phantom designed to irradiate the detector for normalisation.

would be due to pixel-to-pixel variations or collimator effects. The matrix of detected counts acquired with and without the collimator were gated on γ-ray events with energies between 355 – 375 keV as all data acquired with ^{131}I will be energy gated with this window. For the uncollimated uniformity maps, the counts in each pixel were divided by the maximum pixel count of 7149. For the collimated uniformity map, the maximum pixel count was 287. This scales the uniformity maps for the uncollimated and collimated data between 0 and 1, as shown in Figures 5.4b and 5.4b respectively, to give appropriate uniformity factors for each pixel. For the uncollimated data in Figure 5.4a, it can be seen there is variation in detected photopeak counts across the system. There are reduced counts in pixels at the edges of each of the four detector modules. This is due to γ rays passing through the physical gaps between the detector modules and therefore not interacting within the pixels and can also be attributed to degraded charge collection in edge pixels [97]. In addition, environmental effects such as light can also degrade the performance of edge pixels. There is also a region of reduced counts corresponding to $\sim$0.7 normalised counts in detector module 2 from pixel (12, 8) to (16,12). This is due to that detector module being slightly misaligned with respect to the other three modules, increasing the gap. This misalignment is shown in Appendix B.2.

It is particularly important to uniformity correct the data when using the collimator as the reduction in counts due to module misalignment is exacerbated, as seen in Figure 5.4b. This is due to the collimator holes no longer exactly aligning with the CZT pixels. Figure 5.5 shows a histogram of the pixel counts from the data in Figure 5.4b. Ideally, the histogram would be normally distributed around the mean number of counts in the pixels, however the plot shows tailing on the lower count side, highlighting that a number of pixels have reduced counts, beyond those expected from statistical fluctuations. Uniformity correction of future

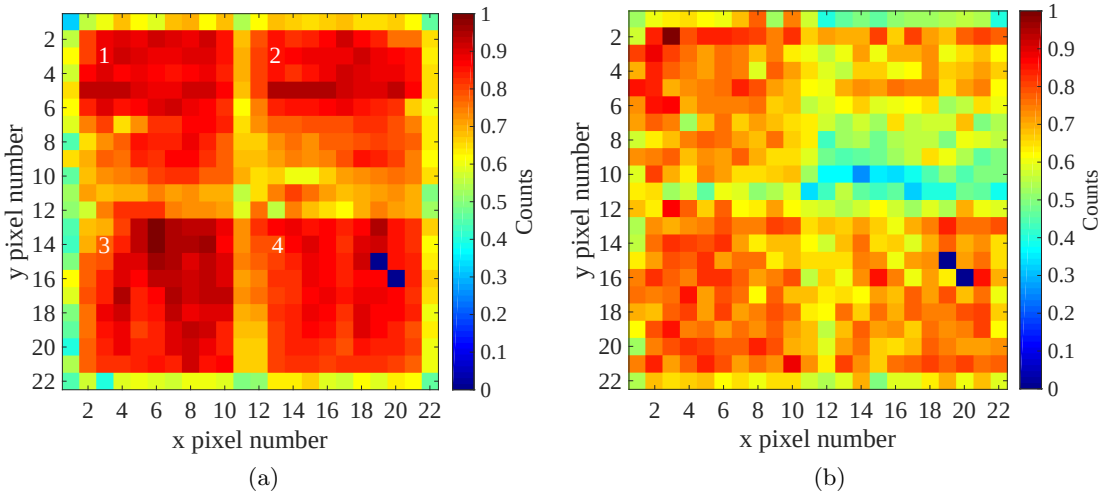

Figure 5.4: Uniformity factor pixel maps for the DEPICT detector (a) without and (b) with the collimator coupled to the detector.

data sets will involved dividing each pixel by its associated pixel uniformity factor. In pixels where its uniformity factor is nearly or equal to 1, such as in the middle of the detector modules, the counts will not be modified to a great extent. However, module edge pixels with a low uniformity factor will have their counts increased to bring them in line with inner module pixels.

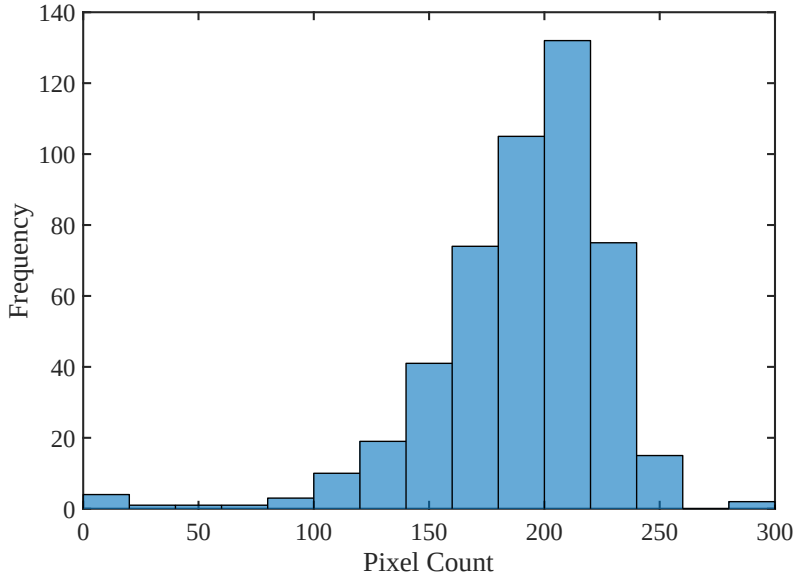

Figure 5.5: Histogram of counts acquired when the collimated system is uniformly irradiated and events are gated on energy between 355 – 375 keV. There are increased low pixel counts because of collimator-module misalignment.

5.3 Line Phantom

Line phantoms were used to investigate the DEPICT system spatial resolution with and without scatter material between the phantom and the collimated detector [108]. The data for these measurements were acquired at The Royal Liverpool University Hospital. The system spatial resolution measures the ability of the system to determine the origin of a γ ray on an x-y plane and is therefore a widely used measure of image quality. It is important to take account of the Compton scattering contribution as the γ rays will have to travel through the neck of the patient in thyroid MRT before they can be detected externally. The system spatial resolution of the Siemens Intevo gamma camera used to acquire data in this chapter is 13.4 mm with its associated high-energy parallel-hole collimator, measured at a source-to-collimator distance of 10 cm. Thus, clinical systems such as this can only be used to determine the 3D spatial distribution of activity in volumes that are large relative to this dimension. For the calculation of system spatial resolution for DEPICT, the test equipment consisted of two line phantoms (capillary tubes) with an inner diameter of 1 mm placed 1.6 cm apart. The capillary tubes were $\sim$40 mm in length, filled with 30 MBq of ^{131}I and sealed at both ends. The liquid radionuclide filled approximately 30 mm of the capillary tubes. The tubes were positioned 10 cm from the face of the collimator along the axis of measurement in both x- and y-directions. No material was placed between the collimator face and the capillary tubes for the first acquisition. Figure 5.6a shows a photograph of the capillary tubes with respect to one another. Before data acquisition, the capillary tube labelled (1) was repositioned so the liquid ^{131}I was in line with that of tube (2). The system spatial resolution is then obtained from a line spread function. A line spread function (LSF) is the profile of measured counts as a function of position across a line source. To create the LSF, the data in the pixel intensity maps were summed parallel to the direction of the capillary tubes over widths of 22 mm (pixels 6 to 16 in both x- and y-directions) to get a value for each point in the LSF over 11 pixels. This is illustrated for the x-direction in Figure 5.6b. Calculating the average count over 11 pixels and using two capillary tubes allowed data from pixels in all four detector modules to be included in each LSF, giving a spatial resolution that is representative of the whole detector. The pixel intensity maps were uniformity corrected using the uniformity factors in Figure 5.4b. Due to the logistics of acquiring data at a working hospital, the data collection times of the four data sets (capillary tubes placed in x- and

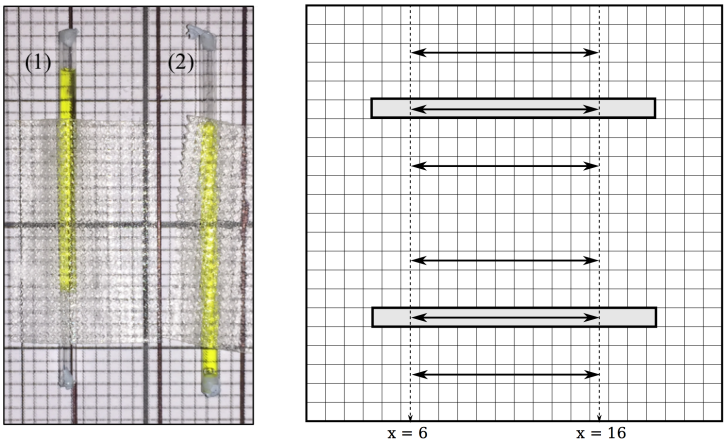

(a) (b)

Figure 5.6: (a) Photograph of the 1 mm inner diameter capillary tubes used to measure the system spatial resolution in y-position and (b) a schematic illustrating how the data were summed to form line spread functions for capillary tubes in the x-position where the black arrows show the range of pixels summed. In reality, all counts in pixels from x = 6 to x =16 were summed for a given y-pixel, but for ease of understanding only 6 arrows are shown.

y-positions, with and without scattering material) were not comparable. The range of data acquisition times was 21 – 24 hours. Therefore, the counts in each image were normalised when producing the LSFs for accurate comparison.

Figures 5.7a and 5.7c show the pixel intensity maps produced with the capillary tubes placed in x- and y-positions, respectively. The pixel maps are gated on γ rays with energy between 355 – 375 keV. Figure 5.7a shows two areas of high counts that are one pixel in width in the y-direction and approximately 15 pixels in length in the x-direction. The capillary tube placed at y = 15 appears to contain more activity than the tube at y = 7, as each pixel contains ∼4000 counts, compared to ∼3000 counts indicating the two capillary tubes may not contain equal activities. Figure 5.7c shows the same two areas of uptake of 1 pixel wide and 15 pixels in length. The capillary tube with slightly reduced activity is now positioned at x = 16. For this capillary tube, pixels y = 4 to y = 11 have reduced counts compared to those from y = 12 to y = 18. The top half of this capillary tube is positioned over module 2 where there are known to be reduced counts, seen in Figure 5.4b. Although the data has been uniformity corrected, Figure 5.7c shows the uniformity correction has not adequately correctly the counts within this module. The uniformity map would be improved with increased statistics as currently the average pixel count is approximately 200, giving a low value of 0.002 cps per pixel.

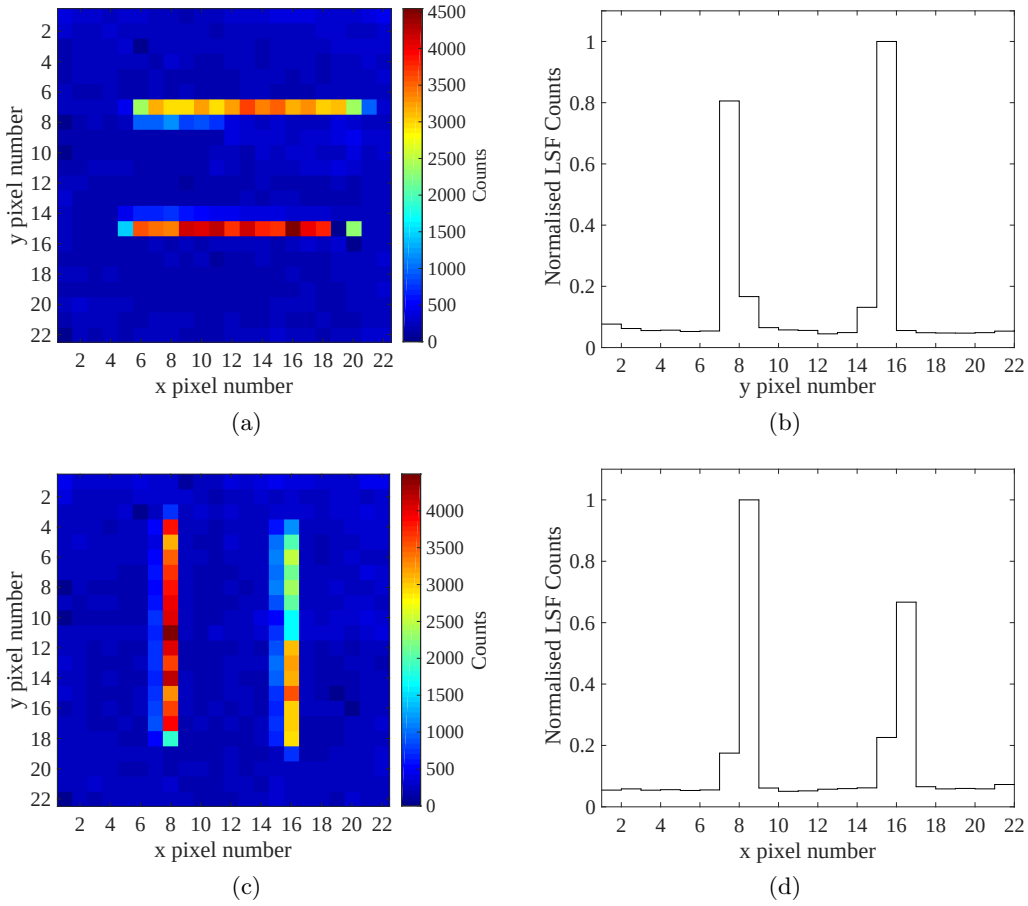

Figure 5.7: (a) Capillary tubes with no scatter material in x-position and (b) summed LSF for data shown in (a). (c) Capillary tubes with no scatter material in y-position and (d) summed LSF for data shown in (c).

System spatial resolution is typically measured and expressed as the FWHM of the LSF, with the FWHM equal to the minimum separation required by two line sources if they are to be just resolved. As the DEPICT detector is pixelated, the LSF counts are histogrammed into well defined bins. Therefore, it is not appropriate to calculate the FWHM of the LSF using a standard Gaussian fit. For calculation of the DEPICT system spatial resolution, the percentage of counts in the peak pixel bin were compared to those of its two nearest neighbours to assess the spread of counts from imaging a 1 mm inner diameter capillary tube. Firstly, the average normalised background counts were determined and subtracted from all pixel bins. The normalised background count for the x-position data was 0.055, and 0.058 for the y-position data. Then, comparison of the background subtracted counts in the LSF peak pixel bin with those in the pixel bins either side of the peak bin was performed. Table

5.2 shows the peak bin pixel number, the two nearest neighbour pixel bin numbers and the background subtracted relative counts (%) in each bin with respect to the summed counts of the three bins.

Capillary tubes in x-position			
y pixel number	%	y pixel number	%
Pixel 6	0	Pixel 14	7.48
Pixel 7	87.14	Pixel 15	92.45
Pixel 8	12.95	Pixel 16	0.07
Capillary tubes in y-position			
x pixel number	%	x pixel number	%
Pixel 7	10.99	Pixel 15	21.40
Pixel 8	88.73	Pixel 16	77.68
Pixel 9	0.28	Pixel 17	0.92

Table 5.2: Comparison of counts within the peak pixel bin to two nearest neighbour bins for the two capillary tubes in both x- and y-positions. The % value shows the ratio of the counts within that pixel bin to the sum of the three pixel bins, following background subtraction.

Table 5.2 shows that for the two capillary tubes in the x-direction and two in the y-direction, the majority of the counts fall within one pixel with a much smaller percentage of counts in the pixel bins either side of the peak bin. For the x-position, 87% and 92% of the counts for both capillary tubes lie within one pixel. For the y-position, the values are 89% and 78%. The ratio of peak bin counts to the sum of the peak and nearest neighbours counts is likely poorer for the capillary tube at x = 16 due to the uniformity correction not adequately recovering lost counts. Given that the majority of the counts lie within one pixel width, the system spatial resolution of DEPICT at 10 cm was concluded to be 2 mm. Discrete detectors such as the DEPICT CZT detector have their spatial resolution governed by the size of the pixel elements. Therefore, although the size of the object being imaged is less than 2 mm, this is not discernible as the minimum bin size in the pixel size. It is possible to manufacture CZT detectors with smaller pixel size but this adds complexity and cost in the readout and processing of the data due to the increased number of pixels and sharing of charge across multiple pixels.

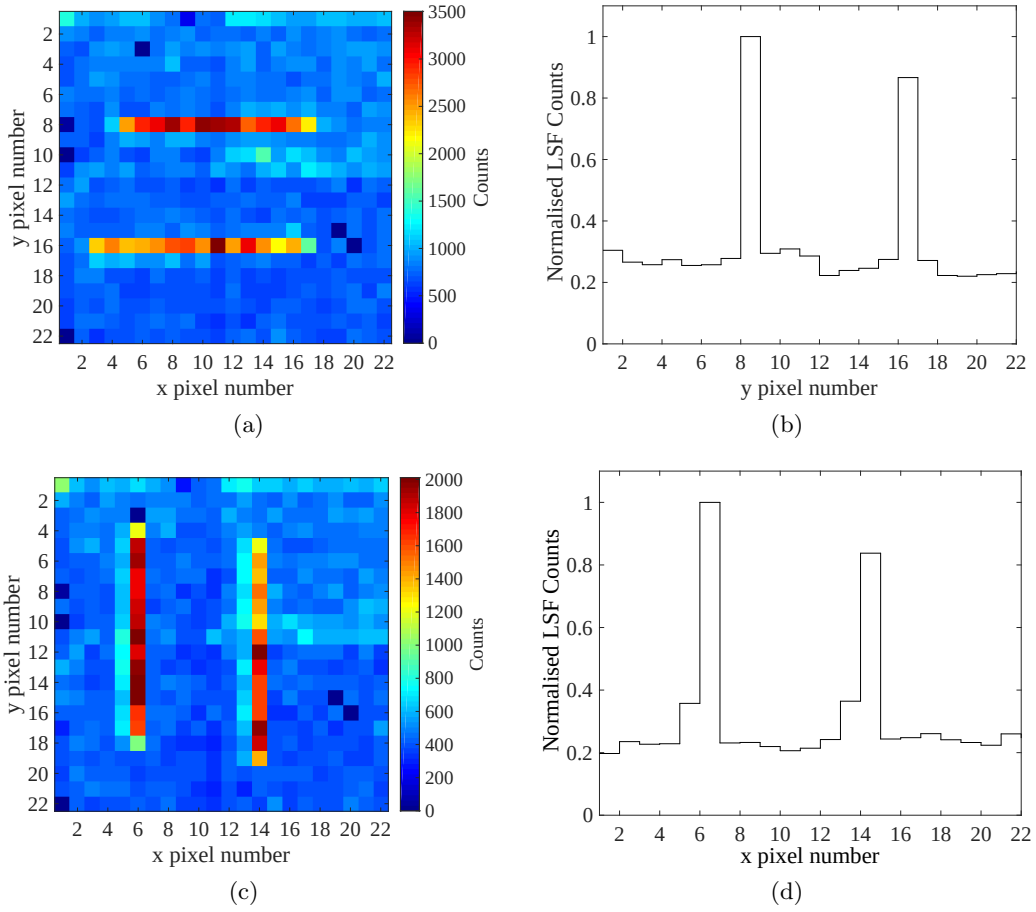

Figure 5.8: (a) Capillary tubes with scatter material in x-position and (b) summed LSF for data shown in (a). (c) Capillary tubes with scatter material in y-position and (d) summed LSF for data shown in (c).

To evaluate the spatial resolution in a more realistic context to clinical implementation, a 10 cm thick acrylic scattering block ($Z_{\text{eff}} = 6.47$ [109]) was placed between the capillary tubes and the collimator [108]. A photograph of the setup is shown in Appendix B.5. This is to replicate the scattering effect when the radioactive source is in the body of a patient. With an effective atomic number Z_{eff} for soft tissue of 7.4, Figure 3.2 shows Compton scattering is the dominant interaction in tissue for the γ rays emitted from ^{131}I and will therefore contribute significantly. Figures 5.8a and 5.8c show the pixel intensity maps produced with the capillary tubes placed in x and y-positions with 10 cm of scatter material. It can be seen in Figures 5.8a and 5.8c that, as expected, there is significantly increased background in comparison to the data acquired with no scattering material. There are however, still two areas of increased counts of 1 pixel width corresponding to the two capillary tubes in each image. Figures 5.8b

Capillary tubes in x-position			
x pixel number	%	x pixel number	%
Pixel 7	3.07	Pixel 15	3.44
Pixel 8	91.82	Pixel 16	93.87
Pixel 9	5.11	Pixel 17	2.81
Capillary tubes in y-position			
y pixel number	%	y pixel number	%
Pixel 6	14.02	Pixel 14	17.66
Pixel 7	86.08	Pixel 15	80.81
Pixel 8	0	Pixel 16	1.52

Table 5.3: Comparison of counts within peak pixel bin to two nearest neighbour bins with scatter material present. The % value shows the ratio of the counts within that pixel bin to the sum of the three pixel bins, following background subtraction.

and 5.8d show the LSFs calculated for the summed data acquired with the capillary tubes in x- and y-positions with scatter material. The normalised average background counts are 0.25 and 0.25, respectively, for the x- and y-position data. Following background subtraction, the ratio of peak pixel bin counts and nearest neighbour counts to the sum of peak and nearest neighbour counts for each LSF were calculated and are shown in Table 5.3.

The percentage of counts within the peak bins compared to the sum of the peak and nearest neighbour bins are all over 80%, shown in Table 5.3. Although the number of background counts has increased, the spatial resolution has not degraded with the inclusion of scattering material. In clinical gamma camera systems, the FWHM is known to degrade with the inclusion of scattering material, however very little difference is observed in DEPICT. It is expected that this is because the DEPICT collimator offers such high resolution that any differences are at a negligible level, at the scale of one pixel width. The system spatial resolution is equal to the minimum distance that two line phantoms must be separated by in space to appear as separate objects in the image. With DEPICT, as long as two objects are greater than 2 mm (1 pixel width) apart, they will be distinguishable from one another.

A useful measure of the relative number of γ rays being detected via the photoelectric interaction is the peak-to-total ratio, defined as the ratio of number of counts in the photopeak

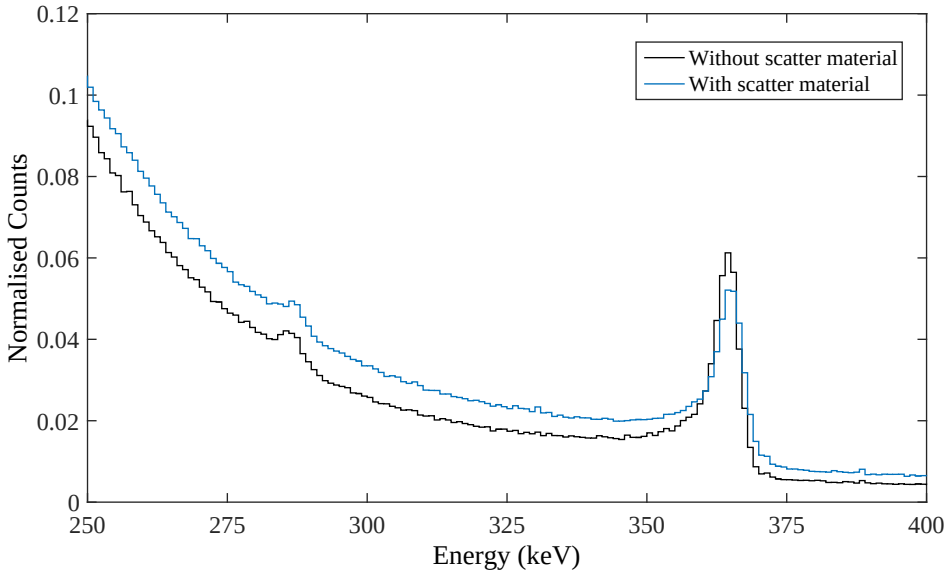

Figure 5.9: Summed energy spectra for capillary tubes in x-position with scatter (blue line) and without scatter (black line) material.

to the total number of counts in the spectrum. The peak-to-total ratio was calculated from the sum spectra acquired with the capillary tubes in the x-position and compared for the data collected with and without scatter material between the detector and the sources. The total normalised counts between 250 – 400 keV, the energy region shown in Figure 5.9, were calculated and compared to the the photopeak counts, with energy between 355 – 375 keV. For the data acquired without scatter material, the peak-to-total was calculated as 14.7%. For the scatter data, the peak-to-total decreased to 12.5%. As expected, the peak-to-total has therefore slightly degraded due to the inclusion of scattering material. Having a lower peak-to-total ratio is undesirable as it is indicative of increased scattering contribution, which degrades the contrast in an image, however the excellent energy resolution of DEPICT system in comparison to NaI scintillation based systems will facilitate high quality vetoing of scattered events. The DEPICT system spatial resolution of 2 mm at 10 cm is significantly better compared to clinical gamma cameras with a resolution of 13.4 mm. Improvement in spatial resolution reduces partial volume effects, improves the detectability of small structures and provides precise anatomical localisation of radiotracer uptake, leading to improved dose estimates.

5.4 Jaszczak Phantom

The Jaszczak phantom [110] is a perspex body that contains various inserts for vials of differing size. It is routinely used to assess the imaging performance of gamma cameras, including image contrast and spatial resolution. Perspex is known as a tissue equivalent material as it has a linear attenuation coefficient at 364.5 keV of 1.26 cm^{-1} and is comparable that of soft tissue (1.09 cm^{-1} at 364.5 keV) [54]. One such phantom was constructed at the University of Liverpool for the DEPICT project and is shown photographed in Figure 5.10a. It can be seen that there are 12 inserts; 3 of which are 10 mm in diameter, 3 are 11 mm, 3 are 12.4 mm and 3 are 16.4 mm. Three vials of length 50 mm and inner diameter 10 mm were filled with aqueous ^{131}I and placed into the Jaszczak phantom. The positions of the vials, labelled as 1, 2 and 3 in Figure 5.10a, corresponding to central positions above pixel numbers (11, 8), (6, 17) and (16, 17) and the phantom was placed 10 cm from the detector, as shown in Figure 5.10b. Vials 1, 2 and 3 contained solutions of activity 1.142 ± 0.03 GBq, 1.042 ± 0.03 GBq and 1.189 ± 0.04 GBq, respectively, as measured using a dose calibrator with an error of 3%. Data were collected for 600 seconds. Figure 5.11 shows the sum energy spectrum acquired from imaging the three vials for 600 seconds using DEPICT. The dashed black lines illustrate the energy window that is used to select imaging events of 355 – 375 keV. Figure 5.12a shows the energy gated pixel map acquired. A uniformity correction was then applied to the data and the uniformity corrected vial data are shown in Figure 5.12b.

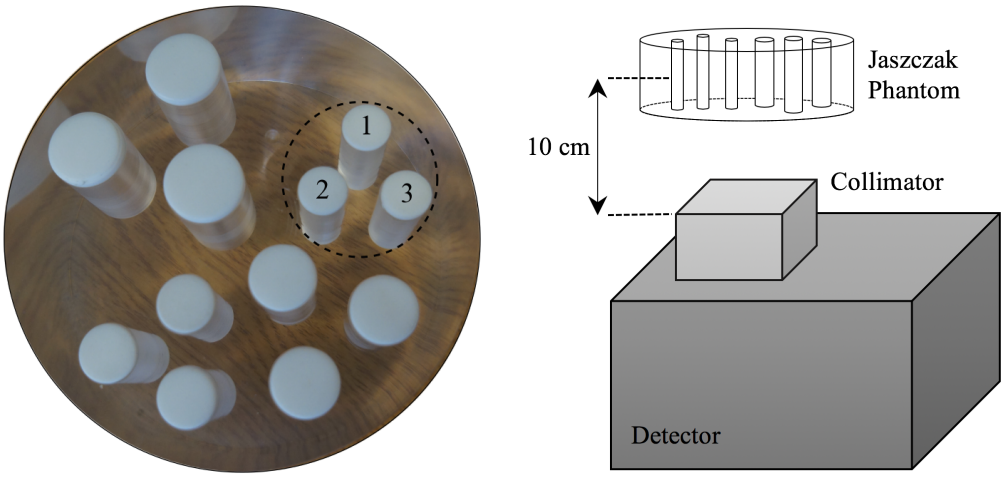

(a) (b)

Figure 5.10: (a) Photograph of the custom Jaszczak phantom with the three 10 mm inner diameter vials highlighted and (b) schematic of the Jaszczak phantom orientation above the collimated detector.

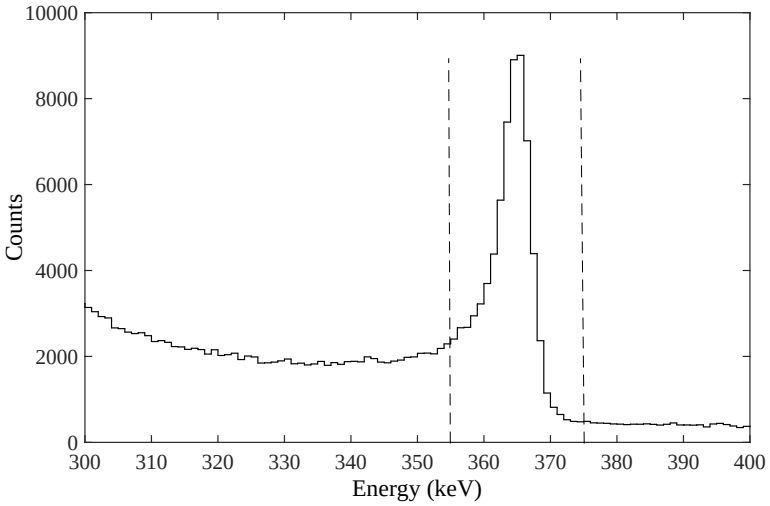

Figure 5.11: Energy spectrum summed for all pixels produced for data acquired with three ^{131}I vials. The dashed black lines show energy gate that is applied to Figures 5.12a and 5.12b.

The uniformity corrected, energy gated pixel map produced with the DEPICT system shown in Figure 5.12b is a direct projection of the three vials with three distinct areas of higher counts with respect to the background. The positions of the three vials have been accurately reconstructed. Vial 2 is known to have slightly reduced activity with respect to the other two vials. The total counts from the pixels at the known position of vial 2 are 2.23 x 10^4. The counts for vials 1 and 3 were 2.64 x 10^4 and 2.68 x 10^4, respectively, demonstrating that the counts reflect the activity differences between the vials.

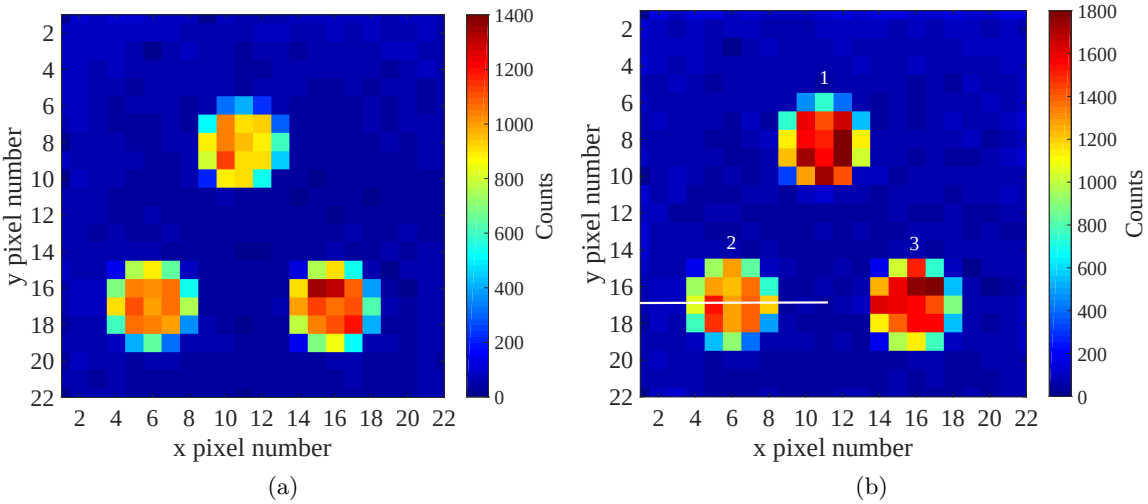

Figure 5.12: (a) Energy gated pixel map acquired with DEPICT from imaging three 10 mm inner diameter vials of ^{131}I and (b) uniformity corrected, energy gated pixel map acquired from imaging three 10 mm inner diameter vials of ^{131}I. The white line highlights the slice taken for Figure 5.15.

Data were subsequently acquired with the three vials of ^{131}I and a commercial gamma camera for comparison. The Siemens gamma camera was coupled to a high-energy general purpose (HEGP) collimator with hexagonal holes of $L = 59.7$ mm, $d = 4.0$ mm and $t = 2.0$ mm. The energy window was set between 337 – 392 (15%) as this is typically the energy window set in clinical imaging. The data acquired with the clinical gamma camera were in Digital Imaging and Communications in Medicine (DICOM) format, which is the international standard to transmit, store, retrieve, process and display clinical medical imaging information [111]. Examples of information that can be read out from DICOM files is shown in Appendix B.4. The medical imaging software OsiriX [112] was used to analyse the DICOM files. The gamma camera had a FOV of 614 mm^2, a matrix size n of 512 x 512 and zoom factor Z of 2. A zoom factor is sometimes applied during acquisition to further decrease pixel size. The size of a pixel d in mm was therefore calculated to be 0.6 mm, using Equation 5.1 [113].

$$d = \frac{FOV}{Z \times n} \tag{5.1}$$

The centre of the vials were positioned 10 cm from the HEGP collimator for 600 seconds. The image obtained with the gamma camera is shown in Figure 5.13. Although the data were originally binned into a 512 x 512 matrix, the axis was scaled given the 0.6 mm size and is therefore shown as a function of pixel size in mm.

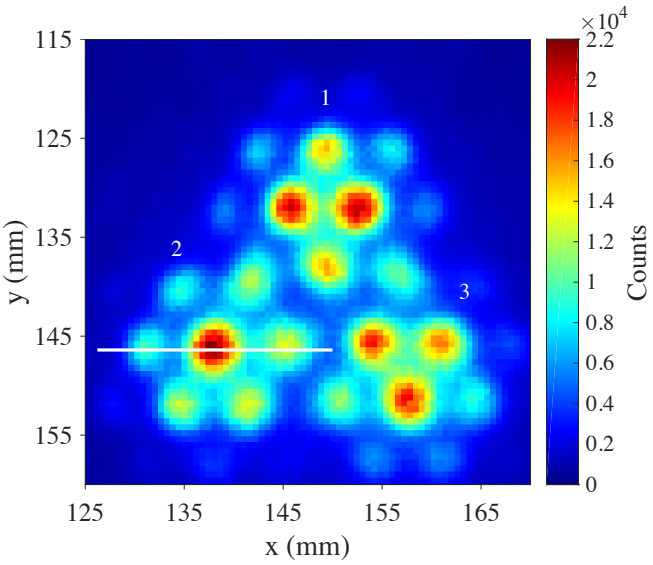

Figure 5.13: Pixel map acquired from imaging three 10 mm inner diameter vials of ^{131}I with a Siemens Intevo gamma camera. The white line highlights the slice taken for Figure 5.15.

The image acquired with clinical gamma camera does not have three distinct higher count rate areas corresponding to the vial cross-sections, as is seen in the DEPICT image, but instead shows multiple circular patterns. Imaging of high-energy γ rays requires collimators to have thicker septa and larger holes, however this causes hole-pattern artefacts within the image [114, 115]. The diameter of one of the small circles was measured using OsiriX to be approximately 4.2 mm in size, which is consistent with the size of the 4 mm Siemens collimator holes. If a γ ray penetrates the collimator septa without first undergoing a scatter interaction, it cannot be distinguished from a desired event that passes straight through a collimator hole. This cannot be compensated for using techniques that are based on differences in energy spectra and degrades the spatial resolution. Often, collimators used with clinical gamma camera have hexagonal holes. This shape is desirable as many holes can be packed together, increasing the sensitivity. However, the system suffers from septal penetration if the septa are not sufficiently thick for the γ rays that are being imaged, illustrated by the black solid lines in Figure 5.14a. This produces an effect in the acquired image that is know as a 'star artefact' due to the effect producing an image that looks like a star, resulting in a loss of image contrast. This effect is exacerbated when there is a high-energy radionuclide within a small volume and is regularly seen in ^{131}I images of the thyroid, increasing the difficulty of performing area delineation. This star artefact can be seen in Figure 5.14b. This image shows the data from Figure 5.13 with a lower maximum value set in the colour map.

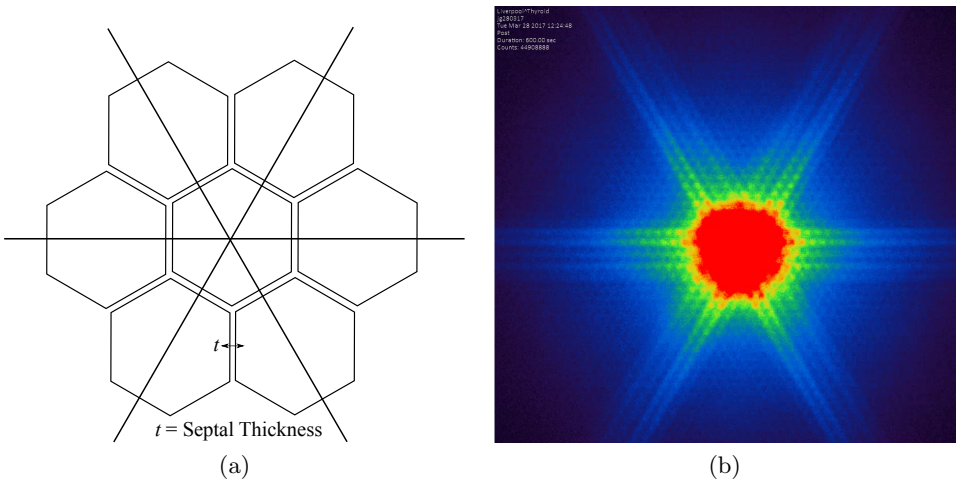

(a) (b)

Figure 5.14: (a) Schematic illustrating the star artefact caused by septal penetration of γ rays through the collimator septa. (b) Jaszczak phantom image acquired with a clinical gamma camera and ^{131}I showing star artefact.

Improving area delineation in planar gamma camera imaging, and subsequently volume delineation in SPECT images, is an important aim of the DEPICT project. This allows for better identification of the spatial distribution of ^{131}I uptake to diseased areas of the thyroid, and subsequently extraction of dosimetric values. In order to determine if accurate area delineation is possible with the DEPICT system, analysis was performed to ascertain if the size of a vial from the image in Figure 5.12b could be quantified. This methodology was repeated and compared with the gamma camera image from Figure 5.13. To analyse these data sets, a slice was taken through the centre of one of the vials. The ideal slice would have no counts outside the known vial position, with a step function of maximum normalised counts of 1 within the vial location. The width of the step function should correspond to the known diameter of the vial. The white lines through vial 2 in Figure 5.12b and Figure 5.13 illustrate the chosen slice, corresponding to y = 17 pixels in the DEPICT data and y = 146 mm in the Siemens gamma camera data. The slices were both 22 mm in length in the x-direction. Figure 5.15 shows the slices produced from the images with the maximum counts from both the DEPICT and Siemens gamma camera images normalised to 1 and plotted as a function of x position (mm). The DEPICT pixel numbers were multiplied by 2, given the pixel size of 2 mm, to calibrate into mm for direct comparison with the Siemens data. The blue dashed line shows the Siemens gamma camera data and the black solid line shows the DEPICT data. The red dashed lines indicate the known position of the vial from the DEPICT image, between x = 7 and x = 17 mm.

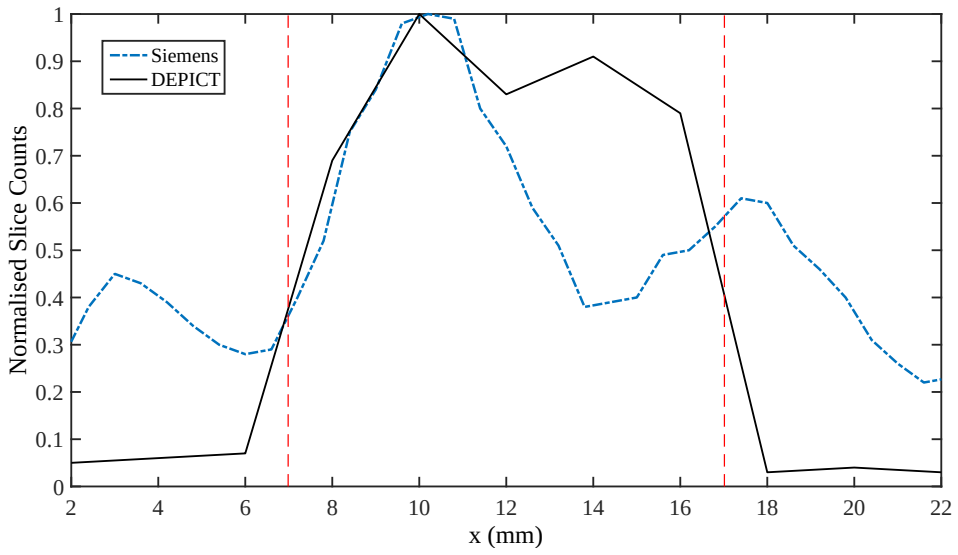

Figure 5.15: Slice through vial 2 from DEPICT (black solid line) and Siemens gamma camera data (blue dashed line). The dashed red lines show the true diameter of the vial.

The DEPICT slice begins at background level increasing to a maximum between the red dashed lines, before falling back to background. The background intensity of the DEPICT data is ∼5% of the maximum. The variation in the DEPICT slice counts within the known vial position can be attributed to pixel-to-pixel fluctuations due to Poisson statistics. The gamma camera data however, has 3 local maxima which are centred at approximately x = 3, 10 and 18 mm. It is clear from visual inspection that the counts for the Siemens data are not well constrained within the known region of the vial. There is also increased background of 30% of the maximum signal amplitude. The DEPICT system therefore clearly offers enhanced spatial resolution and signal-to-noise over the Siemens system, which cannot delineate the vial region. False hot spots in the Siemens data would correspond to inaccurate regions of localised activity in a medical image, which could lead to incorrect diagnosis or false verification of treatment.

In order to quantify how the DEPICT data varies from being an ideal step function, the data was plotted against a step function of width 10 mm in Figure 5.16. The red dashed line shows the diameter of the vial represented by an ideal step function, the solid black line shows the DEPICT slice data and the grey dashed line through 0.5 normalised slice counts shows the FWHM of the step function. This FWHM line was found to intercept the DEPICT data at x = 7.4 and 16.8 mm. If the data were a true step function, it would intercept x = 7 and 17. The deviations from x = 7 and 17 are within one pixel width. This is a satisfactory deviation as the limitation of the DEPICT system is the 2 mm pixel size.

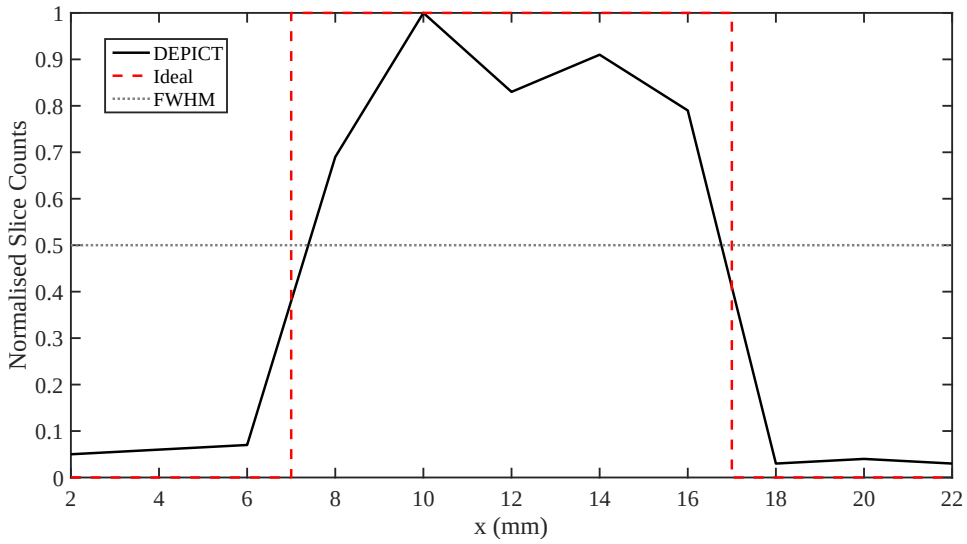

Figure 5.16: Slice through vial 2 from DEPICT data. Red dashed line shows the ideal step function.

Taking a slice through a region of interest in an image is useful for looking at the signal-to-noise ratio and for an approximate calculation of the vial size, but statistical fluctuations in the pixel count may mean this is not a good way to determine the size of features. Therefore, the cumulative frequency of the slices has been calculated. The cumulative frequency distribution gives a running total of the counts in each pixel along the slice, therefore reducing the statistical variation with each summed pixel count. The cumulative frequency distributions of the slices through the middle of vial 2 from Figures 5.12b and 5.13 have been plotted as a function of pixel size in mm. These are shown in Figure 5.17. The dashed black lines show the apparent diameter of the vial from the pixel map images.

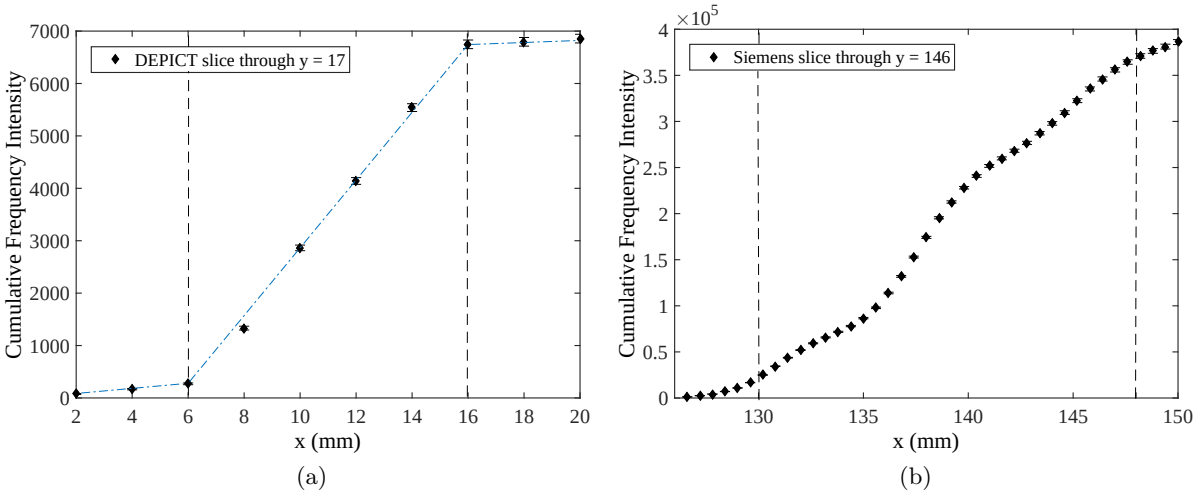

Figure 5.17: Cumulative frequency plots for (a) the DEPICT system and (b) the clinical Siemens Intevo gamma camera. The black dashed lines show the apparent diameter of the vial from each image.

In Figure 5.17a, there are three distinct regions of the cumulative frequency plot that can be fit with three straight lines of differing gradient, shown by the blue dashed lines. A straight line was plotted through 2 – 6 mm with a gradient of 97 counts/mm. This increased to 1323 counts/mm between 6 – 16 and reduces to 55 counts/mm between 16 – 20 mm. The gradient of the lines corresponding to areas of background in Figure 5.17a (2 – 6 mm and 16 – 20 mm) are less than 7.5% of gradient through the vial region (6 to 16 mm). The gradient is expected to be low in regions of background, as not many counts are being accumulated. In the vial, lots of counts are accumulating so the cumulative frequency increases rapidly and uniformly if the activity is homogeneous. The point at which the gradient first deviates from background, indicated by the first dashed line at 6 mm in Figure 5.17a, is taken as

the start of the vial. The end of the vial is found when the gradient of the line deviates back to background, shown by the second dashed black line at 16 mm. The width of the lines is 10 mm, which is consistent with the known size of the vials. Comparatively, in the cumulative frequency plot shown in Figure 5.17b, acquired from the gamma camera data in Figure 5.13, there are no clear increase or decreases in gradient. Between 136 – 140, there is a small bump, corresponding to the hot spot seen in the middle of the slice, but the gradient remains relatively steady. It therefore is not practical to apply straight line fits to this data. From Figure 5.13, the start and end point of the vial appear to be between 130 – 148 mm which is indicated by the dashed lines in Figure 5.17b. This corresponds to a vial diameter of 18 mm, which is larger than the known vial diameter of 10 mm due to septal penetration and poor spatial resolution. As the vial shape is not well defined, it is difficult from the image to ascertain the shape and diameter of the vial. If this were an organ and dosimetry were being performed by multiple operators, it is likely a variety of organ sizes would be measured giving a range of calculated absorbed doses. The DEPICT system with improved spatial resolution, energy resolution and custom-designed collimator successfully facilitates area delineation and will reduce inter-operator variability in dose measurements when performing dosimetry.

5.5 Thyroid Phantom

To evaluate the system performance for imaging the uptake of radioiodine in the case of thyroid disease, a perspex anthropomorphic thyroid phantom based on a clinical Picker phantom [116] was developed, shown in the photographs in Figures 5.18a and 5.18b. This is a very important test case as ultimately the aim of the DEPICT project is to be able to perform quantitative dosimetry for radioiodine treatment. The phantom has a thyroid shaped cavity with 2 lobes and dimensions of 75 x 65 x 17.5 mm. In the human body, a healthy thyroid gland would show similar uptake of radioiodine in both lobes. However, in patients with thyroid cancer or benign disease, there will be variable uptake in the thyroid resulting in areas of higher or lower uptake with respect to the rest of the volume. These areas are referred to as ‘hot’ and ‘cold’ regions, respectively. Hot spots are not often cancerous, however between 5 – 15 % of cold nodules may become malignant [117]. This expected non-uniform uptake has been taken into account when designing the phantom. The phantom was designed to have 3 solid rods in the thyroid cavity with diameters of 6, 9 and 12 mm to mimic three cold spots. The height of the solid rods were equal to the lobe thickness. The right lobe also

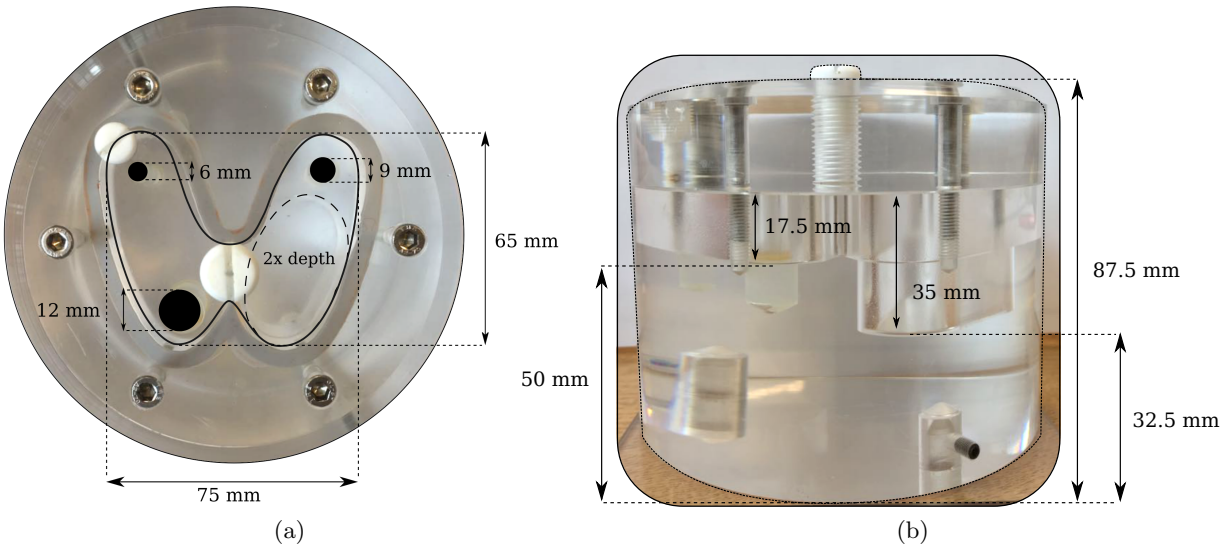

Figure 5.18: Custom thyroid phantom (a) top and (b) side views.

contained a section that was twice the depth of the rest of the cavity and therefore contained twice the activity, mimicking a hot spot. The hot spot had a depth of 35 mm. Between the normal lobe and the base of the phantom is a 50 mm section of perspex (32.5 mm below the hot spot). This attenuating material replicates the attenuating properties of the human body. The thyroid phantom was filled with 2.7 GBq ^{131}I and imaged at a distance of 10 cm from the DEPICT collimator. In a clinical setting, the gamma camera FOV would be larger than that of the thyroid being imaged. However, the DEPICT CZT detector is a prototype system, which has a FOV limited to 44 mm^2 (22 x 22 pixels). The active region of the thyroid phantom is 75 x 65 mm and therefore larger than the detector FOV. Consequently, data were acquired with DEPICT at four x,y positions in a 2 x 2 grid for 600 seconds each, as shown in Figure 5.19. The pixel maps produced at each position were normalised with respect to the uniformity map shown in Figure 5.4b and aligned with one another, obtaining an image of the total thyroid active area. The final image is shown in Figure 5.20a. This multiple data collection and merging of the data sets would not be required with a final clinical DEPICT detector as it would be designed with a larger FOV by tiling multiple CZT modules. For comparison, an image of the thyroid phantom was also acquired for 600 seconds with the clinical gamma camera and is shown in Figure 5.20b.

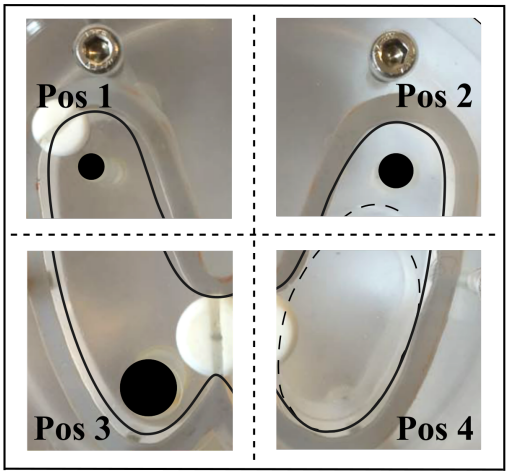

Figure 5.19: Schematic showing the four x,y positions of the thyroid phantom. The pixel maps acquired at each position with the DEPICT system were normalised and merged together to create one image of the total thyroid active area.

Qualitatively, the DEPICT image demonstrates significantly improved image quality compared to the gamma camera image. The three cold spots are evident in the DEPICT image with three regions at the known cold spot positions with approximately background counts (∼30 counts). The 6 and 9 mm diameter cold spots are not evident in the Siemens gamma camera image and although there is a slightly reduced region of counts at the known position of the 12 mm cold spot, it is not well defined. Overall, there are increased statistics in the Siemens image because of the large collimator hole size compared to the DEPICT collimator, increasing sensitivity. As a reminder, this high sensitivity is undesirable in dosimetric imaging following MRT, because it leads to high dead time in the detector system, which induces large uncertainties on dosimetric calculations.

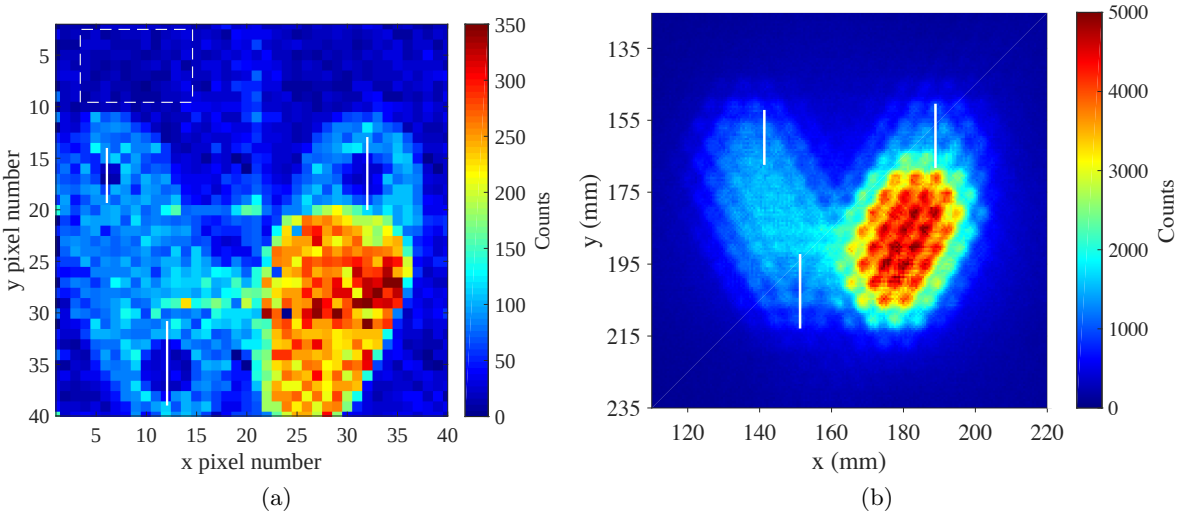

Figure 5.20: Thyroid phantom imaged with (a) DEPICT CZT detector and high-energy parallel-hole collimator and (b) Siemens gamma camera with high-energy general purpose collimator. The white lines in (a) and (b) correspond to the slices used in Figure 5.21. The dashed square in (a) highlight the subset of pixels used to acquire background counts for Figure 5.21.

To quantitatively analyse the cold spots, slices were taken through the 6, 9 and 12 mm cold spot locations in the y-direction, shown by the white lines in Figures 5.20a and 5.20b. The maximum counts of the three slices for both the DEPICT data and the Siemens gamma camera data were normalised to 1 and plotted as a function of mm in the y-direction, shown in Figure 5.21. The red dashed lines show the known location and width of each cold spot. The black solid line shows the DEPICT data and the blue dashed lines show the Siemens data, for each of the 6, 9 and 12 mm cold spots. Ideally, the slices would show normalised counts of 1 outside the known cold spot region, with a reduction to background levels within the region. For the 6, 9 and 12 mm cold spots, the DEPICT data follows this trend with a reduction in counts within the known cold spot region. The data plotted through all three cold spots begins at a maximum, decreases rapidly within the cold spot location and increases again. The DEPICT 9 mm data looks slightly less like a step function because the diameter of the cold spot is not divisible by the 2 mm pixel size, therefore it will cover 5 pixels. This is due to the partial volume effect described in Section 3.6 where objects smaller than the system resolution (2 mm for DEPICT) will have all their counts detected, but over a larger volume than their true size. The slices through the cold spots in the Siemens data have a very irregular pattern, caused by the hole-pattern artefacts within the image due to the large collimator holes. The 6 mm Siemens data generally increase over 12 mm. The 9 mm data

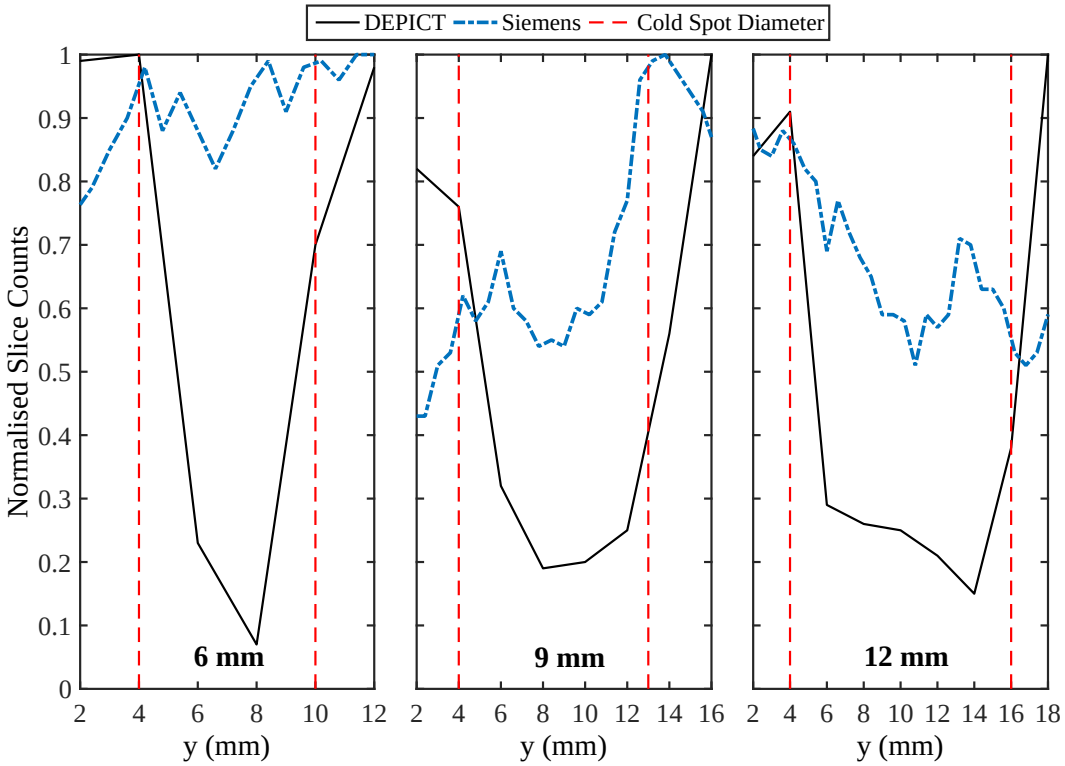

Figure 5.21: Normalised slices through the 6, 9 and 12 mm cold spot locations from data acquired with DEPICT and Siemens gamma camera.

have a small dip in the middle but this likely due to statistical fluctuations as is not lower than the data between 2 – 4 mm. The 12 mm data do decrease between the cold spot locations, however the overall slice tends to decrease rather than just between the dashed lines. Qualitatively, the cold spots were not visible in Figure 5.20b when the thyroid phantom was imaged with the Siemens gamma camera, however these results prove there are no significant reduction in counts at the known cold spot positions. This indicates that cold spots caused by malignancy in a thyroid image acquired with a clinical gamma camera may be missed, but can be detected with the DEPICT system.

The DEPICT slices were subsequently accessed to ascertain whether counts within the cold spots returned to background levels. The average background count from a subset of 77 pixels outside the thyroid cavity shape, illustrated by the dashed white lines in Figure 5.20a, was calculated as it would be expected that the counts from pixels within the cold spot were the same as background. The average background from multiple pixels was calculated to reduce the statistical errors that would arise from taking one slice through an area of background

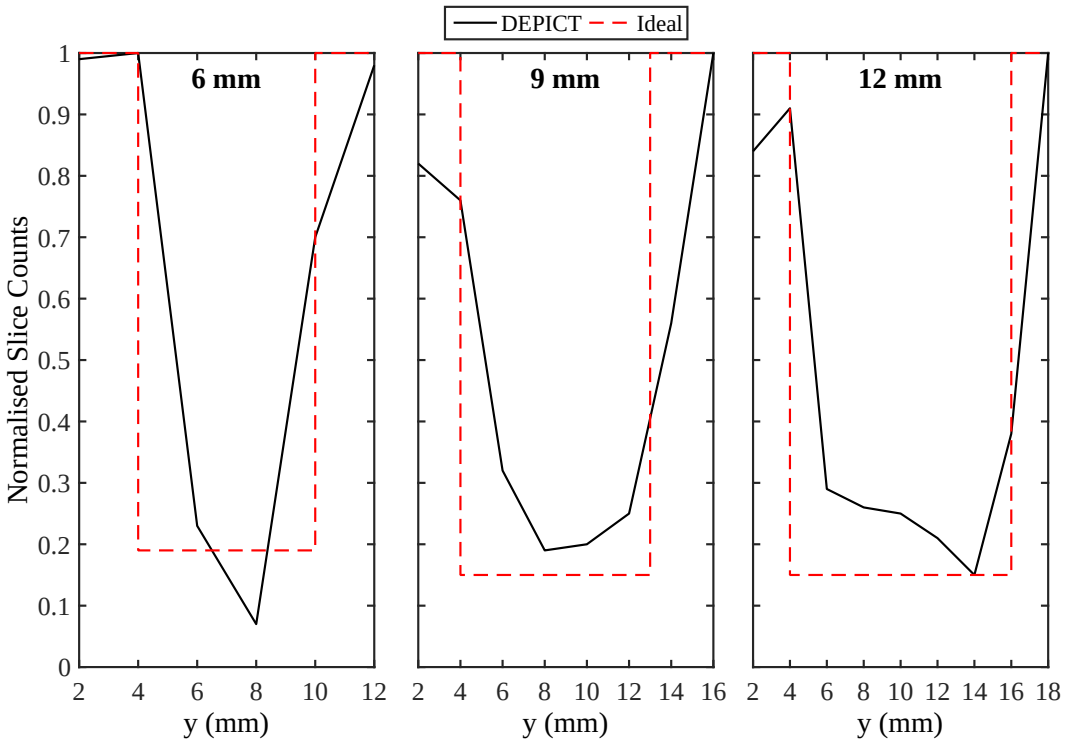

Figure 5.22: Normalised slices through the 6, 9 and 12 mm cold spot locations in DEPICT, with red dashed lines indicating the ideal step function with the base at background level.

with only ∼20 counts per pixel. This average background value was then normalised to the maximum count through each slice at 6, 9 and 12 mm. An ideal step function was plotted with the base of the step function at the average background level. These background values were 0.19, 0.15 and 0.15 normalised counts respectively for the 6 mm, 9 mm and 12 mm data. The average background count remains the same but is normalised to different maximum values. As there are statistical variations within the slice counts through the DEPICT cold spots, the average minima of each slice were calculated. This was achieved by summing the normalised counts of each pixel value that lay within the step function, between the red dashed lines, and diving by the number of pixels within that region. For the 6 mm data, the counts from 6 and 8 mm were averaged, giving a normalised minimum slice count of 0.15. For the 9 mm cold spot, the average normalised minimum slice count from summing counts at 6, 8, 10 and 12 mm and was calculated as 0.24. Finally, summing the normalised counts at 6, 8, 10, 12 and 14 mm gave a value of 0.23 for the 12 mm slice. The 6 mm cold spot data appears to drop below the background level. The slice through the cold spot contains only a small number of counts from a few pixels, compared to the average of 77 pixels for the

background data, therefore this may be due to a particularly low counting pixel. The pixel counts at the 9 mm and 12 mm cold spots do not completely fall to background level. The DEPICT data however, are much improved on Siemens data where the cold spots are not quantifiable.

The cumulative frequency method for obtaining the sizes of artefacts within an image was investigated with the data acquired with the thyroid phantom, as this is a much more complex test case than the individual vials in Figure 5.12b. For the slices illustrated through the 6 mm, 9 mm and 12 mm cold spots show in Figure 5.20a, the cumulative frequency of the slice counts were calculated and are plotted in Figures 5.23a, 5.23b and 5.23c, respectively. In addition, the cumulative frequency from a slice through the hot spot was also calculated. The slice selected was y = 24, from x = 19 – 40 and the cumulative frequency plot is shown in Figure 5.23d. For the slice through a cold spot, it is expected that the gradient of a line through pixels outside the cold spot will be relatively steep, with the gradient being shallow within the cold spot due to only a very small number of counts being summed from pixel-to-pixel. Conversely, through the hot spot it is expected the gradient of the line will begin shallow, increase through the known hot spot position as a high number of counts are being summed, before levelling off outside the hot spot.

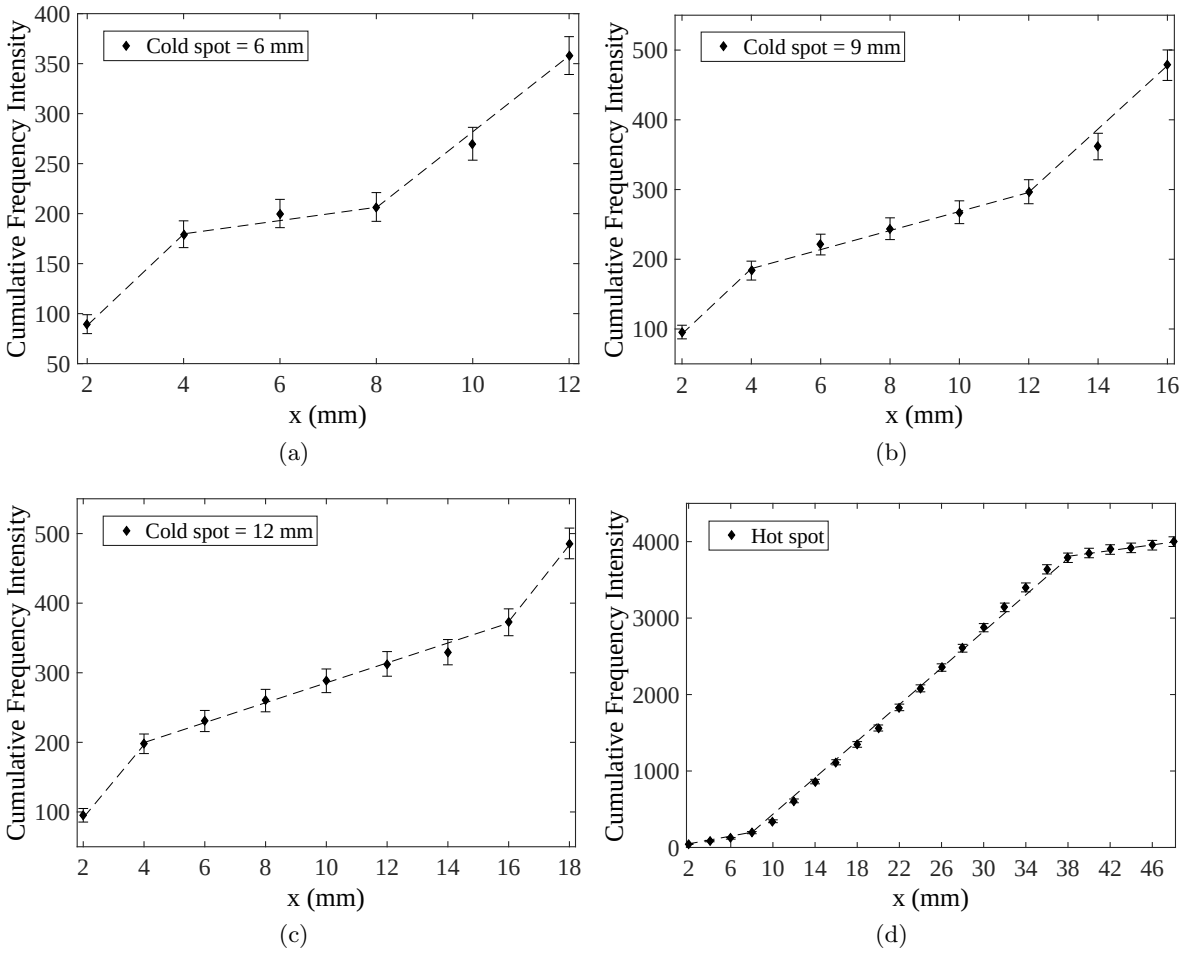

Figure 5.23: Cumulative frequency plots for slices through (a) 6 mm cold spot, (b) 9 mm cold spot, (c) 12 mm cold spot and (d) the hot spot from Figure 5.20a. The black dashed lines in each figure correspond to three straight lines fit to regions of varying gradients.

For each of the data sets in Figures 5.23a - 5.23d, there are three distinct areas to each plot that can be fitted with three straight lines of differing gradient, shown by the black dashed lines. For the 6 mm cold spot data in Figure 5.23a the gradient of the line between 2 and 4 mm is 45 counts/mm, decreasing to 7 counts/mm from 4 to 8 mm and increasing to 38 counts/mm from 8 to 12 mm. The gradient between 4 and 8 mm is less than 20% of that of the lines from 2 – 4 and 8 – 12 mm. This would indicate a cold spot of 4 mm in size. It is known that the cold spot is 6 mm in diameter, therefore the cumulative frequency method does not accurately reconstruct the known cold spot diameter. For the 9 mm cold spot data, this trend is reproduced with a gradient of 44 counts/mm between 2 – 4 mm, 14 counts/mm from 4 – 12 mm and 45 counts/mm from 12 – 16 mm. This would suggest the cold spot is 8 mm in diameter, which is smaller than the known diameter of 9 mm. For the 12 mm cold

spot data the gradient is 51 counts/mm from 2 – 4 mm, 14 counts/mm from 4 – 16 mm and 56 counts/mm from 16 – 18 mm. This indicates a cold spot of diameter 12 mm, which is consistent with the known cold spot size. Finally, for the hot spot cumulative frequency, the gradient is 24 counts/mm from 2 to 8 mm, increasing to 124 counts/mm from 8 to 38 mm and decreasing to 19 counts/mm from 38 to 48 mm. This suggests there is an area of increased counts or a hot spot of 30 mm. This is consistent with the known area of increased counts along this slice of 15 pixels in width. The cumulative frequency method for determining sizes of areas of interest within an image was found to be successful for cold spots of at least 12 mm in size and for hot spots. However, for cold spots of 6 and 9 mm in diameter, this method did not accurately reconstruct the known vial size. When the contrast within an area of an image is degraded, the cumulative frequency method has difficulty in accurately ascertaining the diameter of a region of interest.

5.6 Summary of Phantom Imaging Measurements

One of the key aims of the DEPICT project is to develop a system that can accurately delineate areas of interest. This was tested with the DEPICT system and compared to the Siemens gamma camera with vials of ^{131}I. Methods such as determining the cumulative frequency of a counts through a slice within an image have been established to quantify sizes of features in an image. It was accurately found to calculate the sizes of 10 mm inner diameter vials and cold spots greater than 12 mm in diameter. The DEPICT system has been shown to have improved image quality when imaging clinical activities of ^{131}I due to the superior spatial and energy resolution. The system spatial resolution at 10 cm was determined to be 2 mm, compared to 13.8 mm for a clinical gamma camera. The spatial resolution of DEPICT is ultimately limited by pixel size, but there is a compromise however, between decreasing pixel size to improve the spatial resolution and suffering from charge sharing. In addition, an increased number of smaller pixels leads to increased electronics for read out of more channels, that requiring increased cooling. A smaller number of counts would also be acquired per each pixel, increasing statistical error. Therefore, the DEPICT pixel size of 2 mm is a sufficient compromise. Finally, images acquired with a thyroid phantom were compared with DEPICT and a Siemens gamma camera. Cold spots that were visible in the DEPICT image were not distinguishable by the clinical system, highlighting the improved image quality.

Chapter 6

Activity Quantification and Tomography

Accurately quantifying the uptake of radioactivity within patients undergoing MRT is essential for personalised dosimetry. This requires the conversion of detected counts (in cps) in a region of interest into a value of activity (e.g. MBq). Image quantification, however, is regarded as the largest cause of inaccuracy in dosimetry. Firstly, there are camera limitations such as the spatial resolution, energy resolution and dead time. Secondly, degradation of the images from attenuation and scatter will cause errors in the quantification of activity. This chapter will investigate the feasibility of using DEPICT to obtain quantitative activity information from both planar and 3D images.

6.1 Relative Activity Quantification

To begin with, quantifying the relative activity of various regions of interest within an image was investigated using the thyroid phantom detailed in Chapter 5 and shown in Figures 5.18a and 5.18b. As the hot spot is twice the depth of the normal lobe, it should have twice the activity and hence twice the number of counts should be detected in comparison to the normal lobe. To investigate this, the ratio of counts in 1.44 cm^2 regions of interest within the normal lobe and the hot spot were compared to each other, using data acquired with both the DEPICT and the Siemens Intevo gamma camera; the expected ratio being 50%. The regions of interest were equidistant from the centre of the phantom, as highlighted by the white squares in Figures 6.1a and 6.1b. There is a section of perspex between the base of the thyroid cavity and the base of the phantom, therefore an attenuation correction needs

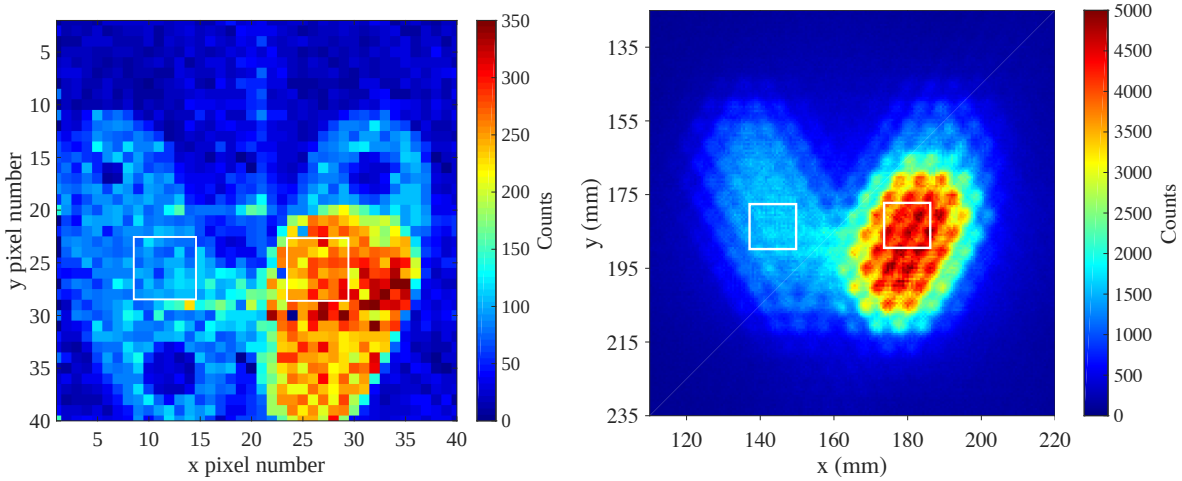

Figure 6.1: Thyroid phantom imaged with (a) DEPICT CZT detector and high-energy parallel-hole collimator and (b) Siemens gamma camera with high-energy general purpose collimator. The left hand square in each image highlights the data selected from the normal lobe; the right hand square shows the hot spot.

to be applied. The thickness of perspex between the normal lobe and the base of the phantom is 50 mm, whilst there is 32.5 mm between the hot spot and the base. An attenuation correction was performed using Equation 3.5, where the linear attenuation coefficient μ of perspex is 0.126 cm^{-1} [54]. As discussed in Section 3.6 attenuation correction is essential for accurate activity quantification measurements. The raw and attenuation corrected counts for the normal and hot spot regions for both images are shown in Table 6.1, along with the calculated ratios of both the uncorrected and corrected normal lobe counts to hot spot counts.

The ratio of uncorrected normal/hot lobe counts is 36.19 ± 0.73% for DEPICT and 37.86 ± 0.05% for the Siemens clinical gamma camera. The ratios increase to 45.12 ± 0.91% for DEPICT, and for the Siemens camera to 47.19 ± 0.07%, highlighting the importance of attenuation correction for quantifying activity. The ratios are consistent with one another, calculated using the consistency relationship $|x_1 - x_2| < 3\sqrt{\Delta x_1^2 + \Delta x_2^2}$ and within reasonable agreement of the known ratio of 50%. Corrections for self absorption have not been implemented. The statistical error calculated for the Siemens data is much smaller because there are significantly increased counts due to the higher throughput of γ rays through the clinical collimator. In clinical gamma camera imaging of the body, it would be necessary to use multiple attenuation coefficients for tissues of differing densities.

	DEPICT	Siemens
Uncorrected normal lobe counts (x10^3)	3.34	695.39
Uncorrected hot spot counts (x10^3)	9.24	1836.98
Ratio of normal/hot uncorrected counts (%)	36.19	37.86
Error on ratio (%)	0.73	0.05
Corrected normal lobe counts (x10^3)	6.28	1305.67
Corrected hot spot counts (x10^3)	13.91	2766.61
Ratio of normal/hot corrected counts (%)	45.12	47.19
Error on ratio (%)	0.91	0.07

Table 6.1: Raw and attenuation corrected counts for normal lobe and hot spot for the DEPICT and gamma camera images.

6.2 Distance Dependence

Although it is useful to extract the relative activity uptaken to different regions of interest, the absolute activity is a more valuable measurement for dosimetry and treatment verification. To be able to determine the calibration factor for converting measured count rate (cps) into absolute activity (GBq), it is necessary to determine if there is a geometrical dependence on the detected count rate. If this was the case, the calibration factor that is required to convert counts into an activity would also need to vary as a function of distance between the thyroid and DEPICT. It is expected in clinical implementation that the distance between the thyroid and DEPICT will be approximately 10 cm [118], however this could vary according to the patient geometry. In order to investigate the geometrical relationship between measured counts and distance, data were acquired with a dose calibrator reference vial of ^{133}Ba, shown in Figure 6.2 [119]. The vial was manufactured by distributing the active element in 20 ml of epoxy, comprising a density of approximately 1.0 g/cm^3 and supplied in a 27 ml polyethylene vial. A distributed source, rather than a point-like source, was selected for this measurement as it mimics the scenario of imaging activity contained in the thyroid. The diameter of the base of the vial is 31.2 mm, as shown in Figure 6.2a. The ^{133}Ba vial was mounted onto a mechanical scanning arm, shown schematically in Figure 6.2b, which accurately positioned the vial at distances of 2, 4, 6, 8 and 10 cm from the face of the collimator. The scanning arm is

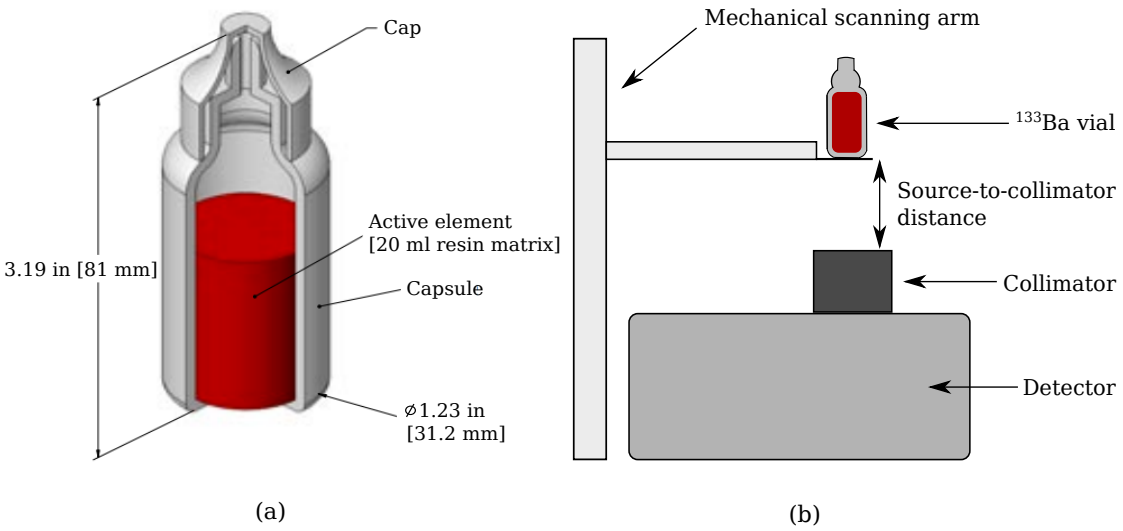

Figure 6.2: (a) Image of the ^{133}Ba vial and (b) a schematic of the experimental setup with the ^{133}Ba vial on mechanical scanning arm at a distance from collimator face.

controlled by a Velmex VXM Stepper Motor Controller [120] that has the capability to drive and control precise linear movement and was selected to minimise any errors in positioning the source as the only variable is the distance to the collimator. Although ^{133}Ba provides an excellent analogue to ^{131}I γ emissions, the activity of the vial at the time of measurement (8.39 MBq) was several magnitudes lower than that used in therapy (a few GBq). A data collection time of 20 hours for each distance was therefore selected to minimise statistical uncertainties. An energy gate of 340 to 360 keV was applied when using the ^{133}Ba source, which removes contribution from scattered γ rays and maximises signal to noise in the image. This energy window is shown in the ^{133}Ba spectrum in Figure 6.3.

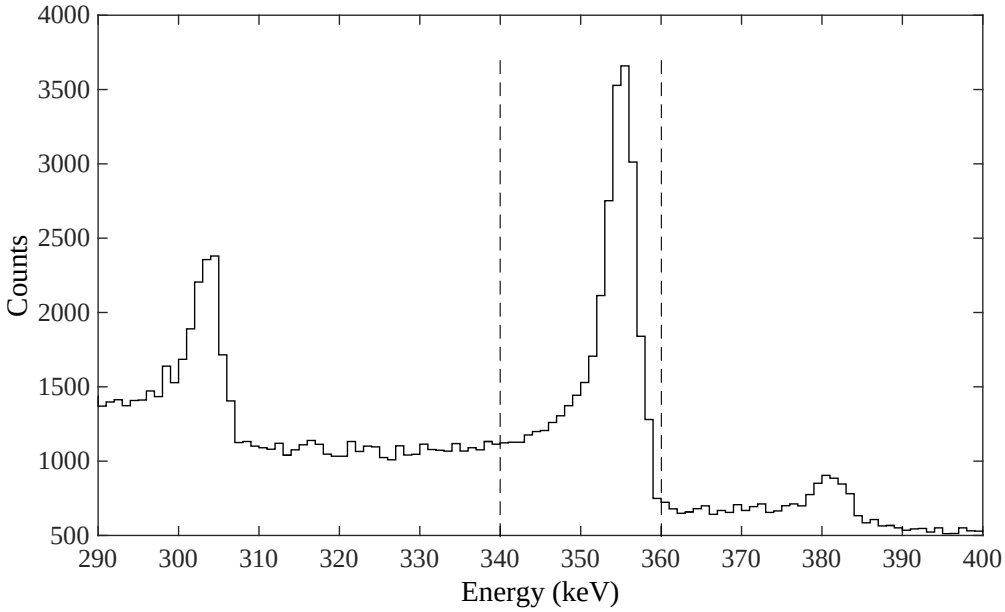

Figure 6.3: Energy spectrum acquired with the distributed ^{133}Ba source. The dashed black lines highlight the 340 – 360 keV energy window.

The average counts per pixel at each distance was calculated by summing the counts from all pixels and dividing by the total number of pixels. Known noisy pixels were manually switched off and not included in the analysis, which left 478 useful pixels. The results are shown in Table 6.2. The average pixel counts obtained for the source at each measurement position are all directly comparable as the collection time was the same (20 hours) and activity loss over the total 100 hour data collection is negligible for 133Ba ($t_{1/2phys}$ = 10.51 years).

Source-to-collimator distance (cm)	Total counts	Average counts per pixel	Error on average pixel count
2	34227	71.61	8.46
4	33688	70.48	8.39
6	34119	71.38	8.44
8	34004	71.14	8.43
10	34758	72.72	8.53

Table 6.2: Counts as a function of source-to-collimator distance for all pixels.

The average number of counts per pixel range from 70.48 to 72.72 and do not appear to follow a direct relationship with distance. Instead, the fluctuations can be attributed to statistical uncertainties and all average pixel counts are within $\sqrt{N}$ of one another. This is an expected result as it is known parallel hole collimators have a count rate that is independent of distance [55] which is ideal for clinical measurements as distance dependent calibration factors are not

required. Measurements can now be undertaken to determine a suitable calibration factor and investigate the feasibility of absolute activity quantification.

6.3 Planar Absolute Activity Quantification

In order to perform absolute measurement of the activity in regions of interest, the calibration factor, or planar sensitivity (cps/GBq) of the system must be known. To determine the DEPICT system sensitivity, the National Electrical Manufacturers Association (NEMA) System Planar Sensitivity test for discrete pixel detectors was followed [108]. NEMA standard tests were developed to provide a uniform criterion for the measurement and reporting of performance parameters for gamma cameras. Planar sensitivity corresponds to the sensitivity in one acquisition plane to a specifically defined planar source placed parallel to that plane and are dependent on collimator type, energy window width, γ-ray energy, source configuration and other factors. The NEMA test states a dose calibrator for accurate activity measurements and flat plastic dish (e.g. petri dish) are required. A petri dish with a small enough diameter for the DEPICT CZT detector was not available, therefore a vial with a base diameter of 30 mm was used. The system sensitivity must be determined for the energy window used with a particular radionuclide therefore the energy window was set at 355 – 375 keV, which is the energy window used with ^{131}I ($\sim$ 5%). The vial was filled with 3.45 GBq of ^{131}I and placed 10 cm from the face of the collimator, which is expected to be the approximate distance between the thyroid and DEPICT in future clinical implementation. The uncertainty on the calibrator used to measure the activity is 3%. As only events within the photopeak window are considered, the activity needs to be multiplied by the emission probability of the 364.5 keV γ rays emitted from ^{131}I, which is 81.7%. Therefore, the 364.5 keV photopeak activity was 2.82 GBq. Data were collected for 120 seconds and the number of counts within the photopeak was measured. A background measurement was also collected without the vial for 120 seconds.

The total number counts within the 355 – 375 keV energy window was 18522 $\pm$ 136, after background subtraction. The energy gated pixel map image acquired is shown in Figure 6.5a, without any uniformity or scatter corrections applied. The data acquisition time of 120 seconds gives a sensitivity, or number of detected photopeak counts per unit time per unit source activity, of 54.73 cps/GBq. To increase the accuracy of the calculated sensitivity

value, two corrections can be applied to each pixel; a uniformity correction and a scatter correction. The uniformity correction was applied using the uniformity factors matrix shown in Figure 5.4b. It is known that a portion of the counts within the photopeak may arise from Compton scattered events, due to ^{131}I emitting γ rays higher in energy than 364.5 keV. Therefore, the Triple Energy Window (TEW) scatter correction method was used [121] to remove scatter events. The true primary γ-ray emissions C_{prim} are given by:

$$C_{prim} = C_{total} - C_{scat}, \tag{6.1}$$

where C_{total} and C_{scat} are the total photopeak counts and counts arising from scattering events, respectively. The subtraction is carried out using two sets of data: the counts acquired within a main window centred on the photopeak energy, and the counts from two sub-windows, positioned either side of the the main window. The scattered γ rays included in the main window are estimated from the counts acquired within the sub-windows. Figure 6.4 illustrates the main photopeak window and the sub-windows to the left and the right of the photopeak window. The TEW correction method is more suitable with ^{131}I than the dual window correction method [122] (where there is only a left window and main window) as the right window will account for scatter from emissions above 364.5 keV.

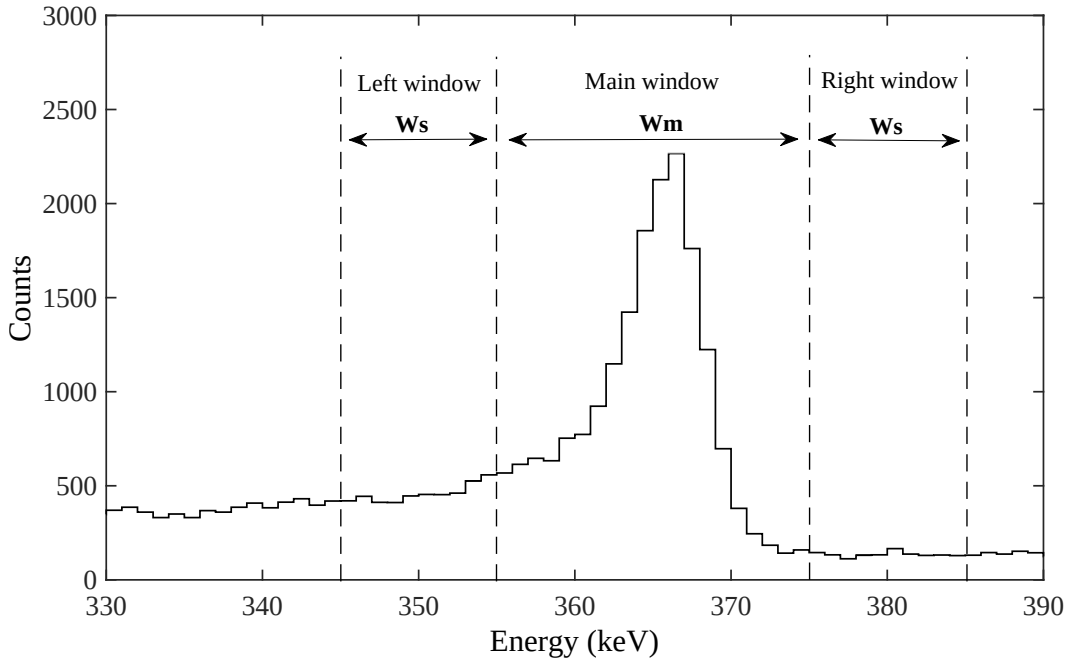

Figure 6.4: ^{131}I sum spectrum acquired for planar sensitivity measurement showing left, main and right windows for Triple Energy Window (TEW) scatter correction.

The width of the main window is defined as W_m and that of the sub-windows as W_s. The scattered counts in the photopeak C_{scat} can be estimated from a linear interpolation between the two sub-windows, following a trapezoidal approximation of scatter counts:

$$C_{scat} \cong \left(\frac{C_{left}}{W_s} + \frac{C_{right}}{W_s} \right) * \frac{W_m}{2} \tag{6.2}$$

where C_{left} and C_{right} are the counts in the left and right windows, respectively. The left scatter window was defined between 345 – 355 keV and right scatter window between 375 – 385 keV. To obtain the total counts C_{total}, the uniformity corrected counts from each pixel were summed and the value of C_{scat} was acquired by summing the scatter correction to each pixel. The planar system sensitivity (cps/GBq) was then determined by dividing the true counts of the planar scan (photopeak minus scatter counts) by the known activity and acquisition time. Figure 6.5b shows the pixel map following the application of uniformity and scatter corrections applied to each pixel. Table 6.3 lists the values of C_{total}, C_{scat}, C_{prim}, acquisition time, C_{prim} (cps), source activity and calculated sensitivity.

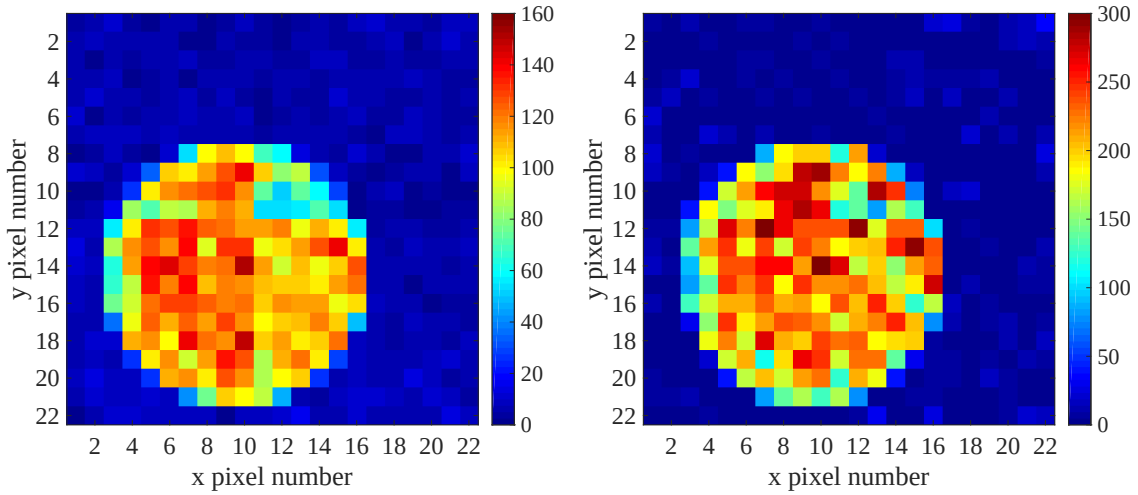

Figure 6.5: Energy gated pixel maps of (a) raw counts acquired from imaging the 30 mm diameter vial and (b) with uniformity and scatter correction applied to each pixel. Note the difference in scales.

Although the pixel counts in Figure 6.5b are expected to become more uniform with the application of a uniformity correction, it is known from the previous measurements that the correction is suboptimal. In addition, the small number of counts per pixel mean the counts in the sub-windows W_s are large, relative to the main window W_m giving large statistical

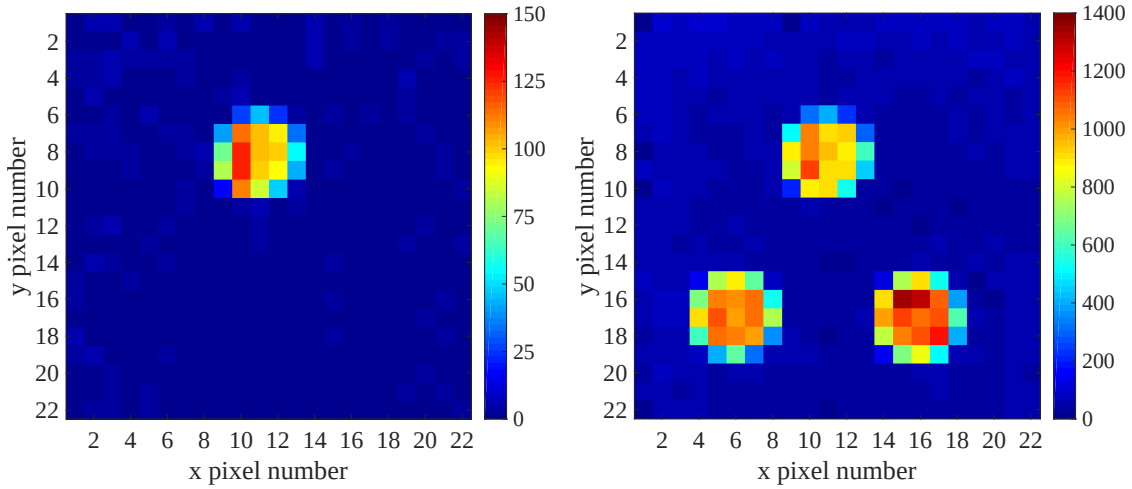

(a) (b)

Figure 6.6: Raw (uncorrected) data acquired using DEPICT for (a) 1 vial and (b) 3 vials containing ^{131}I.

fluctuations in pixel counts. It is expected this effect would improve with a longer data collection time.

C_{total}	C_{scat}	C_{prim}	Time (s)	C_{prim} (cps)	Activity (GBq)	Sensitivity (cps/GBq)
47563	26967	20597	120	171.6	2.82	60.87

Table 6.3: Values for calculation of scatter correction and sensitivity. All values are uniformity corrected.

The new value for sensitivity, calculated following the application of uniformity and scatter corrections is 60.87 cps/GBq, shown in Table 6.3. Data were subsequently acquired to determine the feasibility of using both system sensitivity values for activity quantification. For this, data were acquired with a single vial and 3 vials filled with ^{131}I. Figures 6.6a and 6.6b show the energy gated pixel maps acquired for these two data sets. The single vial had a total activity of 1.14 $\pm$ 0.03 GBq as measured by a dose calibrator with an error of 3% and the three vials had a total sum activity of 3.37 $\pm$ 0.06 GBq. The total error on the three vial sum activity is found by adding the errors of each individual vial in quadrature due to the propagation of errors. Both data sets were acquired for 600 seconds and each vial had an inner diameter of 10 mm. Before the total counts could be calibrated into an activity, three corrections needed to be applied:

- Attenuation Correction

  Unlike the calculations for the sensitivity values where there was no attenuating material between the vial and the collimator, the 1 and 3 ^{131}I vial data sets were acquired with the vials placed in the Jaszczak phantom shown in Figure 5.10a. Therefore, an attenuation correction (AC) needed to be applied to each pixel to account for the 2 cm perspex material at the base of phantom using Equation 3.5.

- Uniformity Correction

  As with previous data sets, a uniformity correction (UC) was performed using the uniformity matrix shown in Figure 5.4b.

- Scatter Correction

  A TEW scatter correction (SC) was applied to each pixel for the data acquired with 1 and 3 vials.

The AC and UC were applied to the main energy window and two sub-windows for each pixel in each data set. This meant that when using Equation 6.2 to determine the scatter contribution, the sub-window counts were also corrected for attenuation and uniformity to make the counts comparable. Table 6.4 shows the total photopeak counts following the application of attenuation, uniformity and scatter corrections. Following AC, the total counts for each vial increases, due to the recovery of counts that were lost by attenuation in the perspex. The UC increases total counts by about 40% as it is known there is a reduction in counts at the edges of each of the four modules and the SC reduces the counts as scattered counts within the photopeak window have been removed.

	Total raw counts	After AC	After AC + UC	After AC + UC + SC
1 vial	2366	3044	8683	3627
3 vials	70881	91195	232881	96711

Table 6.4: Total counts before and after attenuation AC, uniformity UC and scatter SC corrections.

The total counts acquired for the single vial data after the application of the three corrections was 3627. Since the data collection time was 60 seconds, this gives a value of counts per second (cps) of 60.54. The total counts acquired over a 600 second period for the 3 vial data was

96711, giving a cps value of 161.19. These values were divided by each sensitivity value to give a value of activity in GBq and are shown in Table 6.5.

	1 vial activity (GBq)	3 vial activity (GBq)
Sensitivity value 1 (54.73 cps/GBq)	1.11	2.95
Sensitivity value 2 (60.87 cps/GBq)	0.99	2.65

Table 6.5: Calculated activities for 1 and 3 vials of ^{131}I using sensitivity values.

The calculated activities of the single vial were 1.11 ± 0.16 GBq and 0.99 ± 0.14 GBq, respectively, using sensitivity values 1 and 2. The photopeak activity of the single vial was 0.91 ± 0.03 GBq. The calculated value for activity using sensitivity value 2 is within errors of the known vial activity, whilst that calculated using sensitivity value 1 is not. The calculated activities for the 3 vial data were 2.95 ± 0.28 GBq and 2.65 ± 0.26 GBq, using sensitivity values 1 and 2, respectively. Although the calculated activity using sensitivity value 2 is closer to the know total photopeak activity of the 3 vials of 2.73 ± 0.05 GBq, both calculated activities are within errors of the known activity value and were calculated to be consistent with the using the consistency relationship $|x_1 - x_2| < 3\sqrt{\Delta x_1^2 + \Delta x_2^2}$. These results show planar activity quantification with DEPICT is feasible, with improved values calculated when corrections are implemented for the image degrading factors such as attenuation and scatter.

6.4 Tomographic Reconstruction

The results obtained for planar imaging with DEPICT have been shown as superior to those obtained with a clinical gamma camera. However, a further challenge for the device will be producing 3D images of the 3D volumes of interest, by acquiring data at multiple angles to be input to tomography algorithms. This results in a SPECT image, rather than a planar gamma camera image. The feasibility of obtaining 3D images with the DEPICT system was investigated. For tomographic reconstruction, the open-source software NiftyRec [123] was utilised in Matlab to reconstruct data using an Ordered Subset Expectation Maximisation (OSEM) algorithm. The ^{133}Ba vial source shown in Figure 6.2 was mounted onto a rotating scanning table and data were collected for the vial at various angles to the DEPICT gamma camera, shown in Figure 6.7a. The scanning table was a Velmex Rotating Table [124] designed

to allow motorised continuous 360° rotational motion. Data were collected over 360°, at 10° increments, with the data collection time for each step set at 28,800 seconds (8 hours). The long counting times were necessary due to the low source activity of 8.59 MBq and would be decreased significantly in clinical implementation for GBq activities. The distributed ^{133}Ba source shown in Figure 6.2a was used for data collection. With the vial mounted vertically, the middle of the resin was 6.5 cm from the face of the collimator. Data were recorded at every 10° increment as a csv file, containing list-mode data which was input to the NiftyRec Matlab code. The first process performed by the code was calibration of the raw data using a calibration file, and the application of an energy gate to veto events arising from outside the photopeak. A planar image is produced for each angle of rotation θ and all the planar images are saved into a 3D matrix of x, y, θ, where x and y are the 22 x 22 pixels. A common way of presenting this information is in the form of a 2D matrix, known as a sinogram [125]. A sinogram produces a 2D cross-sectional image of the activity from a slice within the object at each angle θ. A slice was taken through the 3D matrix to create a sinogram for y pixel number = 18 and is shown in Figure 6.7b. Each column represents a single row in the projection image arranged in increasing angular order. The goal of an iterative reconstruction algorithm such as OSEM is to estimate the object from a measured sinogram.

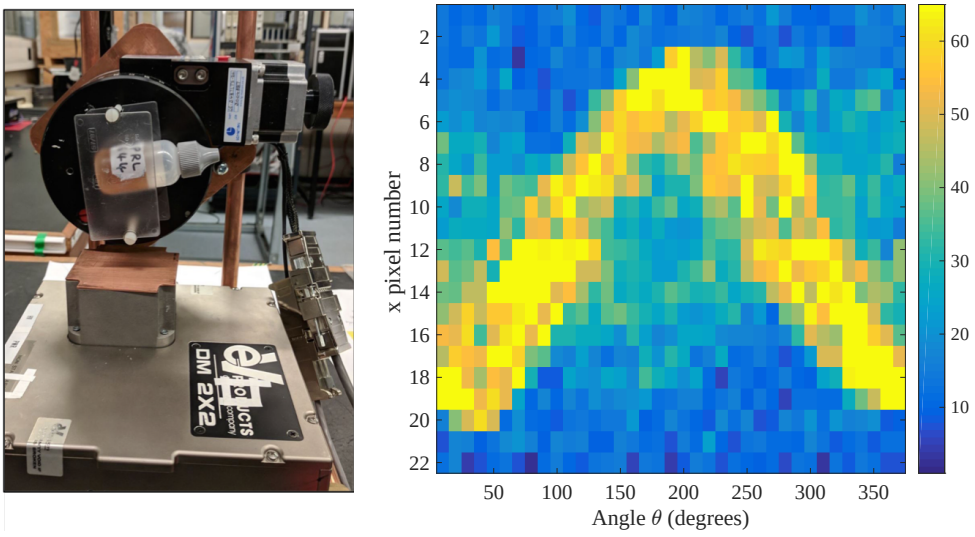

(a) (b)

Figure 6.7: (a) ^{133}Ba vial mounted onto the rotating scanning table above the DEPICT collimator and (b) a sinogram produced from a slice through the data acquired at each angle.

The second process within the code applies the OSEM algorithm to the 3D data. It is possible to optimise the output of the reconstruction by varying user inputs. The most important of these is the iteration number, which corresponds to the number of OSEM iterations. For each iteration, a closer estimate of the true counts distribution is achieved, however too many iterations can generate unwanted noise. The output of the code following application of the algorithm is a text file with four columns of the format x, y, z and intensity, where the x, y, z values give the coordinates of reconstructed counts (intensity) in 3-dimensions. The programme TopCat [126] (Tool for Operations on Catalogues and Tables), which is an interactive graphical viewer and editor for tabular data, was then utilised to view the contents of the text file. It has the functionality of 3D plotting using cartesian coordinates where points in 3D are coloured according to their intensities.

Initially, one iteration was used with 2 OSEM subsets. The reconstruction produced is shown in Figure 6.8a. The reconstructed 3D cylindrical volume is expected to have a base diameter and height of 16 pixels. This reconstructed image has counts in every voxel (3D pixel) and does not resemble the ^{133}Ba vial, however it is known that OSEM algorithms generate a very simple initial image estimate for one iteration. The number of iterations was therefore increased to 5 and the subsequent reconstructed image is shown in Figure 6.8b. Figure 6.8b appears to show a concentrated region of counts within the centre of the image where the vial is known to be, indicated by an increase of purple coloured voxels of 50 – 70 counts, but it still does not resemble a reconstruction of the ^{133}Ba vial. For each planar image obtained at each reconstruction angle, counts are acquired in every pixel. These counts are either true photopeak counts, as an energy gate was applied, or background. Hence, all the background counts will also undesirably get reconstructed and these counts will be masking the true vial shape. Therefore, the data were reprocessed with a suitable threshold was applied to the reconstructed counts to attempt to clean up the image. A threshold was selected that visibly removed unwanted counts from the image, whilst retaining the counts at the known vial position. Example reconstructed images, following the application of a threshold are shown in Figures 6.9, 6.10 and 6.11 for 1, 15 and 150 iterations.

Figure 6.9 shows that applying a threshold with the simple initial condition of one iteration removes unwanted background counts, and a reconstructed image that resembles a the

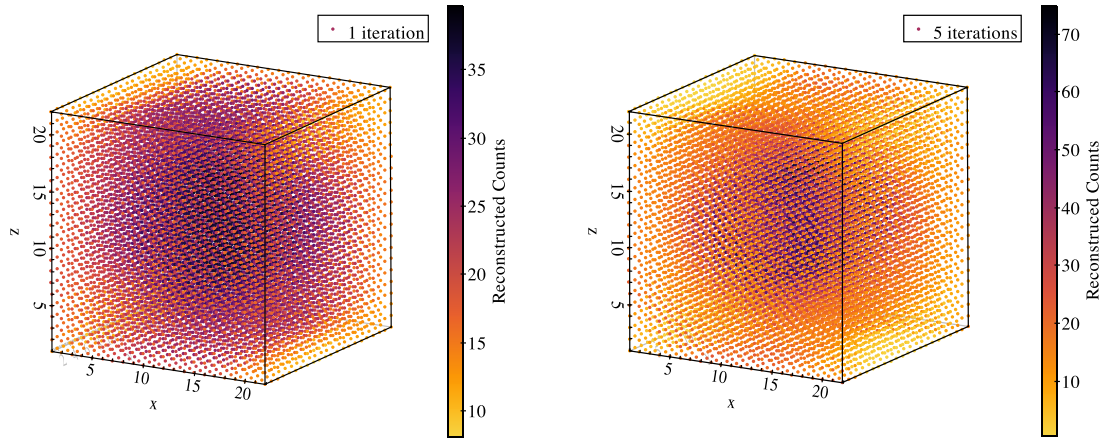

Figure 6.8: 3D reconstructed ^{133}Ba vial following (a) 1 iteration and (b) 5 iterations.

cylindrical shape of the ^{133}Ba distribution is evident. The size of the reconstructed volume however, is much larger than the known vial size. Increasing the number of iterations to 15 for example, shown in Figure 6.10, produces a much more accurate 3D representation of the ^{133}Ba vial. It does appear that the activity is not evenly distributed within the epoxy resin as the counts are not constant across the reconstructed volume. There are counts of approximately 100 towards to centre of the volume, with regions of around 200 counts towards the vial edge. At the maximum iteration number used for this analysis of 150, the volume does not resemble the known shape and it appears to be suffering from edge enhancement [127]. This edge artefact can occur at high iteration number near edges where the radioactivity concentration level changes appreciably within a small distance, such as the edge of a vial, enhancing edge activity whilst underestimating the activity at the centre of the vial.

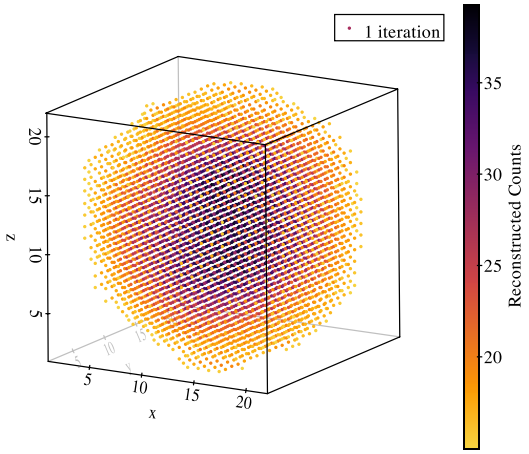

Figure 6.9: 3D reconstructed ^{133}Ba vial after 1 iteration, with a threshold of 30 reconstructed counts.

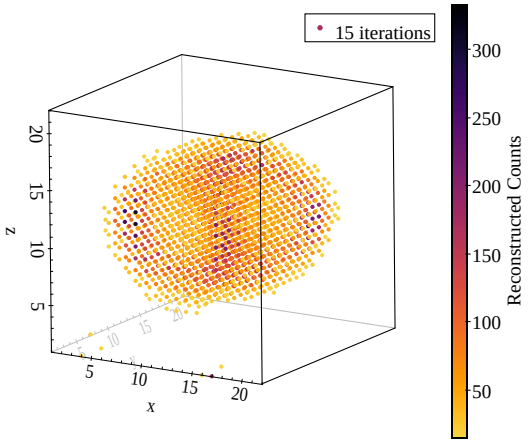

Figure 6.10: 3D reconstructed ^{133}Ba vial after 15 iterations, with a threshold of 30 reconstructed counts.

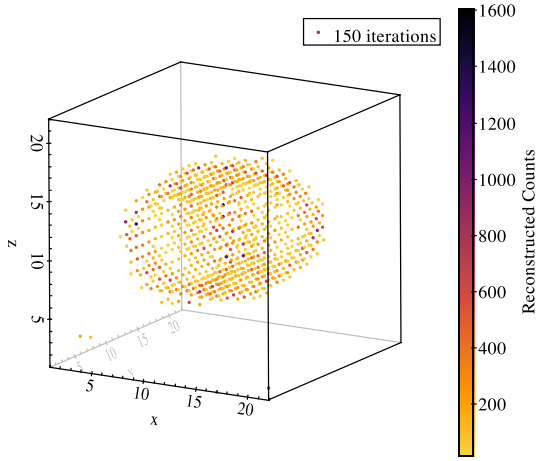

Figure 6.11: 3d reconstructed ^{133}Ba vial after 150 iterations, with a threshold of 30 reconstructed counts.

Following the application of a threshold, an investigation into the optimum number of iterations for this data was conducted. It is known that the total reconstructed counts within an image will remain constant with increasing iteration number. However, for the reconstructed counts within a volume of interest in an image, such as the vial in this data analysis, the reconstructed counts will increase with increasing iteration number as the algorithm produces better estimates of the actual distribution of the counts. However, above a certain iteration number (that will vary for every data analysis with OSEM algorithms) the counts will saturate. This means the iterative code has converged to the maximum likelihood estimate of the count distribution and further iterations do not improved the estimate, but increase noise. Due to the probabilistic nature of the reconstruction algorithm, every time it is applied to the data a unique 3D count distribution is produced. Therefore, for the investigation into the optimum iteration number, the data has been processed by the reconstruction code three times to obtain an average total number of reconstructed counts at each iteration number over a range from 1 to 150 iterations. The average total reconstructed counts within the volume of interest have been plotted as a function of iteration number and is shown in Figure 6.12.

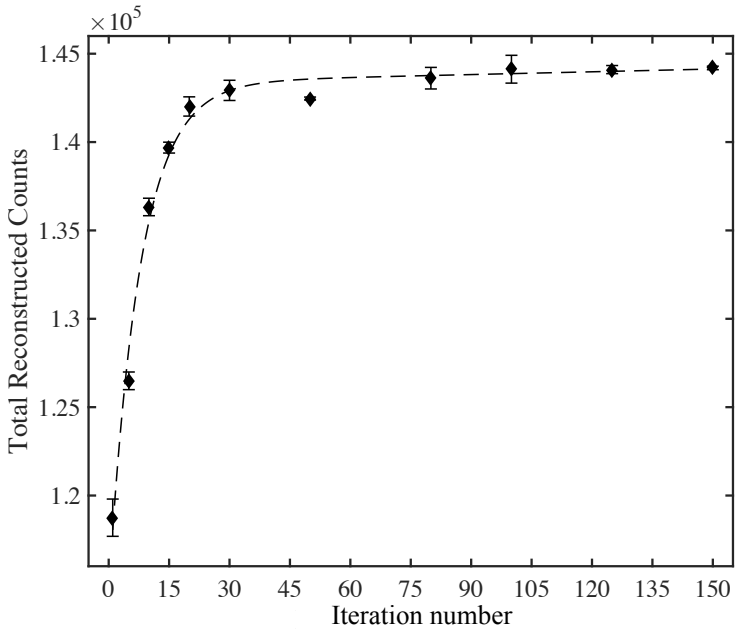

Figure 6.12: Total average reconstructed counts within the volume of interest as a function of the number of iterations for the NiftyRec OSEM algorithm.

A fit has been applied to these data, which follows a second order exponential $y = ae^{bx} + ce^{dx}$ where a = 1.43e+5, b = 3.64e-5, c = -2.88e+4 and d = -0.13. The shape of this plot is as described above and is typical for increasing iteration number in OSEM algorithms [128, 129, 130]. For this data, the total reconstructed counts saturate above approximately 30 iterations. The total reconstructed counts at 50 iterations appears to be anomalous as it does not follow the fit to the data. Ideally, an iteration number would be selected that lies on the area of the graph that curves just before the plateau, giving a compromise between increased image noise and optimum estimate of reconstructed counts. For this data, an iteration number of 15, 20 or 30 would satisfy this criteria.

To further investigate the optimum iteration number, the reconstructed 3D images produced at each iteration number were compared to see if they resembled the true dimensions of the ^{133}Ba vial. A histogram was plotted showing the total reconstructed counts integrated over the y-direction for each value along the x-axis. This would indicate the reconstructed diameter of the base of the vial and was used as a measure of how accurately the reconstructed image resembled the true volume. An example histogram of 15 iterations is shown in Figure 6.13.

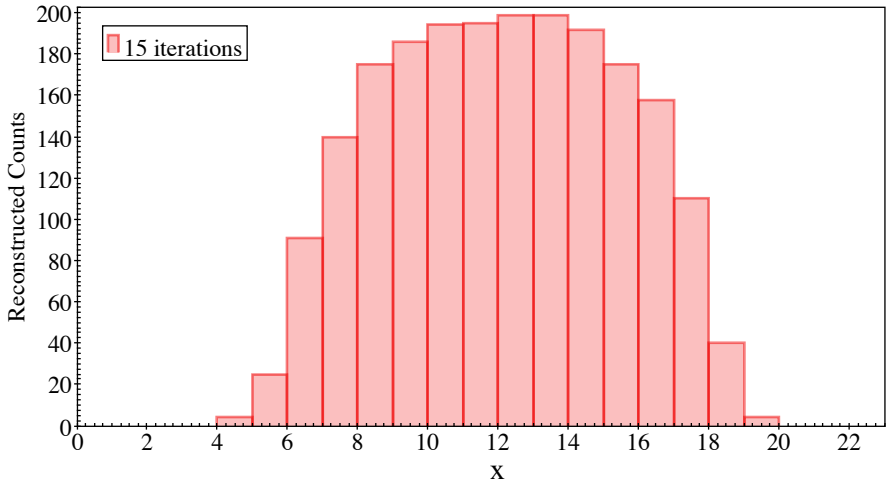

Figure 6.13: Histogram showing total reconstructed counts in the y-direction for each x value. Data shown is for 15 iterations.

The known vial diameter is 31.2 mm therefore due to the DEPICT pixel size of 2 mm, the vial should produce counts across 16 pixels because of partial volume effects. For the histogram shown in Figure 6.13, counts are distributed in the x-axis from 4 – 20. As counts are acquired

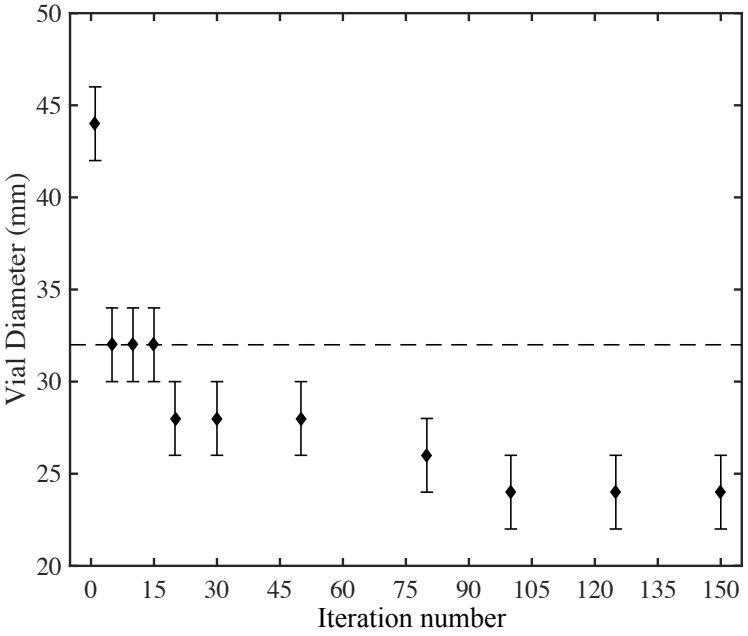

Figure 6.14: Vial diameter determined from histograms as a function of iteration number. Dashed line shows real vial diameter.

over 16 pixels and these counts are known to be attributed to the reeconstructed vial volume at that iteration number, the reconstructed vial diameter was taken as 16 pixels (32 mm), accurately reconstructing the known diameter. The vial diameters acquired from histograms at various iteration numbers from 1 – 150 were plotted as a function of iteration number in Figure 6.14. In Figure 6.14, the dashed line illustrates the known vial diameter and the error on the measured vial diameter is 2 mm as this is the smallest size the DEPICT detector can measure. Figure 6.14 shows that for these data, there are three iteration numbers where the vial size is accurate; 5, 10 and 15 iterations. Above this, the vial decreases in size. This is possibly due to the edge enhancement effect skewing the size of the reconstructed vial. For this data, 15 iterations was selected as the optimum OSEM iteration number as it gives the best estimate of counts, reduced noise, whilst also accurately reconstructing the known vial size.

To be able to extract quantitative activity information for the 3D reconstruction, corrections would need to be applied within the reconstruction algorithm for scatter, attenuation, partial volume effects and collimator-detector response [128]. In addition, calibration data would need to be acquired for conversion of reconstructed counts to absolute activity. The extent

and complexity of the work required to achieve accurate 3D activity quantification is beyond the scope of this thesis. A review paper describing the different parts in the dosimetry chain for radionuclide therapy, with emphasis on activity quantification from SPECT images to achieved personalised dosimetry is found in [34].

6.5 Summary of Activity Quantification Measurements

Relative activity quantification was performed for regions of interest within a thyroid phantom where the known activity ratio is 50%, highlighting the important of attenuation correction in activity quantification. Planar quantification of the radioactivity within vials containing ^{131}I has been achieved using DEPICT to within 9% of the known activity for data acquired with 1 vial and 3% for data with 3 vials, using a system sensitivity value calculated to be 60.81 cps/MBq. Tomographic imaging of a ^{133}Ba vial was successful with an OSEM iterative reconstruction algorithm, with analysis undertaken to determine the optimum iteration number. For these data, 15 iterations and 2 subsets was found to accurately reconstruct the vial. Future work may look to implement corrections to account for factors that degrade the quantitative accuracy of a 3D reconstructed image.

Chapter 7

Further Clinical Applicability of DEPICT

As discussed in Section 2.2, ^{131}I treatment is the most established example of MRT. Radioiodine treatment for thyroid cancer and diseases has proven so successful, treatments have remained largely unchanged in over 70 years since it was first used. However, there appears to be a lack of progression in MRT, relative to EBRT, and this is due to only a small number of patients being treated with this modality, usually with rare cancers and only for palliative intent [131]. Treatments however, are steadily increasing. For example, a large survey by the Internal Dosimetry Users Group showed almost three times as many treatments were carried out in 2015 compared to 2007 [132] and this trend is predicted to continue. This will be aided by MRT entering a new era in which a number of innovative therapeutic radionuclides are being used clinically. These radionuclides open up MRT as a treatment modality for a larger variety of cancers and diseases. However, treatments with emerging nuclides for therapy such as ^{177}Lu, are much more expensive than those with radioiodine. It can cost approximately £70,000 per treatment cycle involving six intravenous administrations of 7.4 Gq [133], compared to ∼£300 for a capsule of ^{131}I, so utilising them efficiently is crucial which can only be achieved through dosimetry. Experimental γ-ray spectra of emerging radiotherapeutics were acquired with DEPICT at The Royal Marsden Hospital and are presented in this chapter.

Increasingly in MRT, a combination treatment using multiple nuclides simultaneously is being discussed [134, 135]. For example, using a high-energy β-emitter such as ^{90}Y, suitable for treating larger tumours, alongside the lower-energy ^{177}Lu for smaller tumours may offer a

more effective treatment [136]. In addition, simultaneous multi-nuclide imaging would offer great advantages in diagnostic SPECT such as the reduction of positional errors that may be suffered when multiple images with different nuclides have to be acquired over various days. As the future of MRT will only progress by using new radionuclides or multiple nuclides in combination, the feasibility of simultaneous multi-nuclide imaging has been investigated with the DEPICT system in this chapter. The aims of this chapter are therefore to:

- Assess the spectroscopic performance of DEPICT for other radiotherapeutics.
- Evaluate the multi-nuclide imaging performance of DEPICT.
- Perform a preliminary study of collimator design for other radiotherapeutics.

7.1 Emerging Radionuclides for Therapy

Table 2.1 details the radionuclides that have been highlighted as having characteristics suitable for use in MRT, either purely for therapy or as a theranostic. Although there appears to be many radionuclides with suitable decay emissions and half-lives, the radionuclides need to be labelled to suitable pharmaceuticals with an appropriate biodistribution to target the radiation specifically to the disease sites. The recent introduction of antibodies and small molecules has allowed this [9]. Four of the nuclides listed in Table 2.1 that are emerging in MRT were measured with the DEPICT CZT detector in order to acquire a γ-ray spectrum and are shown in the following sections. Data were collected at The Royal Marsden Hospital with each source for 300 seconds. For comparison, spectra with each nuclide were also acquired with a clinical gamma camera, with varying acquisition times. As only spectral information was desired, the data were collected intrinsically without a collimator present allowing a high number of statistics to be acquired within a short time.

7.1.1 ^{177}Lu

^{177}Lu is a desirable radionuclide for MRT from a physical perspective as it has a favourable half-life $t_{1/2phys}$ of 6.7 days, a concentrated energy deposition due to its low-energy β emissions, and the emission of γ rays that enable imaging of the biodistribution. ^{177}Lu can be coupled to various pharmaceuticals for the treatment of neuroendocrine and prostate cancers. A ^{177}Lu spectrum was acquired with DEPICT and a 3 MBq source and is shown in Figure

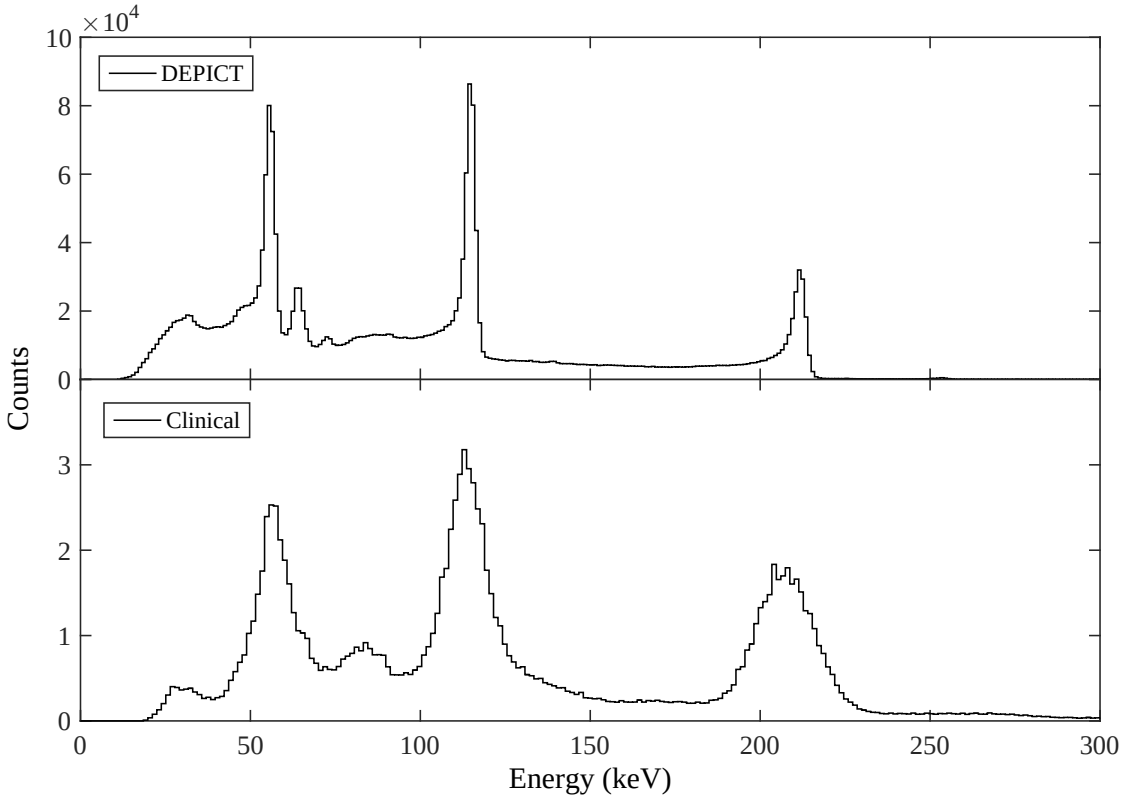

Figure 7.1: ^{177}Lu γ-ray spectrum acquired with DEPICT and the clinical gamma camera. The γ rays of interest are 113 keV and 208 keV.

7.1. ^{177}Lu has two γ rays that can be used for imaging, with energies of 113 and 208 keV. The 208 keV γ ray has a greater emission probability than the 113 keV γ ray (P_γ = 11% compared to P_γ = 6%) and will be attenuated less by tissue making it more suitable for imaging. The 113 keV peak has a greater number of counts than the 208 keV peak in Figure 7.1 (4.0 x 10^5 net photopeak counts compared to 1.7 x 10^5), however this is due to the detector having increased efficiency at lower γ-ray energies, where photoelectric absorption is more probable. Although the emission probabilities of these γ rays are relatively low, the high fixed administered activity of 7.4 GBq makes imaging possible. The energy resolution at 113 keV was measured to be 6.11% and 3.90% at 208 keV, using GF3. Data were subsequently acquired with a 13 MBq vial of ^{177}Lu for 10 seconds with a clinical Siemens Intevo gamma camera and the resulting spectrum is shown in Figure 7.1. The measured energy resolutions of the 113 and 208 keV peaks are 11.78% and 9.94%, respectively.

7.1.2 ^{111}In

As discussed in Section 2.1.6, ^{111}In is used in the imaging/therapy pair of ^{111}In/^{90}Y. ^{90}Y decays almost exclusively via the emission of a high-energy β-particle with a maximum energy of 2.28 MeV, maximum tissue penetration of 11 mm and half-life $t_{1/2phys}$ of 64 hours [137], making it amenable for a variety of MRT applications. Most commonly, these include radioembolisation, where tiny glass or resin beads filled with ^{90}Y are placed inside the blood vessels that feed a tumour, or in MRT where ^{90}Y labelled pharmaceuticals treat neuroendocrine tumours. Although imaging the bremsstrahlung radiation generated by the interactions of the ^{90}Y β-particles is feasible [138], image quality for ^{90}Y bremsstrahung radiation is limited by overlying tissue attenuation, scattering, variable count rates, wide range of energies and type of collimation employed [137]. Therefore, the most practical method for imaging it to use ^{111}In attached to the same pharmaceutical as a surrogate γ-emitting radionuclide. ^{111}In has a half-life $t_{1/2phys}$ of 67 days, comparable to ^{90}Y, and is assumed to have an identical biodistribution. Typically, approximately 150 MBq of 111In is administered. It decays via the emission of 171 and 245 keV γ rays. A γ-ray spectrum acquired with DEPICT 10 MBq of ^{111}In is shown in Figure 7.2. The energy resolution of the 171 and 245 keV γ rays are 4.70% and 3.77%, respectively. Figure 7.2 also shows the γ-ray spectrum acquired with the clinical gamma camera and 42 MBq of ^{111}In for 10 seconds. The measured energy resolutions of the 171 and 245 keV peaks are 12.24% and 11.50%, respectively.

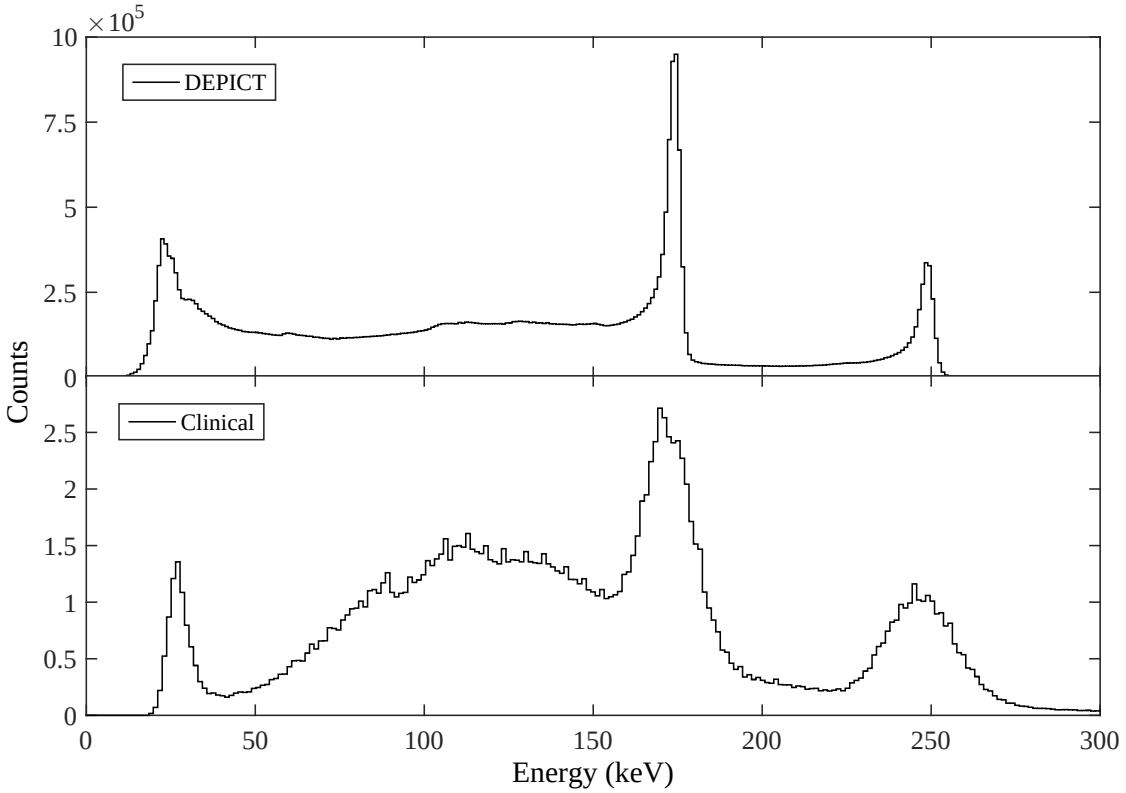

Figure 7.2: ^{111}In γ-ray spectrum acquired with DEPICT and the clinical gamma camera. The γ rays of interest are 171 keV and 245 keV.

7.1.3 ^{223}Ra

Prostate cancer is the most common male cancer in the UK and the second most common male cancer worldwide [139]. ^{223}Ra is an α-particle emitter and is used for treatment of bone metastases from prostate cancer. Although other radionuclides have been used for the same purpose, such as ^{153}Sm and ^{89}Sr, ^{223}Ra is the first α-emitter to also demonstrate proof of survival [140]. ^{223}Ra use has increased by a factor of 100 since being approved by the European Medicines Agency in 2013 [141]. The number of patients with bone metastases treated with radiopharmaceuticals increased by nearly 400% from 2007 to 2015 due to ^{223}Ra [142]. A DEPICT γ-ray spectrum acquired with 2 MBq of ^{223}Ra is shown in Figure 7.3. The γ ray of interest is typically 269 keV with an emission probability of 14%. This is because a clinical gamma camera cannot accurately resolve the low-energy peaks of 145 and 155 keV, as seen in Figure 7.3. In addition, the emission probabilities of the two lower-energy γ rays are reduced ($P_\gamma = 3\%$ and $P_\gamma = 6\%$, respectively) therefore will suffer increased attenuation through the body. However, the 145 and 155 keV photopeaks can be easily resolved with

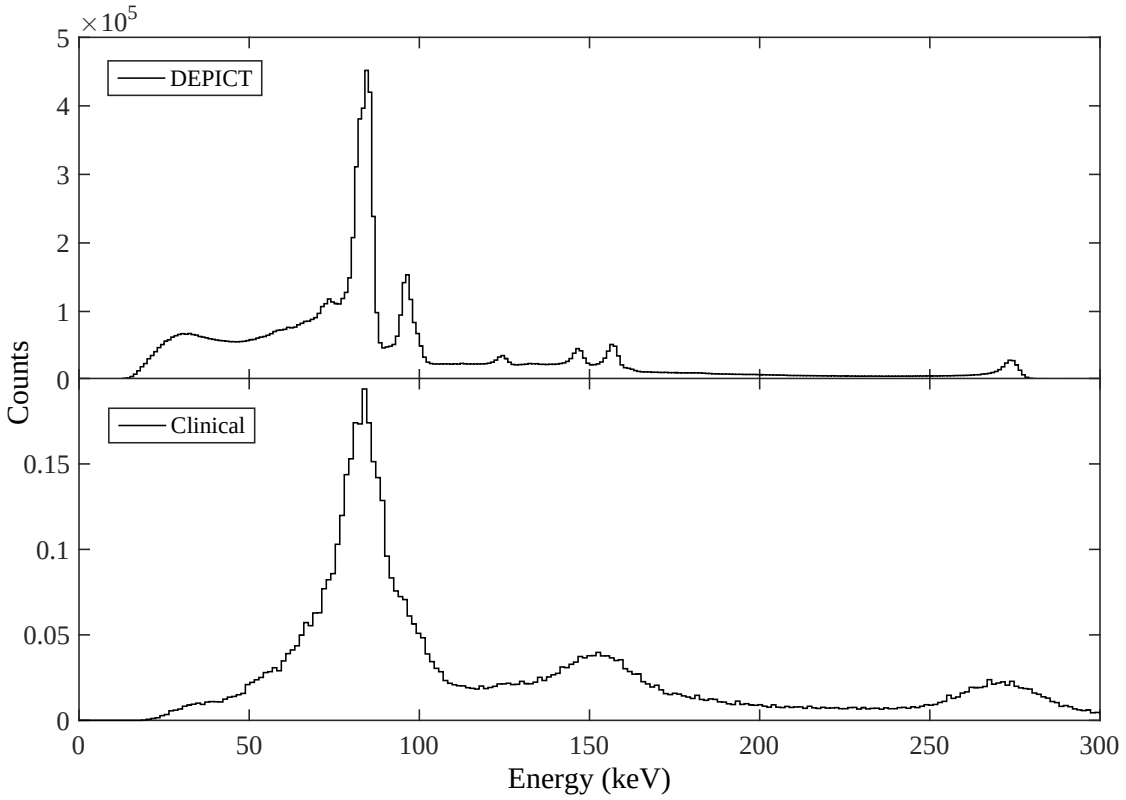

Figure 7.3: ^{223}Ra spectrum acquired with DEPICT and the clinical gamma camera. The γ ray of interest is 269 keV.

DEPICT, giving additional statistics in energy gated images. Attenuation corrections may also be implemented by looking at the relative attenuation of different γ rays from an nuclide if multiple γ-ray energies can be resolved. The energy resolution of the 269 keV γ ray was measured with DEPICT as 3.8%. A vial with 6.2 MBq of ^{223}Ra was placed in front of the clinical gamma camera and the γ-ray spectrum acquired is shown in Figure 7.3. The measured energy resolution of the 269 keV peak is 12.42%.

7.1.4 ^{227}Th

^{227}Th is also an α-particle emitter and used for the treatment of Non-Hodgkin's Lymphoma, ovarian cancer or mesothelioma; a cancer that is almost always caused by exposure to asbestos. ^{227}Th decays to ^{223}Ra with an average α energy of 5.9 MeV and to other short-lived radionuclides in its decay to stable ^{207}Pb. A ^{227}Th γ-ray spectrum was acquired with the DEPICT system and at the time of measurement, the ^{227}Th/^{223}Ra ratio was 2/3 MBq. Therefore, γ-ray emissions from ^{223}Ra also arise in a ^{227}Th γ-ray energy spectrum. A spec-

trum was also acquired with a Siemens clinical gamma camera for comparison. The data for this spectrum were acquired by The Royal Marsden as part of a clinical trial, therefore the exact measurement details are undisclosed. The γ-ray spectrum acquired with DEPICT is of particular interest for dosimetry applications, as the ^{227}Th peaks at 236 keV ($P_\gamma = 13.4\%$) and 256 keV ($P_\gamma = 8.5\%$) are easily resolvable, illustrated in Figure 7.4. This is not the case in a spectrum acquired with a clinical camera spectra, as seen in Figure 7.4. The poor energy resolution causes the 269 keV peak from ^{223}Ra to mask the 256 keV peak, as seen in the inset of Figure 7.4. The 236, 256 and 269 keV photopeaks have energy resolutions of 3.45%, 3.12% and 3.86%, respectively, measured with DEPICT. It was not possible to measure the energy resolution of the photopeaks in the clinical spectra accurately.

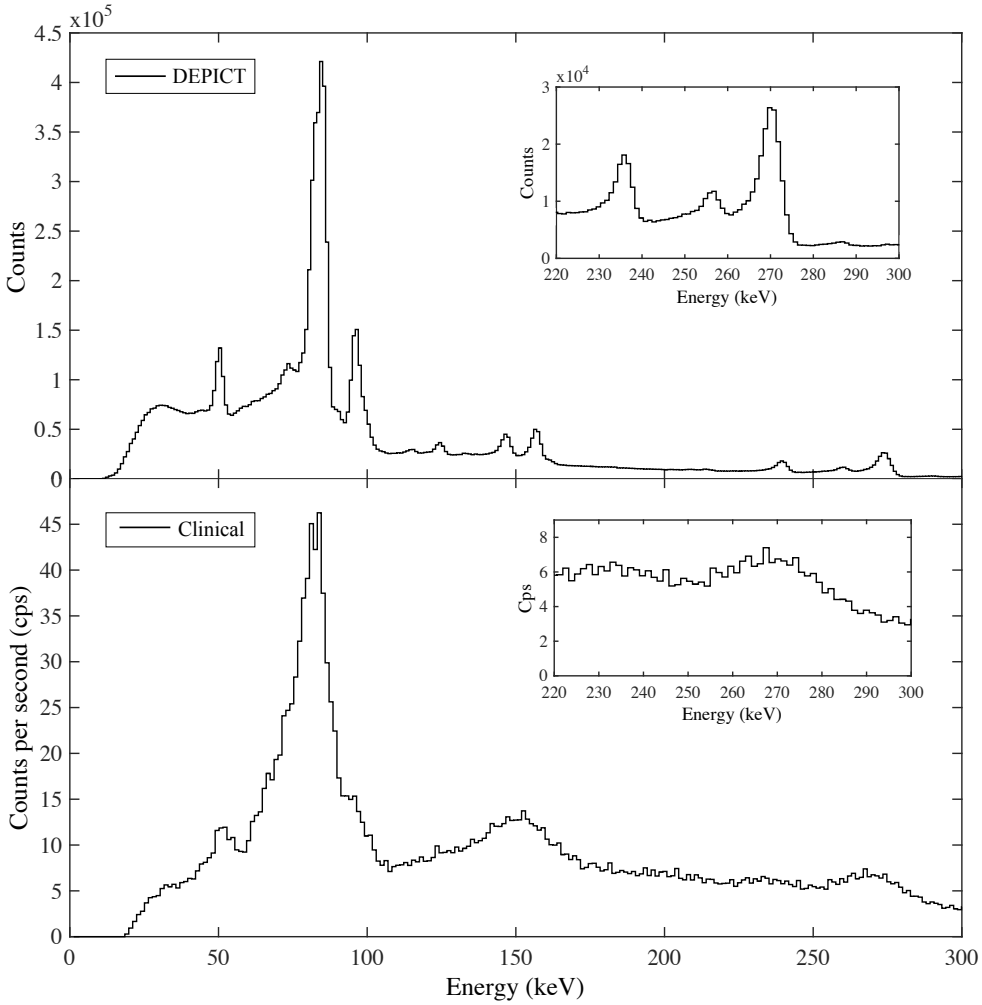

Figure 7.4: ^{227}Th γ-ray spectra acquired with DEPICT and the clinical gamma camera with the data courtesy of The Royal Marsden Hospital. The γ-ray of interest is 236 keV. Insets (a) and (b) expand the spectra between 220 and 300 keV to show the peaks at 236 keV and 256 keV and 269 keV as imaged by DEPICT and Siemens gamma camera.

7.2 Monte-Carlo study of ^{227}Th

Due to the excellent energy resolution of CZT, the photopeaks of each nuclide studied in Section 7.1 are clearly resolvable in the γ-ray spectra acquired with DEPICT in Figures 7.1 - 7.4. However, these spectra were collected without spectral degrading scatter material that would be present during MRT. The radionuclide this would have the greatest impact on is ^{227}Th. The photopeak of interest is 236 keV however down scatter from the two photopeaks with higher energies (256 and 269 keV) may be detected in an energy window set around the 236 keV photopeak, resulting in reduced image contrast and degraded quantitative accuracy. Therefore, to assess the spectral quality in a realistic clinical setting, ^{227}Th γ-ray spectra were simulated using the GAMOS [102] Monte-Carlo toolkit with a ^{227}Th source placed within scattering material. The minimum set of commands required to run a GAMOS simulation are those selecting a geometry, a physics list and a generator, to initialise Geant4 and run N events. The basic GAMOS electromagnetic physics list defines the particles required for the simulation and their physical processes. For this simulation, the physical processes of γ rays and electrons were called. The low-energy physics model based on the Livermore Evaluated Data Libraries [143, 144, 145] were selected. These libraries provides atomic data for elements Z = 1 to 100, over the energy range 10 eV to 100 GeV which is appropriate for medical simulations. The GAMOS generator provides several time, energy, position and direction distributions that the user may combine to achieve their desired outcome. The geometry includes the definition of materials and describes the position of the particle source and simulated detector in space. The generation of particles and the geometry are described below.

A distributed cylindrical source of radius 2 cm and length Z of 4 cm, with the same activity ratio as the experimental ^{227}Th/^{223}Ra spectrum collected with DEPICT in Figure 7.4, was simulated. The distributed source, shown by the white cylinder in Figure 7.5, was placed inside a volume in which the volume material had the attenuating properties of soft tissue, defined by the Tissue Substitutes in Radiation Dosimetry and Measurement (Report 44) [146]. This simulated a simplified MRT situation in which a distributed source of activity is contained with soft tissue in the body. To extract information from a GAMOS simulation, a sensitive detector that simulates the signals (hits) in a device must be created. It creates

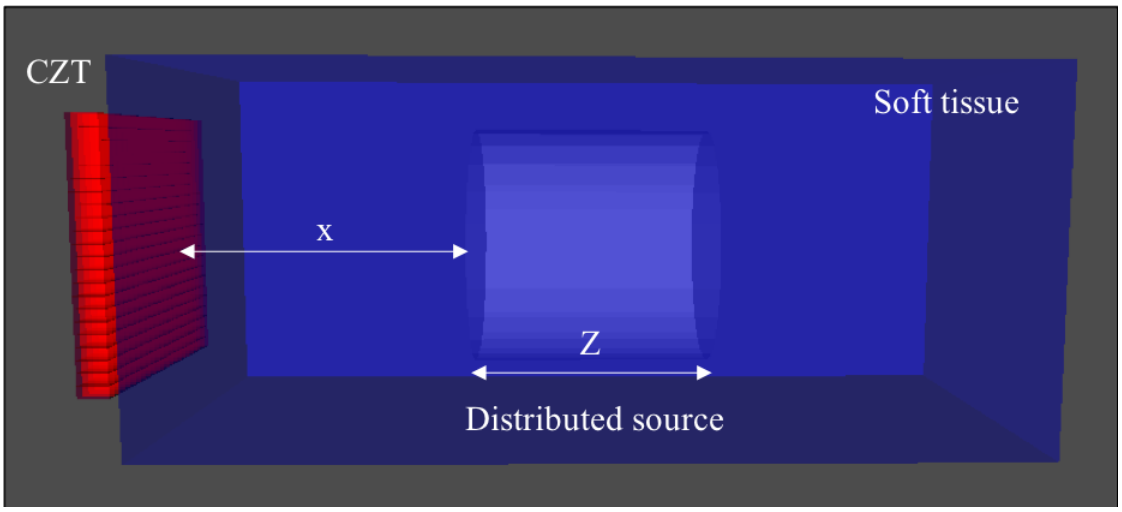

Figure 7.5: Simulated GAMOS geometry viewed using view3Dscene .

hits each time a particle track transverses a sensitive volume and loses energy. Sensitive detectors can be attributed to a user-defined volume to mimic the response of the sensitive part of a real detector. A 44 x 44 x 5 mm volume segmented into 484 2 x 2 x 5 mm voxels to replicate the DEPICT CZT detector was therefore created, shown in red in Figure 7.5. The height and width of the soft tissue volume, shown in blue, were both set as 6 cm to completely cover the face of the CZT detector. The depth was changed in order to vary the thickness of soft tissue x between the CZT detector and the edge of the distributed source volume nearest to the detector. as illustrated in Figure 7.5. For comparison, the simulation was run with x set to 5 cm and 10 cm and also without the soft tissue surrounding the source.

There are a number of experimental detector effects which can be accounted for with user commands in GAMOS, including energy resolution and minimum hit energy (threshold). The energy resolution of the DEPICT CZT detector was therefore recreated in the simulated CZT detector, along with the energy threshold that was set in experimental data collection. The ability to smear the energy of the hits with a Gaussian distribution is achieved by:

$$/gamos/setParamSD : EnergyResol : Absorber \quad VALUE1$$

In addition, a second term can be applied for energy-independent factors attributed to instrumental effects such as noise by:

$$/gamos/setParamSD : EnergyResolInstr : Absorber \quad VALUE2$$

The extent of Gaussian smearing is dictated by the width parameter of a Gaussian distribution, the standard deviation σ, and in GAMOS is the value of *VALUE1*. The parameter σ is related to the FWHM through the relation $FWHM = 2.35\sigma$ [47]. Therefore, to calculate the result of *VALUE1* required to accurately simulate the DEPICT CZT energy resolution, the FWHM of various nuclides with γ-ray energies 59 – 364.5 keV were measured and a plot of FWHM versus energy was produced. A straight line was fit to the data with the equation $y = mx + c$. The gradient m of the graph was then divided by 2.35 to obtain the value of σ as $FWHM = 2.35\sigma$, which was calculated to be 0.0097. *VALUE2* corresponds to the intercept of the FWHM versus energy graph, as it is the contribution to the energy resolution that is independent of γ-ray energy. This was calculated as 0.0019. In GAMOS, charge transport properties cannot be simulated, therefore the low-energy photopeak tailing characteristic of CZT detectors is not reproduced.

Simulations with no scatter material and 5 cm and 10 cm of scatter material were run with 10 million events each, where the number of events is the number of initial particles. Each particle will then collide and generate a set of secondary particles. ROOT [147], a scientific toolkit developed by CERN that allows data processing, statistical analysis and visualisation, was used to display the reconstructed hits as a histogram. Figure 7.6 shows the three histograms acquired, with no scatter and 5 and 10 cm of scatter material. Figure 7.7 displays the events from Figure 7.6 that have an energy from 220 – 300 keV. This energy regions contains the 236, 256 and 269 keV γ rays that are of interest in ^{227}Th imaging.

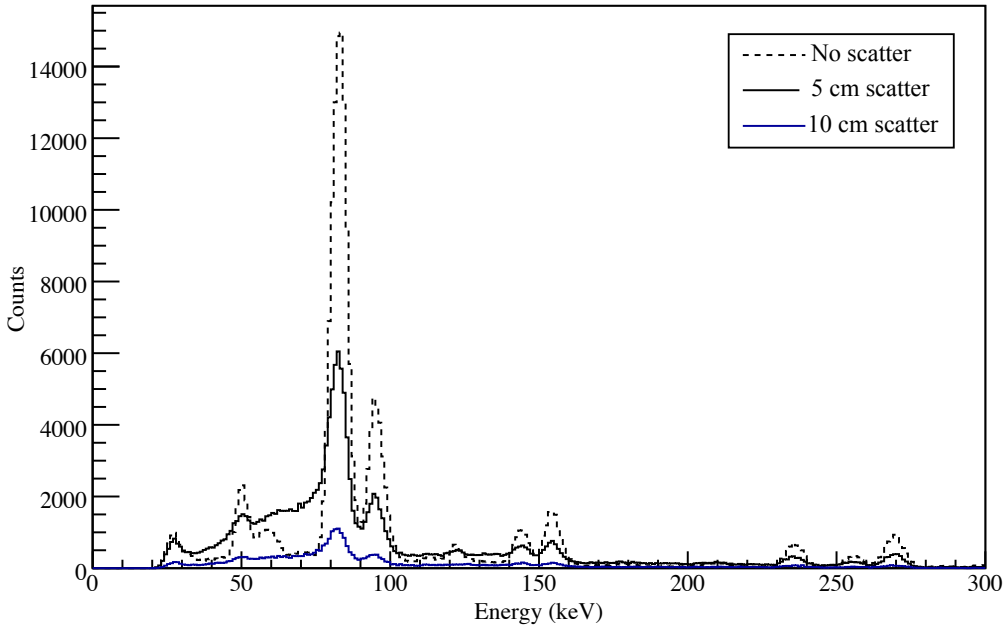

Figure 7.6: ^{227}Th energy spectra simulated with no scatter material (black dashed line), 5 cm (solid black line) and 10 cm (solid blue line) of scatter material between the source and the detector.

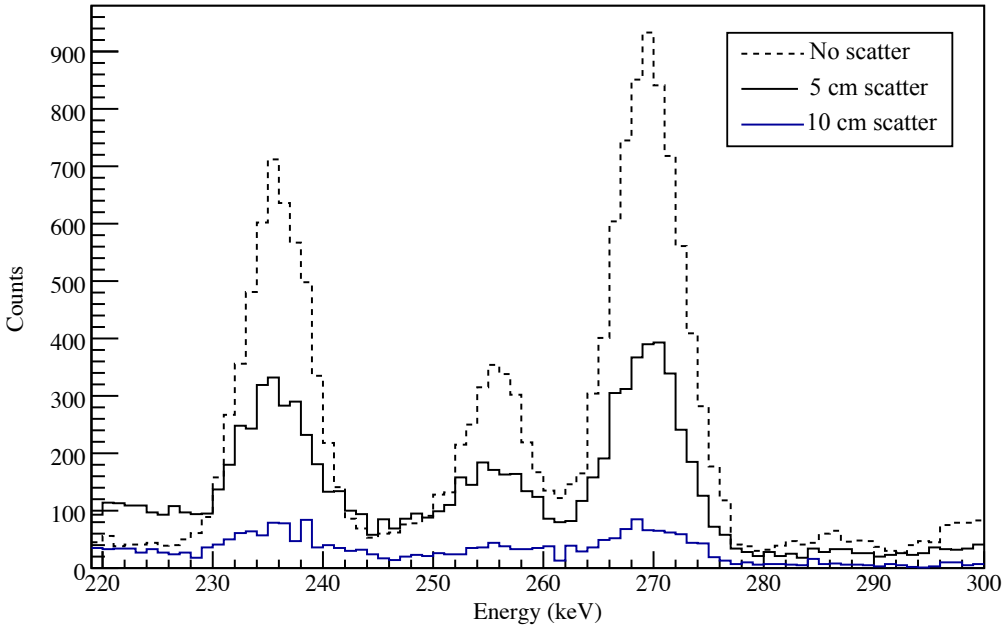

Figure 7.7: Shown is the data from Figure 7.6 but only events with energy between 220 and 300 keV.

Figure 7.6 shows three ^{227}Th spectra, with decreasing counts as the thickness of scatter material increases. The position and width of the photopeaks replicate those seen in the experimentally collected ^{227}Th spectrum in Figure 7.4a. Following a simulation, GAMOS can output information about the interactions of 'original' γ rays in the sensitive detector.

For this energy range, only photoelectric absorption and Compton scattering are possible. Table 7.1 highlights the number of original γ rays reaching the sensitive detector *N γ in SD*, the number of original γ rays undergoing photoelectric interactions in the sensitive detector *N PE* and the number of original γ rays with Compton interactions *N Comp* for the histograms seen in Figure 7.6 with no scatter material, 5 cm and 10 cm.

	No scatter (x10^5)	5 cm scatter (x10^5)	10 cm scatter (x10^5)
N γ in SD	3.94	2.04	0.43
N PE	3.23 (81.85%)	1.60 (78.11%)	0.33 (76.20%)
N Comp	0.29 (7.23%)	0.19 (9.42%)	0.04 (9.82%)

Table 7.1: Comparison of photopeak to Compton scatter events. The percentage in brackets shows the relative photoelectric or Compton scattered events compared to the total γ-ray events in the sensitive detector.

As the thickness of scatter material increases, the number of photoelectric events decreases, while the number of Compton events increases, as expected. The peak-to-Compton ratio, defined here as the ratio of *N PE / N Comp*, is 11.32 for no scatter, 8.29 for 5 cm of scatter and 7.76 for 10 cm of scatter. A reduced peak-to-Compton ratio will cause a reduction in contrast within a medical image, increasing the difficulty of performing dosimetry. It is expected the presence of a collimator would induce further scatter. The three photopeaks of interest are still resolvable, and due to the excellent energy resolution of DEPICT it is possible to energy gate individual emissions to accurately suppress scattered events for activity quantification.

7.3 Multi-nuclide Imaging

^{99m}Tc and ^{123}I are two common medical imaging nuclides that emit γ rays of very similar energies; 140.5 keV and 159 keV, respectively. Although not used for therapeutic purposes, these nuclides and can be used simultaneously to study two physiological processes to elucidate the disease status as part of an MRT treatment plan [148]. Thus, experimental planar images were acquired with ^{99m}Tc and ^{123}I for the investigation of multi-nuclide imaging with DEPICT. A collimator optimised for low-energy γ rays is required for imaging these nuclides. Therefore, a prototype low-energy parallel-hole collimator, manufactured by Kromek, was coupled to the DEPICT CZT detector. The lead collimator was designed with hexagonal

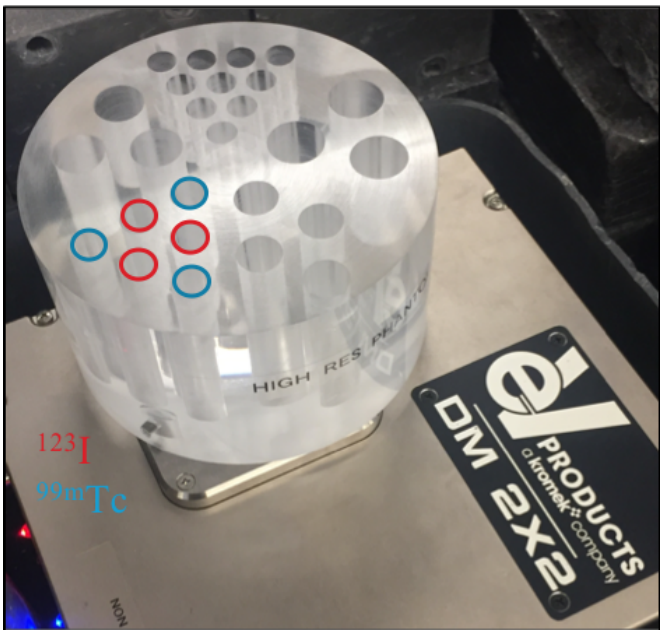

Figure 7.8: A photograph of the perspex phantom placed on top of the low-energy collimator. Red circles show the position of the three ^{123}I vials; blue circles show the position of the ^{99m}Tc vials. In the photograph the phantom is offset from the position in which it was placed during data collection in order to be able to view the low-energy collimator.

holes of length $L = 23$ mm, hole diameter $d = 1.2$ mm and septa thickness $t = 0.2$ mm. Unlike the DEPICT collimator, the low-energy collimator was not designed to be pixel matched to the CZT detector. Data were acquired simultaneously with six 8 mm inner diameter vials of length 4.5 cm; three filled with aqueous ^{123}I ($t_{1/2phys} = 13.22$ hours) and three with ^{99m}Tc ($t_{1/2phys} = 6.01$ hours). The ^{123}I vials each contained an activity of ∼300 kBq, with ∼200 kBq in each ^{99m}Tc vial. The activities of the ^{123}I and ^{99m}Tc sources were calibrated at The Royal Liverpool University Hospital on the morning of the measurement, and uncertainties arise due to the calibration and dispensing methods. The vials were placed into a perspex phantom in the orientation shown in Figure 7.8 and data acquired for 30 minutes.

The associated sum spectra acquired with the six vials simultaneously is shown in Figure 7.9a. The two peaks at approximately 75 and 85 keV correspond to lead x-rays produced in fluorescence from the collimator. The peaks at 140.5 and 159 keV are the photopeak events from the ^{99m}Tc and ^{123}I sources, respectively. The black dashed lines encompass γ-ray events with energy between 130 – 175 keV and indicate the energy gate applied to the the pixel map shown in Figure 7.9b. Six areas of high counts are evident in the pixel map corresponding to

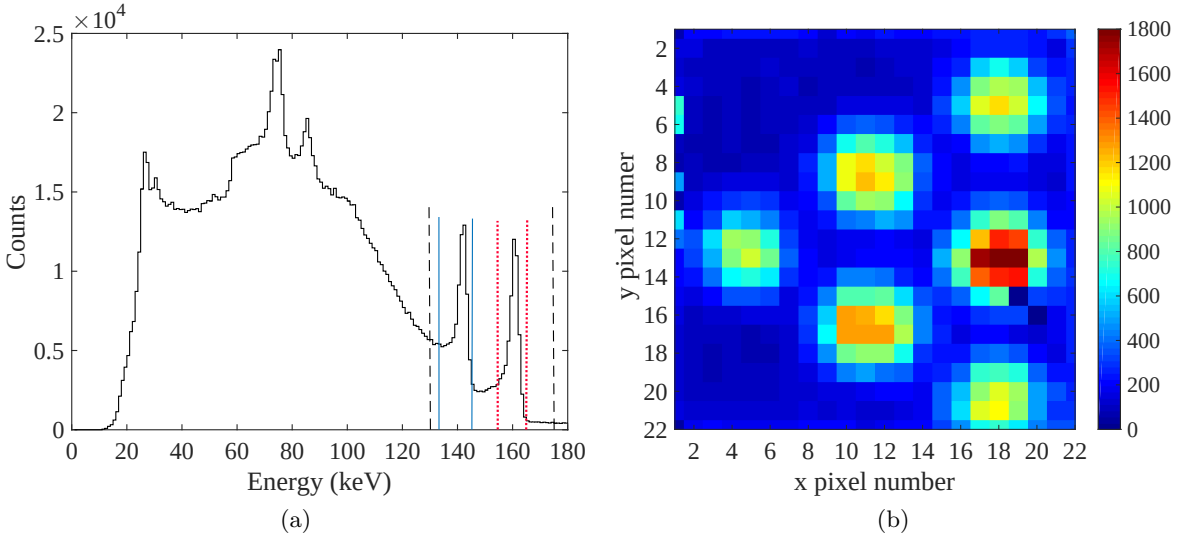

Figure 7.9: (a) Sum spectra acquired with three ^{123}I and three ^{99m}Tc vials. The dashed black lines encompass both photopeaks, the blue solid lines and the red dotted lines encompass the ^{99m}Tc photopeak and the ^{123}I photopeak, respectively and (b) the energy gated pixel map obtained, with γ-ray events with energy 130 – 175 keV.

the six vials. The hot spots at the known ^{123}I vial positions have increased counts compared to the hot spots for the ^{99m}Tc vials. This is consistent with the increased activity in the ^{123}I vials, although it appears that the vials did not contain exactly equal activities. As the energy gate applied encompasses the photopeak energy of each nuclide, it is not possible in this image to distinguish the ^{99m}Tc and ^{123}I vials from one another.

Due to the excellent energy resolution of the CZT detector, it is possible to apply very narrow energy windows around the individual photopeaks. An energy window around 5% was applied around each photopeak, corresponding to 137 – 144 keV around the 140.5 keV ^{99m}Tc photopeak and 155 – 163 keV around the 159 keV ^{123}I photopeak. These energy windows are shown in Figure 7.9a with the blue solid line showing the ^{99m}Tc energy window, and red dotted lines indicating the ^{123}I window. Two energy gated pixel maps corresponding to the data encompassed in each energy window are shown in Figures 7.10a and 7.10b. With the energy gate applied between 137 – 144 keV in Figure 7.10a, three regions of higher intensity are visible at the known ^{99m}Tc vial positions. There are three areas of approximately 150 counts visible in the ^{99m}Tc gated pixel map where the ^{123}I vials are known to be. Although the energy gate is applied around the ^{99m}Tc photopeak, it sits on the Compton background of ^{123}I. Therefore some events in the ^{99m}Tc pixel map will arise from ^{123}I emissions. The triple

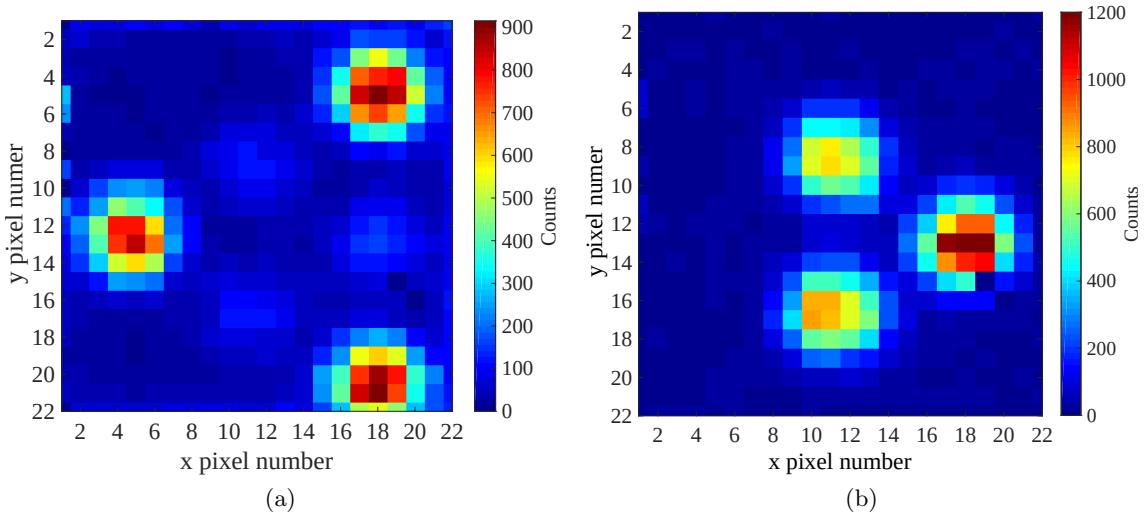

Figure 7.10: Energy gated pixel maps showing vials containing (a) ^{99m}Tc only and (b) ^{123}I only.

energy window scatter correction method could be applied to remove these scattered events from the image [149]. Figure 7.10b shows three high count areas at the known position of the ^{123}I vial positions in the pixel map created with γ-ray events between 155 – 163 keV. These images show that it is possible to apply an energy gate around one photopeak and be able to observe the vials with that energy only and prove multi-nuclide imaging with radionuclides of similar γ-ray energy is achieveable with the DEPICT system. This technique is not feasible with a NaI(Tl) detector typically used in clinical gamma cameras. For comparison, Figure 7.11 shows a γ-ray spectrum obtained from imaging two 16.4 mm diameter vials containing 0.11 MBq ^{99m}Tc and 0.55 MBq ^{123}I [150]. The photopeaks are not easily resolvable, and complex corrections would have to be applied to deconvolve an image acquired with ^{99m}Tc and ^{123}I with a clinical gamma camera.

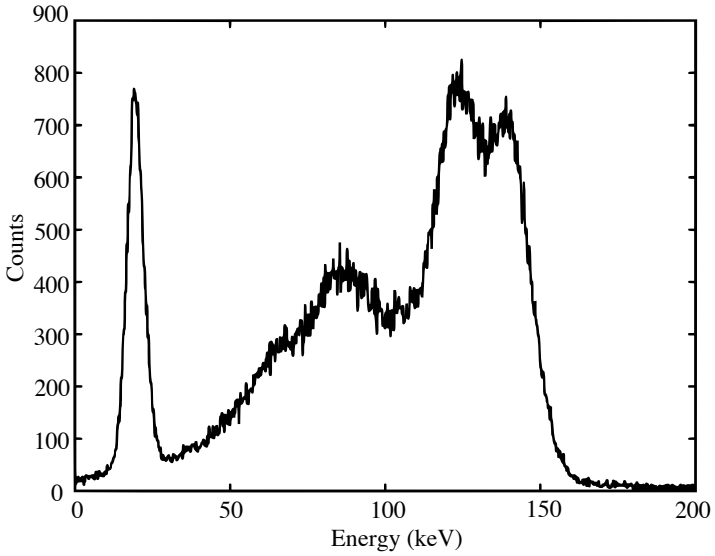

Figure 7.11: ^{123}I and ^{99m}Tc energy spectrum acquired with NaI(Tl) detector. Data courtesy of A. Patel [150].

7.3.1 Energy Optimised Collimator

Sections 7.1.1 - 7.1.4 show the DEPICT CZT detector can be used to acquire high quality spectroscopic data for a variety of medical radionuclides. In order to acquire medical images with these nuclides, a collimator optimised for the energy of their emitted γ rays is required. The choice of collimator is a trade-off between high sensitivity, good signal-to-noise ratio, spatial resolution and septal penetration. It was not within the remit of this thesis to produce multiple collimators so as a preliminary study to allow recommendations for future work, experimental data were acquired using existing collimators with other designs later studied using GAMOS. ^{177}Lu is classed as a medium-energy γ-emitter. Medium-energy collimators are therefore preferable over low-energy collimators for ^{177}Lu imaging because of the lower septal penetration of the emitted γ rays. In addition, although high-energy collimators have thicker septa than medium-energy collimators that would further reduce septal penetration, they have inferior spatial resolution due to larger collimator holes. In order to study the effects that arise due to imaging with an unoptimised collimator, data were acquired with a 22 mm inner diameter vial of 108 MBq ^{177}Lu, with both the low-energy prototype Kromek collimator described in Section 7.3 and the DEPICT high-energy collimator. Data were acquired for 15 minutes with the low-energy collimator and 20 minutes with the high-energy collimator and an energy window of 200 – 220 keV was applied. Figure 7.12a and Figure 7.12b show the energy gated pixel maps acquired with the low-energy and high-energy collimators,

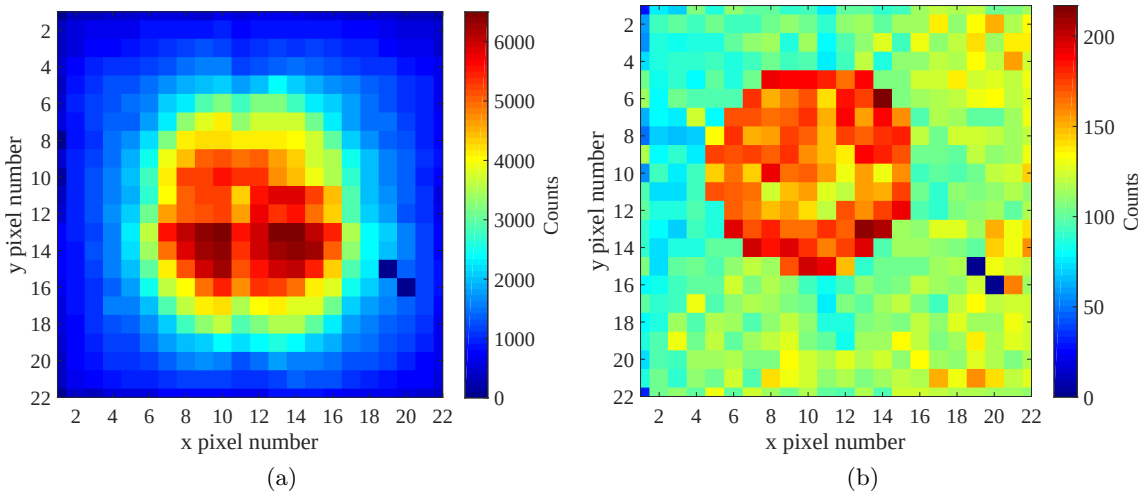

Figure 7.12: ^{177}Lu vial positioned on top of (a) low-energy Kromek collimator and (b) the custom-designed high-energy collimator. Both images are energy gated on the 208 keV peak with an energy window of 200 – 220 keV.

respectively. Figure 7.12a has an area of 5000 – 6000 counts per pixel towards the centre of the image, with the counts decreasing with increasing radial distance from the centre. Ideally, a distinct circular pattern would be visible at the position of the vial with the known diameter of 22 mm, however there is blurring of the vial edges caused by septal penetration. The exact position or edges of the vial cannot be determined accurately from this image. Figure 7.12b shows a distinct circular region of ∼175 counts per pixel, corresponding to a direct projection of the vial that is 11 pixels in diameter. Although typically high-energy collimators have larger holes to increase the sensitivity, the DEPICT high-energy collimator was developed with small holes for decreased sensitivity (due to imaging high activities) and high resolution. Therefore a clear outline of the base of the vial is seen in the image, but with highly reduced counts compared to the low-energy collimator. Due to difficulties that occurred in the acquisition of the high-energy collimator data, the collimator was not positioned in its ideal position above the detector. This error in positioning caused a large amount of scatter, manifesting as a high (100 count) background in the pixel map. It is expected that the background counts would be would be dramatically reduced if the collimator was positioned correctly. Due to the cost and availability of the radionuclide, it was not possible to repeat this experiment.

A DEPICT imaging system for employment across the energy range of the radionuclides discussed in this chapter requires a custom-designed medium-energy collimator. GAMOS was therefore used for the preliminary design of a medium-energy collimator. Firstly, to validate the GAMOS geometry, simulations of the experimental setup used for acquiring Figure 7.12a and 7.12b were undertaken, and pixel maps compared. Figure 7.13a shows the simulated low-energy collimator with 23 mm length and 1.2 diameter holes and Figure 7.13b shows that of the high-energy collimator with 55 mm length and 0.6 mm diameter holes. In both figures, the simulated pixelated CZT detector is shown in red, the collimator holes are white and the edge of the collimator that is physically positioned above the detector casing in shown in blue. The white cylinder is a simulated glass vial, with a ^{177}Lu source distributed within the volume. There is a 2.1 mm gap between the base of the collimator holes and the CZT detector face. In Figures 5.1a and 5.1b, 50 γ-ray events were simulated and their paths are illustrated by the green lines.

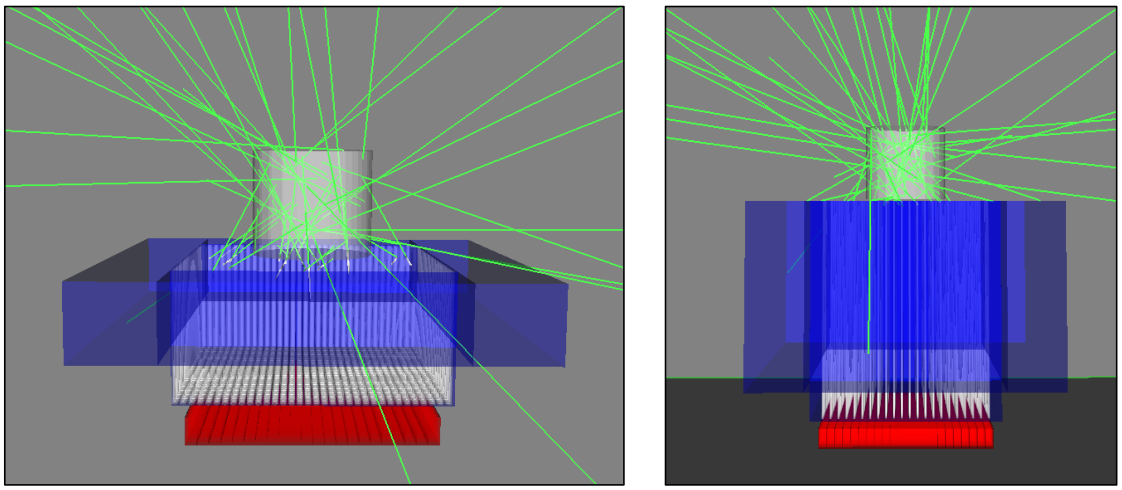

(a) (b)

Figure 7.13: Images showing the geometry of the GAMOS simulations of (a) low-energy Kromek prototype collimator and (b) custom-designed DEPICT high-energy collimator. The coloured volumes are defined in the text.

The simulations to acquire data for validation ran 100 million events for the low-energy collimator and 2100 million events for the high-energy collimator. ^{177}Lu 208 keV γ rays were simulated for comparison to the experimentally acquired pixel maps shown in Figures 7.12a and Figure 7.12b, as only events arising from photoelectric absorption were included. Figures 7.14a and 7.14b show the simulated pixel maps that were binned into 22 bins across 44 mm

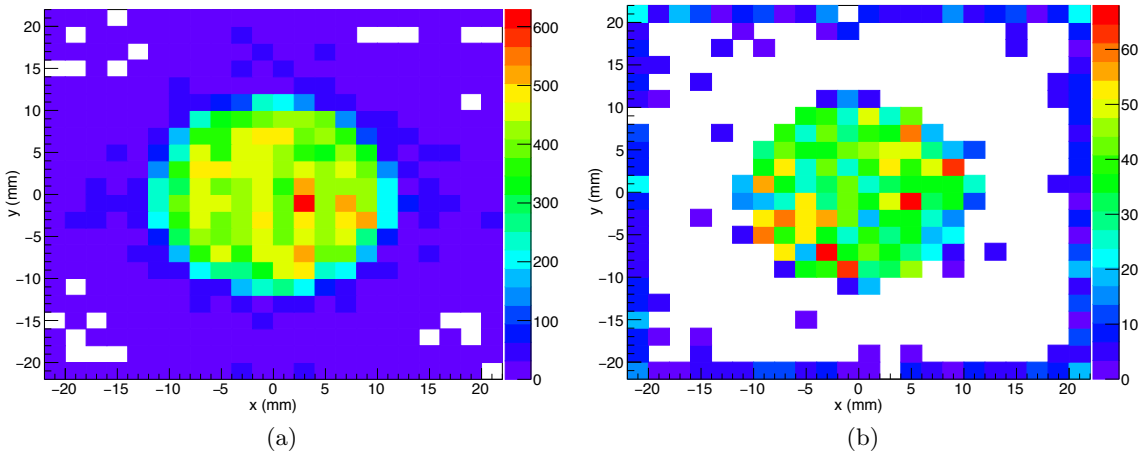

Figure 7.14: Plots showing GAMOS simulated pixels maps of the (a) low-energy and (b) high-energy collimators and ^{177}Lu vial.

in the x- and y-directions (-20 to 20 mm) to simulate the CZT pixels. Figure 7.14a shows an area of ∼400 counts in the centre of the image, corresponding the simulated vial, with a background ∼15 counts. The large amount of septal penetration seen in Figure 7.12a is not well replicated as for simplicity, the low-energy collimator was simulated with circular holes rather than hexagonal. However, there are a small number of pixels with approximately 50 counts surrounding the hot spot due to a small amount of septal penetration. Transmission (%) is defined as the number of original γ rays that interacted within the sensitive detector $N\,\gamma$ *in SD* divided by the number of original simulated events, multiplied by 100. For the simulated low-energy collimator $N\,\gamma$ *in SD* was 17578, giving a transmission of 1.76 x 10^{-2} %. Figure 7.14b shows the pixel map acquired from simulating the DEPICT high-energy collimator. The collimator was designed to have a very low efficiency for imaging the high-activities in MRT therefore a reduced transmission compared to the low-energy collimator would be expected. For the high-energy collimator, $N\,\gamma$ *in SD* was 1420, giving a transmission of 6.76 x 10^{-5} %. The maximum possible number of GAMOS simulated events were run, however due to the extremely low transmission, a pixel map that would be representative of an experimentally acquired pixel map was not produced. The centre pixels of the image that corresponding to the vial position, have approximately 40 counts, with mostly zero counts in surrounding pixels and a small number ∼5 in the edge pixels. The relative differences however, in pixel counts and calculated transmission values between the low-energy collimator and high-energy collimator simulated data were as expected.

As the simulated images adequately represent the experimental pixel maps, a medium-energy collimator could be designed by modifying the high-energy, pixel matched tungsten collimator geometry. Although a higher activity of ^{177}Lu is typically administered in MRT compared to that of ^{131}I (7.4 GBq to 3.7 GBq), the γ rays emitted from ^{177}Lu are lower in both energy and intensity. The emission probability of 364.5 keV γ rays from ^{131}I is 82%, compared to 11% for 208 keV γ rays from ^{177}Lu. Additionally, the linear attenuation coefficient of soft tissue is 0.13 cm^{-1} at 208 keV compared to 0.11 cm^{-1} at 364% [54]. Equation 3.5 shows that for soft tissue of thickness 5 cm, 52% of 208 keV γ rays would pass through the material compared to 58% for 364.5 keV γ rays. If a 208 keV γ ray is emitted for a given disintegration, it is more likely to be attenuated, therefore dead time effects are less likely to be as severe and the collimator does not have to be as low-efficiency as the high-energy DEPICT collimator. Typically the hole diameter and length for a medium-energy collimator are greater than those for a low-energy collimator and less than those of a high-energy collimator. However, as the DEPICT high-energy collimator is designed for low-efficiency, high-resolution measurements to improve image quality and improve count rate saturation, it has a much smaller hole diameter than that of the low-energy collimator. To facilitate high-resolution imaging with increased efficiency, collimator geometries were simulated with the hole diameter ranging from 0.6 (low-energy collimator hole diameter) to 1.2 mm (high-energy collimator hole diameter), in 0.1 mm increments. The hole length was set at 40 mm for each hole diameter. The length of the holes are required to be longer than those of a low-energy collimator, to reduce septal penetration, but shorter than those of the high-energy collimator to allow more γ rays to reach the detector. Therefore, the hole length was varied from 25 – 50 mm, with the hole diameter set at 1 mm. For each hole diameter and hole length, 50 million events were ran. Figures 7.15a and 7.15b show the measured transmission as a function of diameter and length, respectively. The transmission is also known as collimator efficiency g and is defined by

$$g \approx K^2 \left(\frac{d}{L}\right)^2 \left[\frac{d^2}{(d+t)^2}\right], \tag{7.1}$$

where K is a constant that depends on hole shape ($\sim$0.24 for round holes) and d, L, and t are hole diameter, length and septal thickness. Therefore, Equation 7.1 shows the transmission is proportional to d^2, assuming $t = 0$, and also to $1/L^2$. This relationship is replicated in the data shown in Figures 7.15a and 7.15b.

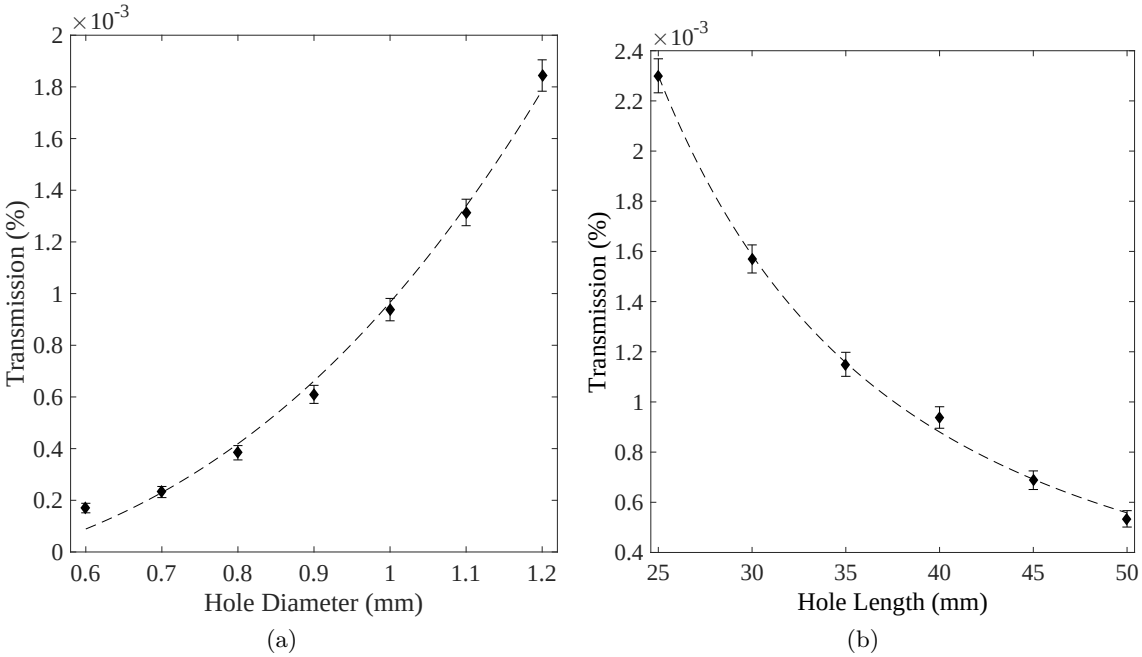

Figure 7.15: Plots showing the transmission (%) of events as a function of (a) hole diameter d and (b) hole length L. For (a) the length was set at 40 mm and for (b) the diameter was set at 1 mm.

For this rudimentary medium-energy collimator design, 40 mm was chosen as the hole length as this was the mid-length between the low- and high-energy collimators. This length is also comparable to the length of commercial medium-energy collimators at 40.64 mm. The hole diameter of 1 mm was chosen, giving both increased sensitivity and high-resolution imaging. A small amount of septal penetration is often accepted in gamma cameras; usually 5%. For septal penetration of less than 5%, the septal thickness t, hole diameter d and hole length l are related by

$$t \geq \frac{6d/\mu}{l - (3/\mu)}, \tag{7.2}$$

where μ is the linear attenuation coefficient of the septal material [55]. For the chosen hole length l of 40 mm, hole diameter d of 1 mm and linear attenuation coefficient μ for tungsten of 12.93 cm^{-1} at 208 keV, the septal thickness required for less than 5% setpal penetration is $\geq$ 0.01 mm, which is far surpassed in this design with a septal thickness of 1 mm. As the DEPICT collimator is pixel matched, there is the constraint that $d + t$ must equal the pixel pitch of 2 mm. The expected system spatial resolution R_{sys} can be determined using Equations 3.3 and 3.4 to calculate the values of collimator resolution R_{coll} and R_{sys}. R_{coll} is 1.25 mm for a source-to-collimator of 10 cm giving a value for system spatial resolution R_{sys}

of 2.36 mm. Although this is degraded compared to the 2 mm resolution of the DEPICT high-energy collimator, it is much improved on the system spatial resolution of a clinical gamma camera coupled to a medium-energy collimator of 12.5 mm at 10 cm. Figure 7.16 shows a simulated pixel map acquired with the medium-energy collimator with 2100 million simulated events.

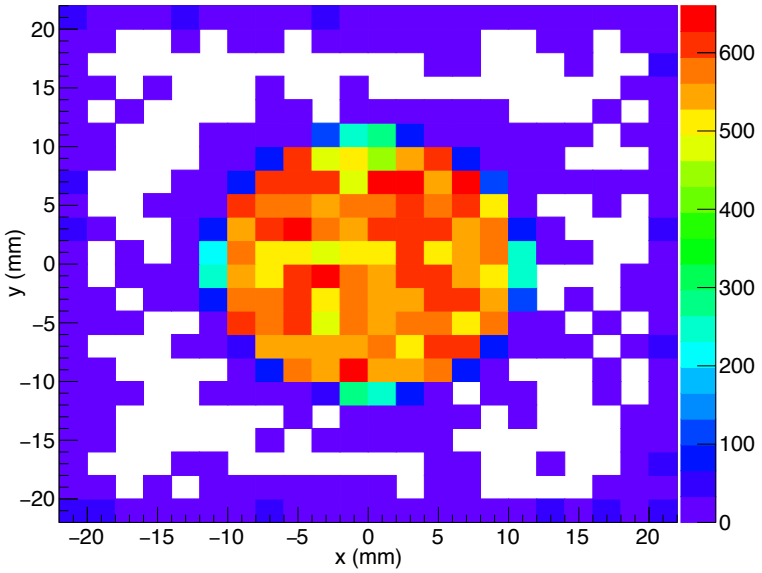

Figure 7.16: Medium-energy collimator simulation with hole length $L = 40$ mm and hole rdiameter $d = 1$ mm.

The simulated pixel map shows a high ∼550 count area towards the centre of the of the image with approximately 20 counts in the background pixels. The simulated transmission of the medium-energy collimator was calculated as 9.10 x 10^{-4}, which is intermediate to the transmissions calculated for the low- and high-energy collimators, as expected. From the image, the diameter of the vial is calculated as 12 mm, including the pixels at the edge of the high count area of approximately 200 counts, however the spatial resolution is expected to be degraded compared to the high-energy collimator due to the shorter and larger diameter holes.

The design of a collimator is complex as hole length and diameter are not totally independent of one another, therefore it is not possible to ascertain their effects on an image individually. As the DEPICT CZT has a very small FOV, it is likely that future work will involved a scaled up version of the detector used in this thesis. Therefore, the design of the medium-energy collimator may change as detector is scaled up in size. In addition, the sensitivity of the

system will depend on the organ being imaged, as deeper-seated organs will induce more scatter and attenuation

7.4 Summary of Further Clinical Applicability of DEPICT

In this chapter, the feasibility of multi-nuclide imaging with DEPICT has been investigated as simultaneous imaging of ^{123}I and ^{99m}Tc can be used in brain and cardiac imaging [151, 152]. The excellent energy resolution of CZT was found to successfully permit simultaneous imaging of these two nuclides. Energy spectra of the γ rays emitted from emerging radionuclides in the field of MRT were acquired with the DEPICT CZT detector. These were ^{177}Lu, ^{111}In, ^{223}Ra and ^{227}Th. A comparison of ^{227}Th γ-ray spectra acquired with and without scatter material was undertaken with simulations using GAMOS. The peak-to-Compton ratio decreased with increasing scatter material as expected, but the peaks of interest were still resolvable. Medical imaging of the emerging radionuclides that emit medium-energy γ rays requires a medium-energy collimator. GAMOS was used for the preliminary design of a DEPICT medium-energy collimator to facilitate this. The final design was circular holes of length $l = 40$ mm, diameter $d = 1$ mm and septal thickness t of 1 mm.

Chapter 8

Conclusions

The methods used to develop and evaluate the DEPICT system for imaging the γ rays emitted following MRT have been discussed in this thesis. The DEPICT project was based at the University of Liverpool with collaborators from The Royal Liverpool University Hospital, The Royal Marsden Hospital and Kromek. Data were acquired across both hospital sites to allow measurements with high activity medical radionuclides in order to provide realistic clinical test scenarios. The project focussed on radioiodine treatment of thyroid cancer and benign diseases, such as hyperthyroidism.

The motivation for this project was the need for the routine clinical implementation of dosimetry in MRT. Accurate calculation of the absorbed dose will enable therapies to be tailored to give maximum tumour absorbed dose, whilst minimising the dose to organs at risk. In EBRT, the process of patient-specific dosimetry has been standard practise for years providing individualised radiotherapy treatments to patients with accurately delivered absorbed tumour doses. In MRT, it is rare for a patient to have their absorbed doses calculated and therapy is based on administering standard amounts of activity. Failing to calculate dose leads to some patients receiving more radiation than is necessary to treat their disease, and some receiving a sub-optimal dose. The EU Directive 2013/59/Euratom of 5 December 2013 required that by February 2018 'all medical exposures of patients for radiotherapy purposes, exposures of target volumes shall be individually planned and their delivery appropriately verified'. However, most centres still employ a 'one-size-fits-all' approach rather than calculating individualised internal dose values, even though increasing evidence shows that treatment outcomes correlate with the absorbed doses delivered to tumours and healthy organs [153]. In addition to the patient benefit of potentially increased rates of successful cancer treatment,

progressing from generic treatments to the routine application of patient-specific dosimetry will save NHS funds by MRT becoming a more effective and efficient treatment modality. The cost savings become even more important when emerging radiopharmaceuticals are considered as the cost of these for treatment is significant.

Limitations in current clinical gamma cameras hinder the progression of dosimetry in MRT due to uncertainties that arise from outlining organs of interest from poor quality images. To overcome issues faced in imaging, such as limited energy resolution and spatial resolution, a pixelated CZT detector was chosen for use in the DEPICT project. CZT is a room temperature semiconductor detector that is known to have superior energy resolution and excellent spatial resolution, if developed with small pixels. In the work of this thesis, a DMatrix CZT detector manufactured by eV Products [92] was optimised for MRT applications that require good energy resolution and high-throughput of γ rays, given the high activities administered. A custom-designed high-energy parallel-hole collimator was developed to couple to the CZT detector to create a γ-ray imaging system. The collimator had a high resolution and low efficiency and was found not to enter dead time when imaging therapeutic activity levels (at least 3.5 GBq). The measured energy resolution of 3% at 364.5 keV and system spatial resolution at 10 cm of 2 mm are far superior to the same parameters in scintillator gamma cameras. These are 9 – 10% and 13.4 mm for energy resolution and system spatial resolution with a high-energy collimator, respectively. Improved energy resolution allows narrow energy windows to be set around a photopeak reducing unwanted scatter contributions within an image, which would otherwise degrade the signal-to-noise. The CZT detectors are also coupled to custom ASICs to process and readout the signals, which reduce the size and cost of readout electronics compared to clinical gamma cameras that require bulky PMTs.

Images produced using the DEPICT system for data acquired with ^{131}I and a variety of clinical phantoms have been shown to be both qualitatively and quantitatively superior when compared to a Siemens Intevo gamma camera. The DEPICT system could easily resolve vials of 10 mm diameter, whereas the large collimator holes of the Siemens system degraded the image. Cold spots in a thyroid phantom that were visible in the DEPICT image were not seen in an image acquired with the Siemens gamma camera. These cold spots were 6, 9 and 12 mm in diameter meaning the clinical system would not pick up an artefact with reduced counts with respect to the background in a clinical image of this size. Identifying features of this size is important to accurately represent the physiological non-uniformities within a

diseased thyroid.

Planar activity quantification of data acquired from a single vial and three vials of ^{131}I was achieved to facilitate calibration of detected counts into an activity. Two sensitivity values (cps/Gbq) for the collimated DEPICT system with ^{131}I were acquired. The first was simply calculated from placing a ^{131}I vial above the detector and measuring the counts per second per unit photopeak activity. The second had appropriate uniformity, scatter and attenuation corrections applied. This factor of 60.87 cps/GBq reconstructed the known activity of the single vial to within 9% and 3% for the three vials. Although these values of activity were well reconstructed this study was carried out without the presence of background activity, which is always present in clinical studies and would complicate activity quantification. Attenuation correction would also be further complicated in a patient due to areas with different attenuation coefficients. Successful 3D reconstruction of a ^{133}Ba vial was achieved using an OSEM reconstruction algorithm, with an investigation performed into optimum iteration number. It was found that 15 iterations with 2 subsets and a threshold of 30 reconstructed counts was optimum for reconstruction of the vial volume in 3D.

An area where CZT may have a significant impact is in ^{227}Th therapy. The Royal Marsden Hospital in Sutton is currently the only UK centre to be taking part in a first-in-human study to evaluate the safety, maximum tolerated dose, pharmacokinetics and recommended dose for further clinical developement with this nuclide [154]. Imaging is extremely difficult due to the poor energy resolution of scintillator gamma cameras and the extremely low administered activities, starting at 1.5 MBq. Complicated deconvolution techniques have to be employed to separate the ^{227}Th photopeak from those arising from ^{223}Ra emissions for activity quantification. ^{227}Th γ-ray spectra acquired with the DEPICT system and a clinical gamma camera have shown the significant impact the superior energy resolution has on resolving photopeaks and will aid dosimetry measurements. Imaging of emerging radionuclides in MRT with DEPICT however, such as ^{227}Th, requires an energy optimised collimator. For γ rays with energy above approximately 140 keV and below 260 keV, a medium-energy collimator is required. The preliminary design of a medium-energy collimator was presented with collimator holes of length $L = 40$ mm, diameter $d = 1$ mm and septal thickess $t = 1$ mm were selected.

8.1 Recommendations

The following recommendations for further work have been made in order to develop a fully clinical DEPICT system:

- Determine if planar activity quantification is feasible with different radionuclides and/or geometries. It is likely this would require calculation of different sensitivity factors because the sensitivity is energy-dependent, due to the energy dependence of interaction mechanisms.
- If personalised dosimetry was implemented and shown some patients would benefit from lower administered activities of ^{131}I, a high-energy collimator with larger or shorter holes to increase the sensitivity may be required as the DEPICT collimator was developed for activities on the order of several GBq. In addition, a CZT crystal that is thicker than 5 mm may be desired for greater detection efficiency if administered activities were lower.
- Produce pixel-matched parallel-hole collimators for a detector system where multiple CZT detectors are tiled up for larger FOV.
- Investigate the feasibility of activity quantification from 3D reconstructed images. This will require implementation of appropriate corrections within the reconstruction algorithm and acquisition of data for calibration from counts to activity.

8.2 Clinical DEPICT Design

A mock-up of a potential clinical DEPICT system is shown in Figure 8.1. The system shown is designed specifically for imaging of the thyroid. The collimator, CZT detector and associated electronics would be encased and positioned onto a rotating arm to acquire multiple images at various angles around the patient. If a clinical DEPICT system was developed, there are currently 23 ^{131}I treatment centres in the UK this could be supplied to. These centres deliver $\sim$2000 ^{131}I treatments and $\sim$100 ^{131}I-mIBG neuroblastoma treatments per year. Whilst this is small compared to EBRT, it has been suggested that ^{131}I-mIBG would be used far more extensively if personalised treatment is adopted and shows patient benefits and reduced costs [155]. More than £5 million per year is currently spent on ^{131}I MRT in the UK.

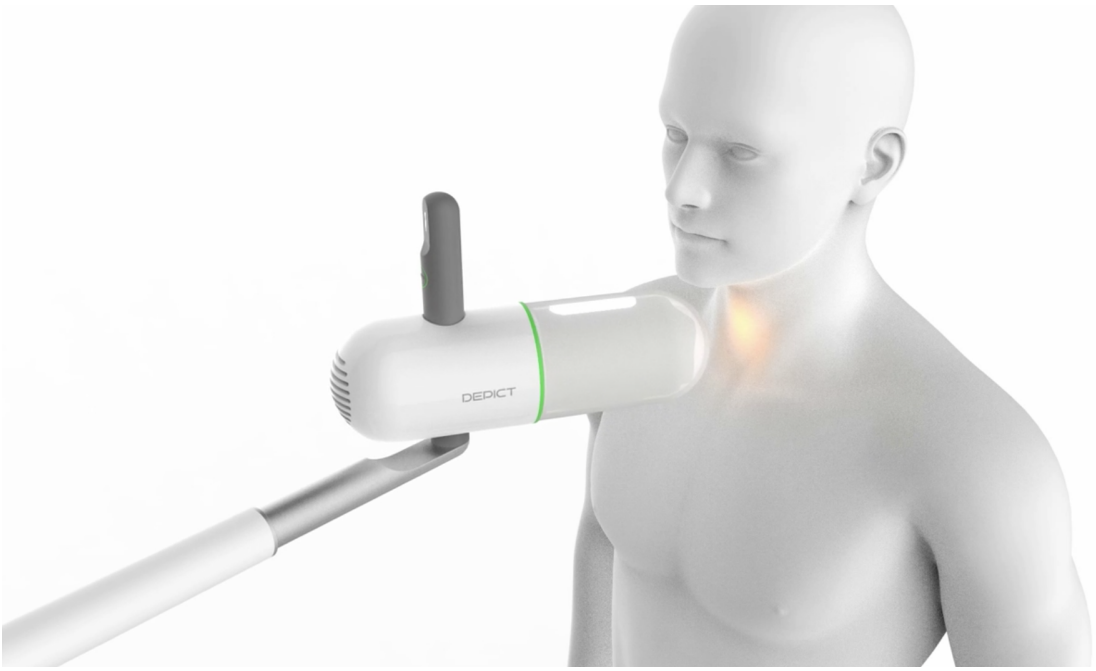

Figure 8.1: Mock-up of potential clinical DEPICT detector system.

Appendix A

Supplementary Material for Chapter 4

A.1 Full ^{131}I Decay Chain

^{131}I decays via the emission of multiple β particles and γ rays to ^{131}Xe, shown in Figure A.1.

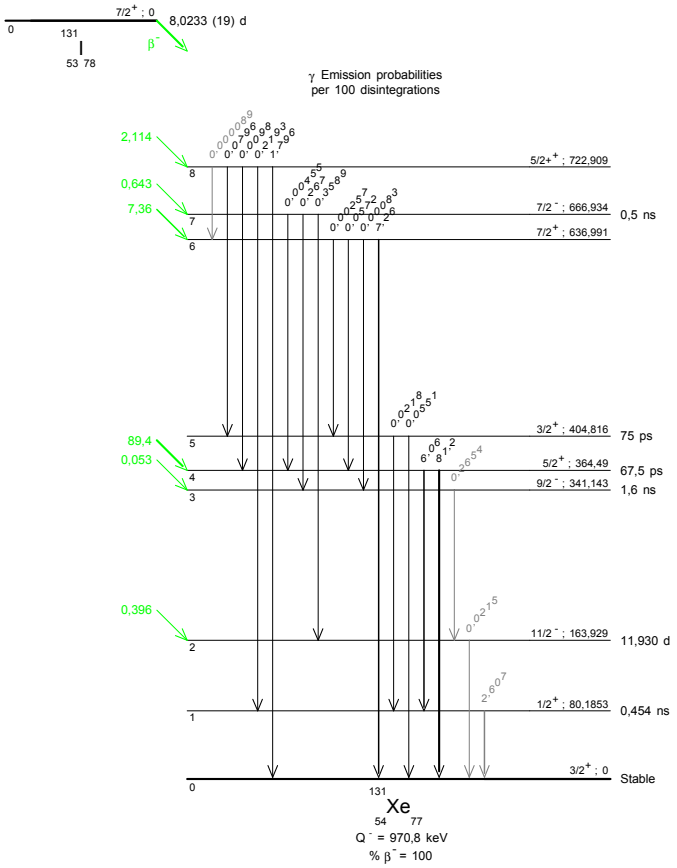

Figure A.1: ^{131}I decay chain to ^{131}Xe. Reproduced from [99].

A.2 Charge Sharing

Pixelated CZT detectors allow increased spatial resolution compared to unsegmented detectors, and this effect improves as the pixel size decreases due to the small pixel effect [61]. However, when the pixel size is decreased to be comparable to the size of the electron charge cloud created when the γ ray interacts, the charge may be shared between multiple pixels or lost in the gap between the pixels and degrade the spatial resolution. Multiple pixel events can occur either due to the charge sharing phenomena, or because the γ ray Compton scatters from one pixel into another, where it deposits its remaining energy. To quantify the amount of charge sharing in the DEPICT CZT detector, the response of the detector as a function of known γ ray position was measured. A 1.64 GBq ^{241}Am source collimated into a 1 mm beam was mounted on a x-y positioning table, controlled by a Velmex VXM Stepper Motor Controller [120], 1.5 cm above the carbon fibre window. The collimated source was moved across the face of the detector in an x-y grid with the step between positions set at 1 mm and data collected for 1 second at each step. For this data collection, the detector readout mode was changed from the 'basic sparsified photon collection' mode used thus far, that only read out triggered channels above a threshold, to 'readout all' mode. This meant that any interaction would trigger the read out of all events in the individual CZT detector module. It was necessary to read out all data from all pixels, in order to observe low energy Compton scattering or charge shared events that occur.

(a) (b)

Figure A.2: Figures (a) and (b) show the collimated ^{241}Am source mounted onto the scanning arm, and placed 1.5 cm above the carbon fibre window.

To discriminate between charge shared and Compton scattered events, the Compton scattering formula given in Equation 3.2 was used. This allowed the range of possible energies of the scattered γ ray E_f and recoil electron to be calculated. Figure A.3 plots the energies of a 59.5 keV γ ray and an electron after Compton scattering, given the incident γ-ray energy $E_0 = 59.5$ keV and the rest mass equivalent energy of the electron $m_0c^2 = 511$ keV.

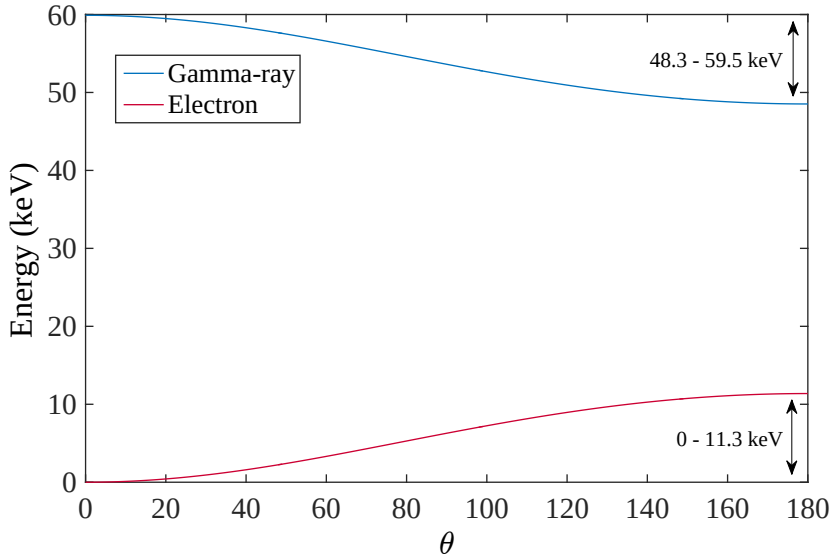

Figure A.3: Energies of a ^{241}Am 59.5 keV γ ray and electron after Compton scattering.

The range of possible energies was calculated to be 0 – 11.3 keV for the energy absorbed by the recoil electron and 48.3 – 59.5 keV for the scattered γ ray, for values of θ between 0 and 180°. Any multi-pixel event with deposited energies of 11.3 - 48.3 keV could then be tagged as a charge shared event, not a Compton scattered event. Since the detector was in readout all mode, all pixels will output a signal corresponding to the collection of real charge or due to electronic or background noise. Figure A.4 shows an example energy spectrum acquired with the ^{241}Am source for this data collection. As a result of the readout mode, a large amount of low energy noise below ∼10 keV is exhibited in the spectrum. This is due to events from all pixels being summed each time a γ ray interacts. Therefore, a threshold of 5 keV was set in post processing when quantifying the charge shared events, to discriminate some noise events. It is known that this threshold will also remove a proportion of Compton scattered and charged shared events, with an energy less than 5 keV.

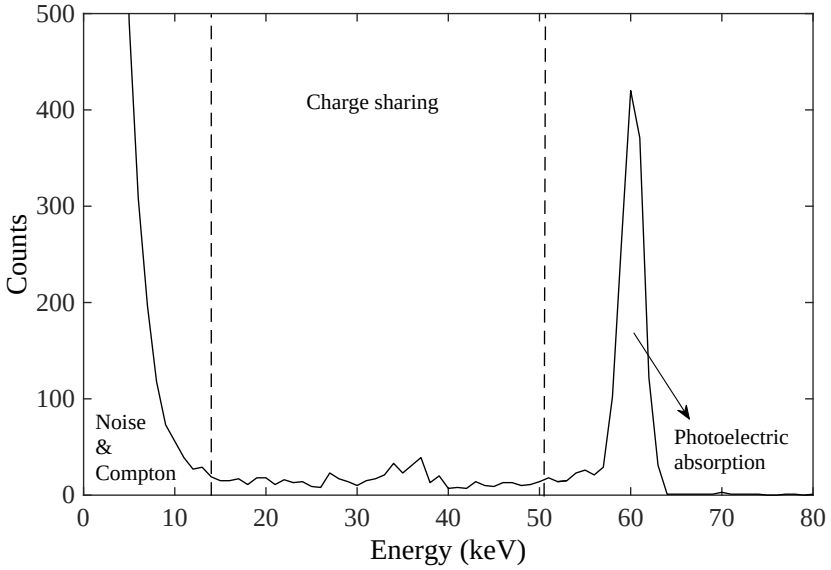

Figure A.4: ^{241}Am energy spectrum acquired in readout all mode, illustrating energy regions corresponding to low energy noise and Compton events, charge shared events and events due to photoelectric absorption.

The final criteria for a multi-pixel event to be classed as a charge shared event is as follows:

- Energy deposited is outside Compton scatter limits defined in Figure A.3.
- Energy is deposited in directly neighbouring pixels, denoted pixel 1 and pixel 2.
- Energy is deposited in the same time stamp.
- Sum of energy deposited in pixel 1 and pixel 2 is less than or equal to 65 keV, accounting for the imperfect detector resolution when detecting photoelectric events.

A 2D energy spectrum is shown in Figure A.5, which depicts the energy recorded in each pixel, for events in which 2 pixels pass the threshold in the same time stamp. The threshold is evident where there are no counts between 0 and 5 keV on each axis. The red areas of 16,000 counts at 59.5 keV for both pixels corresponds to a 59.5 keV γ ray being detected in one pixel in coincidence with noise of energy between $\sim$5 – 8 keV in another pixel.

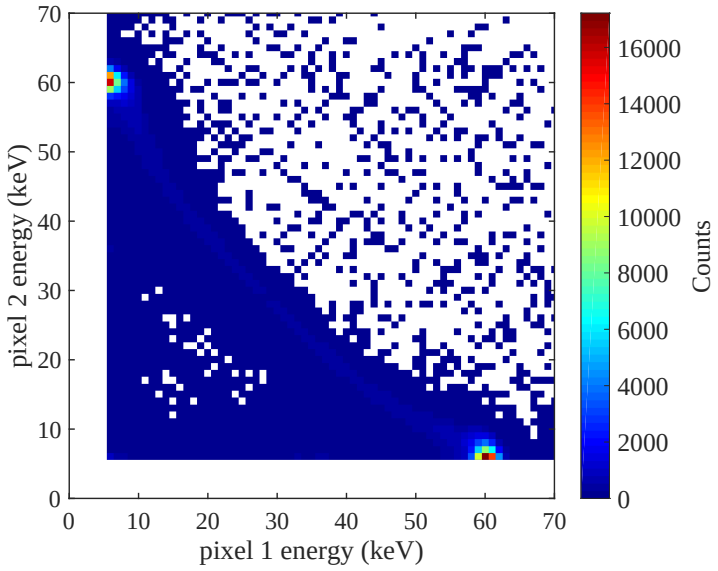

Figure A.5: 2D energy spectrum depicting the energy recorded in each pixel, for events in which 2 pixels pass the threshold in the same time stamp. Only data below 70 keV are included.

Following the application of the charge shared selection criteria, the ratio of charge shared events to all γ-ray interactions for this data was determined to be 0.79%. This is the minimum contribution of charge sharing as some events have been lost with the post processing threshold. This methodology for quantifying charge sharing is not applicable with ^{131}I, as the possible energies for the recoil electron and scattered γ ray are 0 – 214.3 keV and 150.2 – 364.5 keV, respectively. The energies of the electron and scattered γ ray overlap as seen in Figure A.6, therefore the charge shared events cannot be distinguished from Compton scatter events, however it would be expected that the contribution of charge shared events would increase for ^{131}I. The relative cross sections for Compton scattering and photoelectric absorption interactions by a 59.5 keV γ ray are 0.116 cm^2/g (2.13%) and 5.315 cm^2/g (97.86%) respectively, for a total attenuation cross section of 5.431 cm^2. There is a large increase in Compton scattering cross section for ^{131}I 364.5 keV γ ray at 0.083 cm^2/g (72.81%), with 0.031 cm^2/g (27.16 %) for photoelectric absorption for a total attenuation cross section of 0.114 cm^2/g [54].

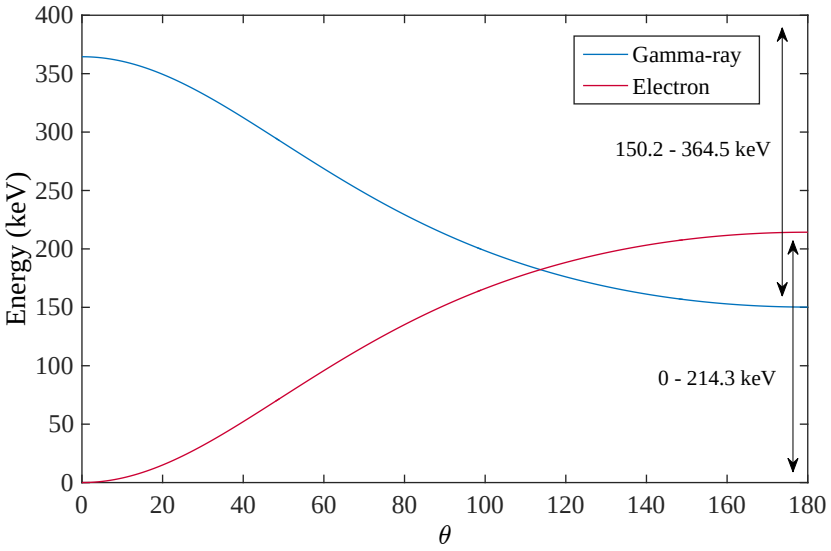

Figure A.6: Energies of a ^{131}I 364.5 keV γ ray and electron after Compton scattering.

Appendix B

Supplementary Material for Chapter 5

B.1 DEPICT Collimator

Figures B.1a - c show CAD drawings of the top, cross section and bottom view of the custom-designed high-energy parallel-hole collimator for DEPICT.

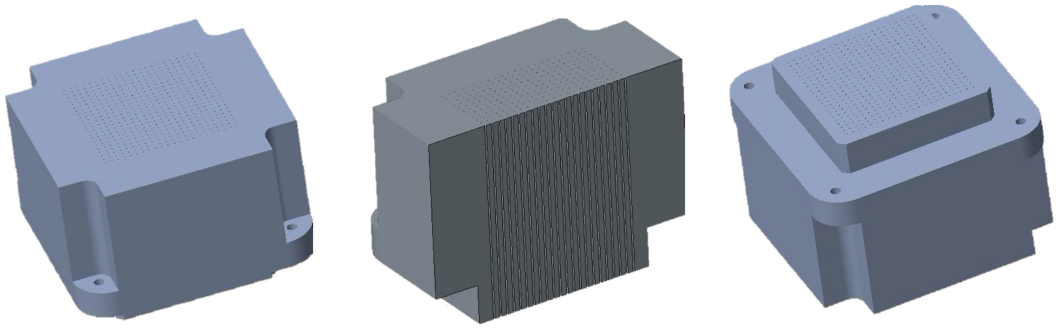

(a) (b) (c)

Figure B.1: (a) Top (b) cross section slice and (c) bottom view of the high-energy parallel-hole tungsten collimator.

B.2 Misalignment of Detector Modules

Figure B.2 shows the four individual CZT detector modules that make up the DMatrix detector. The upper right module appears to be slightly misaligned with respect to the other three modules. As the collimator was designed to have 484 holes, each matched to an individual pixel, this misalignment means the collimator holes do not lie exactly above the detector pixels and cause reduced counts in a portion of the pixels. The physical gap between the modules is also evident.

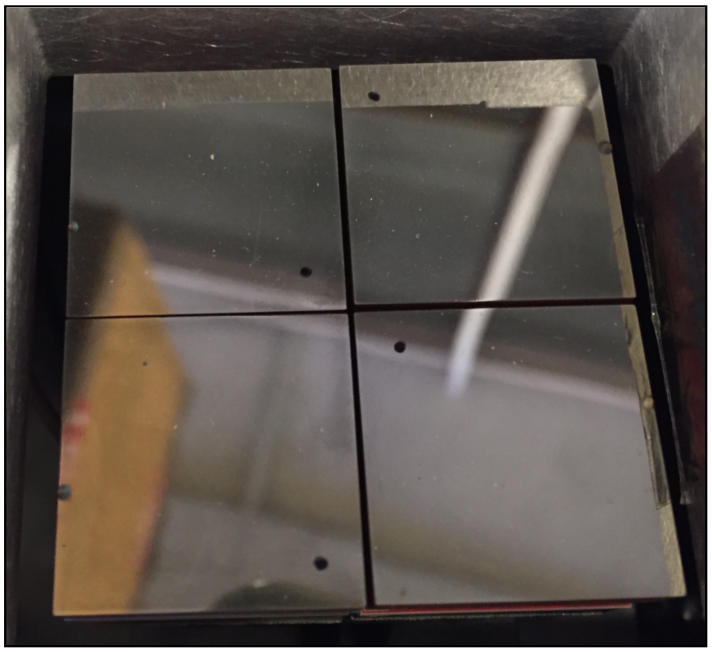

Figure B.2: Slight misalignment of CZT detector modules.

B.3 Uniformity Phantom

Figure B.3 shows a photograph of the uniformity phantom above the uncollimated DEPICT system.

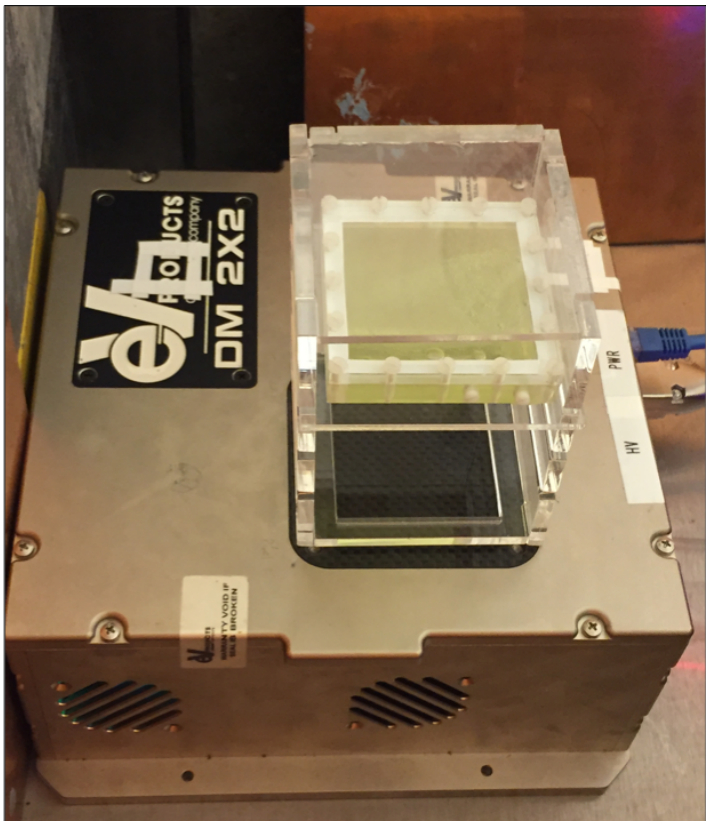

Figure B.3: A photograph of the uniformity phantom above the DEPICT detector.

B.4 Digital Imaging and Communications in Medicine

Digital Imaging and Communications in Medicine (DICOM) files are the standard for the communication and management of medical imaging information and related data. Figure B.4 shows an example of the information that is transmitted alongside medical images. It includes information such as date and time, and smallest and largest pixel values.

MATLAB Command Window 1 of 2

```
>> info_upright_thyroid = dicominfo↙
('/Users/lucymcareavey/Desktop/Marsden_Iodine_Measurements/Marsden_Clinical_Images/I131STATICS/marsden2')

info_upright_thyroid =

                                Filename:↙
'/Users/lucymcareavey/Desktop/Marsden_Iodine_Measurements/Marsden_Clinical_Images/I131STATICS/marsden2'
                             FileModDate: '03-Apr-2017 15:25:48'
                                FileSize: 3153104
                                  Format: 'DICOM'
                           FormatVersion: 3
                                   Width: 512
                                  Height: 512
                                BitDepth: 16
                               ColorType: 'grayscale'
            FileMetaInformationGroupLength: 184
                FileMetaInformationVersion: [2x1 uint8]
                   MediaStorageSOPClassUID: '1.2.840.10008.5.1.4.1.1.20'
                MediaStorageSOPInstanceUID: '1.3.12.2.1107.5.6.1.90239.30830117032810362697300000006'
                          TransferSyntaxUID: '1.2.840.10008.1.2'
                    ImplementationClassUID: '1.2.752.37.0.4.7'
                ImplementationVersionName: 'HERMESGOLD470'
                     SpecificCharacterSet: 'ISO_IR 100'
                                ImageType: 'ORIGINAL\PRIMARY\STATIC\EMISSION'
                             SOPClassUID: '1.2.840.10008.5.1.4.1.1.20'
                          SOPInstanceUID: '1.3.12.2.1107.5.6.1.90239.30830117032810362697300000006'
                               StudyDate: '20170328'
                              SeriesDate: '20170328'
                           AcquisitionDate: '20170328'
                               ContentDate: '20170328'
                               StudyTime: '113604.429000'
                              SeriesTime: '113810.347000'
                           AcquisitionTime: '115023.360000'
                               ContentTime: '115023.360000'
                           AccessionNumber: ''
                                  Modality: 'NM'
                              Manufacturer: 'SIEMENS NM'
                           InstitutionName: 'The Royal Marsden'
                    ReferringPhysicianName: [1x1 struct]
                                StationName: 'RPYSINTEV002'
                          StudyDescription: 'Phantom'
                             SeriesDescription: 'I131 statics'
                                  OperatorName: [1x1 struct]
                     ManufacturerModelName: 'Encore2'
                                PatientName: [1x1 struct]
                                  PatientID: 'jg280317'
                             PatientBirthDate: '19170328'
                                  PatientSex: 'O'
                                  PatientAge: '100Y'
       InterventionDrugInformationSequence: [1x1 struct]
                         CountsAccumulated: []
            AcquisitionTerminationCondition: 'TIME'
                              SoftwareVersion: '10.100.1503.901\12.1.0.19_TT06\syngo CT 2013A>Symbia Intevo 16>10.↙
100.1510.1604>VB10B\VB10B'
                                ProtocolName: '2.0.53169212@'
                       DateOfLastCalibration: '20170328\20170228\20170328\20170228'
                       TimeOfLastCalibration: '093309.000000\164332.000000\093309.000000\164332.000000'
                         ActualFrameDuration: 600001
                             PatientPosition: 'FFS'
                  Private_0019_10xx_Creator: 'SIEMENS MED NM'
                          Private_0019_100f: [4x1 uint8]
                           StudyInstanceUID: '1.3.12.2.1107.5.6.1.90239.30830117032807152094200000004'
                          SeriesInstanceUID: '1.3.12.2.1107.5.6.1.90239.30830117032807152094200000005'
                                    StudyID: '1'
                               SeriesNumber: 1000
                             InstanceNumber: 2
                        FrameOfReferenceUID: '1.3.12.2.1107.5.6.1.90239.30830117032810362697300000002'
                        ImagesInAcquisition: 2
                  PositionReferenceIndicator: 'unknown'
                             SamplesPerPixel: 1
                   PhotometricInterpretation: 'MONOCHROME2'
                              NumberOfFrames: 2
                       FrameIncrementPointer: [84 16 84 32]
                                        Rows: 512
                                     Columns: 512
                               PixelSpacing: [2x1 double]
                             CorrectedImage: 'UNIF\UNIF\UNIF'
                              BitsAllocated: 16
                                 BitsStored: 16
                                    HighBit: 15
                          PixelRepresentation: 0
                        SmallestImagePixelValue: 0
                         LargestImagePixelValue: 5308
                                 WindowCenter: 2654
                                  WindowWidth: 5308
                  Private_0029_10xx_Creator: 'SIEMENS CSA HEADER'
                          Private_0029_1008: [10x1 uint8]
```

```
                        Private_0029_1009: [4x1 uint8]
                        Private_0029_1010: [2097152x1 uint8]
                    RequestingPhysician: [1x1 struct]
            RequestedProcedureDescription: 'Phantom'
                Private_0033_10xx_Creator: 'SIEMENS MED NM'
                        Private_0033_1010: [512x1 uint8]
                        Private_0033_1011: [512x1 uint8]
                        Private_0033_1014: [4x1 uint8]
                        Private_0033_1015: [4x1 uint8]
                        Private_0033_1029: [8x1 uint8]
                        Private_0033_1030: [8x1 uint8]
                        Private_0033_1031: [4x1 uint8]
                        Private_0033_1032: [6x1 uint8]
                        Private_0033_1037: [4x1 uint8]
                Private_0035_10xx_Creator: 'SIEMENS MED NM'
                        Private_0035_1001: [10x1 uint8]
          PerformedProcedureStepStartDate: '20170328'
          PerformedProcedureStepStartTime: '113604.487000'
                PerformedProcedureStepID: 'NM20170328113604'
       PerformedProcedureStepDescription: 'Phantom'
                Private_0043_10xx_Creator: 'SIEMENS MED NM'
                        Private_0043_1003: [1440x1 uint8]
                        Private_0043_1004: [1440x1 uint8]
                    EnergyWindowVector: [2x1 uint16]
                NumberOfEnergyWindows: 1
          EnergyWindowInformationSequence: [1x1 struct]
    RadiopharmaceuticalInformationSequence: [1x1 struct]
                       DetectorVector: [2x1 uint16]
                    NumberOfDetectors: 2
             DetectorInformationSequence: [1x1 struct]
           PatientOrientationCodeSequence: [1x1 struct]
     PatientGantryRelationshipCodeSequence: [1x1 struct]
                Private_0055_10xx_Creator: 'SIEMENS MED NM'
                        Private_0055_107e: [8x1 uint8]
                        Private_0055_107f: [8x1 uint8]
                        Private_0055_10c0: [16x1 uint8]
                Private_0061_10xx_Creator: 'SIEMENS MED NM'
                        Private_0061_100f: [8x1 uint8]
                        Private_0061_1010: [8x1 uint8]
                        Private_0061_101c: [10x1 uint8]
                        Private_0061_1055: [8x1 uint8]
                        Private_0061_1056: [8x1 uint8]
                        Private_0061_1057: [8x1 uint8]
                        Private_0061_1058: [8x1 uint8]
                        Private_0061_1059: [8x1 uint8]
                        Private_0061_105d: [8x1 uint8]
                        Private_0061_105e: [8x1 uint8]
                        Private_0061_105f: [8x1 uint8]
                        Private_0061_1076: [16x1 uint8]
                        Private_0061_1083: [8x1 uint8]
                Private_7fe3_10xx_Creator: 'SIEMENS MED NM'
                        Private_7fe3_1014: [8x1 uint8]
                        Private_7fe3_1015: [8x1 uint8]
                        Private_7fe3_1016: [8x1 uint8]

>> info_upright_thyroid.PixelSpacing

ans =

    0.5994
    0.5994

>>
```

Figure B.4: MATLAB DICOM information of thyroid phantom measurement taken with Siemens gamma camera.

B.5 System Spatial Resolution with Scatter Setup

Figure B.5 shows a photograph of the 1 mm inner diameter line phantoms (capillary tubes) placed on top of a 10 cm acrylic scattering block to measure the system spatial resolution with scatter material.

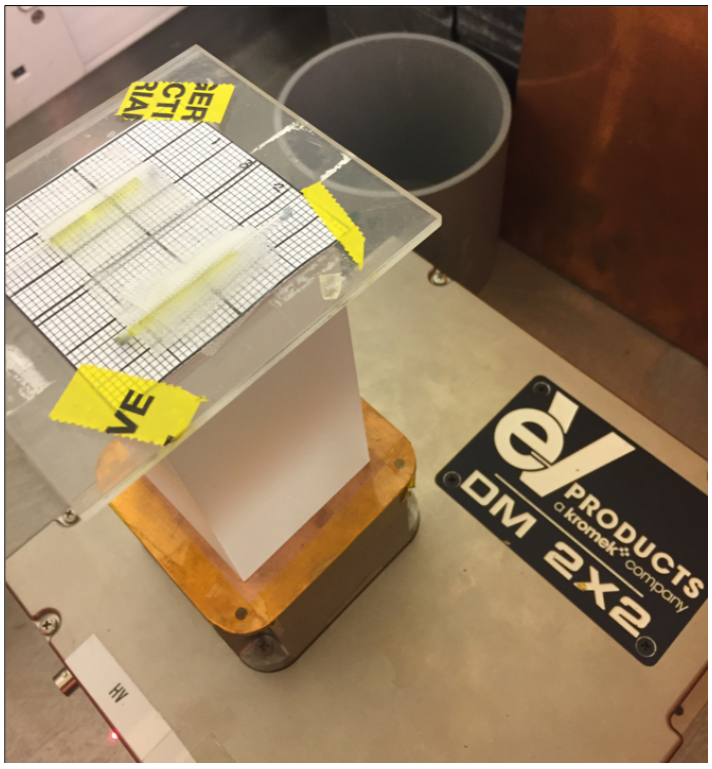

Figure B.5: A photograph showing the DEPICT system with line phantoms placed on top of 10 cm acrylic scattering block.

Bibliography

[1] D. R. McGowan and M. J. Guy. Time to demand dosimetry for molecular radiotherapy? *The British Journal of Radiology*, 88(1047), 2015.

[2] G. D. Flux *et al.* A dose-effect correlation for radioiodine ablation in differentiated thyroid cancer. *European Journal of Nuclear Medicine and Molecular Imaging*, 2010.

[3] G. Sgouros *et al.* Patient-Specific Dosimetry for ^{131}I Thyroid Cancer Therapy Using ^{124}I PET and 3-Dimensional-Internal Dosimetry (3D-ID) Software. *Journal of Nuclear Medicine*, 2004.

[4] GE Healthcare. Discovery NM 530c. `http://www.gehealthcare.co.uk/en-gb/products/categories/molecular_imaging/nuclear_medicine/discovery_nm_530c`.

[5] Spectrum Dynamics Medical. D-SPECT Cardio. `http://www.spectrum-dynamics.com/d-spect-cardio-introduction/`.

[6] SurgicEye. Declipse SPECT Imaging Probe. `https://www.surgiceye.com/for-healthcare-professionals/declipsespect-imaging-probe/`.

[7] CMR Naviscan. LumeGEM Molecular Breast Imaging System. `http://www.cmr-naviscan.com/lumagem/`.

[8] Molecular Dynamics. Whole Body Functional Imaging System. `http://www.molecular-d.com/Product`.

[9] Institute of Medicine and National Research Council. *Advancing Nuclear Medicine Through Innovation.* National Academies Press (US), 2007.

[10] United Nations of Scientific Committee on the Effects of Atomic Radiation. Sources and Effects of Ionizing Radiation - UNSCEAR 2000 Report Vol. I, 2000.

[11] G. Sgouros. Molecular Radiotherapy: Targeting Cancer at the Cellular Level. *Newsletter of the SNM Molecular Imaging Center of Excellence - Journal of Nuclear Medicine*, 2007.

[12] F. F. (Russ) Knapp and A. Dash. *Radiopharmaceuticals for Therapy*. Springer India, 2016.

[13] A. Marin *et al.* Bystander effect and radiotherapy. *Reports of Practical Oncology & Radiotherapy*, 20(1), 2015.

[14] A. I. Kassis. Therapeutic Radionuclides: Biophysical and Radiobiologic Principles. *Seminars in Nuclear Medicine*, 2008.

[15] *Handbook of Radioactivity Analysis*. Elservier, 2012.

[16] O. Sartor *et al.* Targeted use of Alpha Particles: Current Status in Cancer Therapeutics. *Journal of Nuclear Medicine and Radiation Therapy*, 3(4), 2012.

[17] European Medicines Agency. `https://www.ema.europa.eu/en/medicines`.

[18] S. G. DuBois and K. K. Matthay. Radiolabeled metaiodobenzylguanidine for the treatment of neuroblastoma. *Nuclear Medicine and Biology*, 35, Supplement 1:S35 – S48, 2008.

[19] ClinicalTrials.gov. FDA approves lutetium Lu-177 dotatate for treatment of GEP-NETs. `https://www.fda.gov/drugs/informationondrugs/approveddrugs/ucm594105.htm`.

[20] Endocyte. Study of 177Lu-PSMA-617 In Metastatic Castrate-Resistant Prostate Cancer (VISION). `https://clinicaltrials.gov/ct2/show/NCT03511664`.

[21] C. Jago and A. Al-Shamahi. Spotlight on Radiotherapeutics. *A Thomson Reuters Pharma Matters Report*, 2013.

[22] X. Chen and S. T. C. Wong. *Cancer Theranostics*, pages 285–325. Elsevier Inc., 2014.

[23] National Nuclear Data Centre. NuDat 2.7. `https://www.nndc.bnl.gov/nudat2/chartNuc.jsp`.

[24] C. Alberti. From molecular imaging in preclinical/clinical oncology to theranostic applications in targeted tumor therapy. *European Review for Medical and Pharmacological Sciences*, 16(14):1925 – 1933, 2012.

[25] C-H. Yeong *et al.* Therapeutic radionuclides in nuclear medicine: current and future prospects. *Journal of Zhejiany University Science B*, 15(10), 2014.

[26] U. Eberlein, M. Cremonesi, and M. Lassmann. Individualized dosimetry for theranostics: Necessary, nice to have, or counterproductive. *Journal of Nuclear Medicine*, 58(2), 2017.

[27] S. Vinjamuri *et al.* Peptide receptor radionuclide therapy with 90Y-DOTATATE/90Y-DOTATOC in patients with progressive metastatic neuroendocrine tumours: assessment of response, survival and toxicity. *British Journal of Cancer*, 2013.

[28] C. T. Sawin and D. V. Becker. Radioiodine and the Treatment of Hyperthyroididm: The Early History. *Thyroid*, 7(2), 1997.

[29] RADAR - the RAdiation Dose Assessment Resource. The Decay Data. `http://www.doseinfo-radar.com/RADARDecay.html`.

[30] K. S. Gleisner *et al.* Variations in the practice of molecular radiotherapy and implementation of dosimetry: results from a European survey. *European Jounral of Nuclear Medicine and Molecular imaging Physics*, 2017.

[31] E. B. Silberstein *et al.* The SNM Practice Guideline for Therapy of Thyroid Disease with ^{131}I 3.0. *Journal of Nuclear Medicine*, July 2012.

[32] D. A. Meier *et al.* Procedure Guideline for Therapy of Thyroid Disease with ^{131}Iodine. *Journal of Nuclear Medicine*, 43:856–861, 2002.

[33] M. Luster *et al.* Guidelines for radioiodine therapy of differentiated thyroid cancer. *European Journal of Nuclear Medicine and Molecular Imaging*, 2008.

[34] M. Ljungberg and K. S. Gleisner. Personalized Dosimetry for Radionuclide Therapy Using Molecular Imaging Tools. *Biomedicines*, 4(25), 2016.

[35] R. Loevinger and M. Berman. A revised schema for calculating the absorbed dose from biologically distributed radionuclides. *MIRD Pamphlet No. 1 Revised. New York: The Society of Nuclear Medicine*, 1976.

[36] R. Loevinger and T.F. Budinger. MIRD Primer for absorbed dose calculations. *Revised Edition. New York: The Society of Nuclear Medicine*, 1991.

[37] J. A. Siegel *et al.* MIRD Pamphlet No. 16: Techniques for Quantitative Radiopharmaceutical Biodistribution Data Acquisition and Analysis for Use in Human Radiation Dose Estimates. *Journal of Nuclear Medicine*, 40(2), 1999.

[38] W. S. Snyder *et al.* MIRD Pamphlet No. 11 "S" Absorbed Dose per Unit Cumulated Activity for Selected Radionuclides and Organs. *Society of Nuclear Medicine*, 1975.

[39] W. E. Bolch *et al.* MIRD Pamphlet No. 17: The Dosimetry of Nonuniform Activity Distributions - Radionuclide S Values at the Voxel Level. *Journal of Nuclear Medicine*, pages 11S – 36S, 1998.

[40] W. S. Snyder *et al.* MIRD Pamphlet No. 5, Revised: Estimates of Specific Absorbed Fractions for Photon Sources Uniformity Distributed in Various Organ of a Heterogeneous Phantom. *Society of Nuclear Medicine*, 1978.

[41] Y. Hum Na *et al.* Deformable adult human phantoms for radiation protection dosimetry: Anthropomophic data representing size distributions of adult worker populations and software algorithms. *Physics in Medicine and Biology*, 2010.

[42] EURAMET. Metrology for clinical implementation of dosimetry in molecular radiotherapy. Technical Report SRT-h18, EMPIR Call 2015 - Health, SI, Normative and Research Potential, 2015.

[43] L. Bodei *et al.* Receptor radionuclide therapy with 90Y-[DOTA]0-Tyr3-octreotide (90Y-DOTATOC) in neuroendocrine tumours. *European Journal of Nuclear Medicine and Molecular Imaging*, 31(7):1038–1046, 2004.

[44] W. Rontgen. On a new kind of rays. *Science*, 3(59):227 – 231, 1896.

[45] H. O. Anger. Use of a gamma-ray pinhole camera for in vivo studies. *Nature*, 170(4318), 1952.

[46] J. A. Patton and T. G. Turkington. SPECT/CT Physical Principles and Attenuation Correction. *Journal of Nuclear Medicine Technology*, 36(1), 2008.

[47] G. F. Knoll *et al. Radiation Detection and Measurement Fourth Edition.* John Wiley & Sons, Inc., 2010.

[48] P. F. Sharp, H. G. Gemmell, and A. D. Murray. *Practical Nuclear Medicine*, chapter Nuclear Medicine Imaging. Springer, 2005.

[49] Siemens System Specfications. `https://3.imimg.com/data3/AC/PC/MY-13438971/gamma-camera.pdf`.

[50] GE Healthcare. *Infinia - 3/8" or 1" Free-Geometry Dual-Detector Cameras Optional Hawkeye Hybrid NM/CT*, 2006.

[51] D. Hart and B. F. Wall. A Survey of Nuclear Medicine in the UK in 2003/4. *Health Protection Agency*, 2005.

[52] Administration of Radioactive Substances Advisory Committee (ARSAC). Notes for Guidance on the Clinical Administration of Radiopharmaceuticals and Use of Sealed Radioactive Sources. 2006.

[53] M. Ljungberg *et al.* MIRD Pamphlet No. 26: Joint EANM/MIRD Guidelines for Quantitative ^{177}Lu SPECT Applied for Dosimetry of Radiopharmaceutical Therapy. *Journal of Nuclear Medicine*, 2016.

[54] NIST. XCOM: Photon Cross Sections Database. `http://physics.nist.gov/PhysRefData/Xcom/Text/XCOM.html`.

[55] J. A. Sorenson S. R. Cherry and M. E. Phelps. *Physics in Nuclear Medicine.* Elsevier, Fourth edition, 2012.

[56] D. Darambara and A. Todd-Pokropek. Solid state detectors in nuclear medicine. 46:3–7, 04 2002.

[57] L. J. Harkness *et al.* Semiconductor detectors for compton imaging in nuclear medicine. *Journal of Instrumentation*, 7(01):C01004, 2012.

[58] R. P. Parker. Semiconductor nuclear radiation detectors. *Physics in Medicine and Biology*, 15(4):605, 1970.

[59] H. Bradford Barber. Applications of semiconductor detectors to nuclear medicine. *Nuclear Instruments and Methods in Physics Research Section A: Accelerators, Spectrometers, Detectors and Associated Equipment*, 436(1):102 – 110, 1999.

[60] K. Iniewski *et al.* CZT detector technology for medical imaging. *Journal of Instrumentation*, 2014.

[61] Z. He. Review of the Shockley - Ramo theorem and its application in semiconductor gamma-ray detectors. *Nuclear Instruments and Methods in Physics Research A*, 463(3), 2001.

[62] S. J. Bell *et al.* Performance comparison of small-pixel CdZnTe radiation detectors with gold contacts formed by sputter and electroless deposition. *Journal of Instrumentation*, 12, 2017.

[63] Y. Z. Yin *et al.* Charge Sharing Effect on 600 μm Pitch Pixelated CZT Detector for Imaging Applications. *Chinese Physics C*, 38(11), 2014.

[64] F. *et al.* Zhang. Characterization of the H3D ASIC Readout System and 6.0 cm^3 3D Position Sensitive CdZnTe Detectors. *IEEE Transactions on Nuclear Science*, 59(1), February 2012.

[65] P. Rehak. Silicon Radiation Detectors. *IEEE Transactions on Nuclear Science*, 51(5), October 2004.

[66] W. Akutagawa, K. Zanio, and J. W. Mayer. CdTe as a gamma detector. *Nuclear Instruments and Methods*, 55:383–385, 1967.

[67] C. Scheiber and J. Chambron. CdTe detectors in medicine: a review of current applications and future perspectives. *Nuclear Instruments and Methods in Physics Research A*, 1992.

[68] T. Takahashi and S. Watanabe. Recent Progress in CdTe and CdZnTe Detectors. *IEEE Transactions on Nuclear Science*, 2000.

[69] A. Owens and A. Peacock. Compound semiconductor radiation detectors. *Nuclear Instruments and Methods in Physics Research A*, 531(1):18–37, 2004.

[70] S. *et al.* Del Sordo. Progress in the Development of CdTe and CdZnTe Semiconductor Radiation Detectors for Astrophysical and Medical Applications. *Sensors*, 9(5):3491, 2009.

[71] G. S. Ohm. *Die Galvanische Kette: Mathematisch Bearbeitet*. Berlin: T. H. Riemann, 1827.

[72] M. N. Wernick and J. N. Aarsvold, editors. *Emission Tomography The Fundamentals of PET and SPECT*. Elsevier Academic Press, 2004.

[73] G. De Geronimo *et al.* Readout ASIC for 3D Position-Sensitive Detectors. *IEEE Transactions on Nuclear Science*, 55(3), 2008.

[74] P. Coleman-Smith L. L. Jones, I. Lazarus. A Readout ASIC for CZT Detectors. *Topical Workshop on Electronics for Particle Physics*, 2008.

[75] Y. K. *et al.* Dewaraja. MIRD Pamphlet No. 24: Guidlines for Quantitative ^{131}I SPECT in Dosimetry Applications. *Journal of Nuclear Medicine*, 54:2182–2188, 2013.

[76] O. Schober and B. Riemann. *Molecular Imaging in Oncology*, volume 187, chapter Quantitative SPECT/CT. Springer, 2013.

[77] United States Department of Energy Technical Information Center. *Bibliography on Nuclear Medicine*. 1978.

[78] International Atomic Energy Agency. Quantitative Nuclear Medicine Imaging: Concepts, Requirements and Method. *IAEA Human Heallth Reports No. 9*, 2014.

[79] M. S. Rosenthal *et al.* Quantitative SPECT Imaging: A Review and Recommendations by the Focus Committee of the Society of Nuclear Medicine Computer and Instrumentation Council. *Journal of Nuclear Medicine*, 36(8):1489–1513, 1995.

[80] Y. K. Dewaraja, M. Ljungberg, and K. Koral. Effects of dead time and pile up on quantitative SPECT for I-131 dosimetric studies. *Journal of Nuclear Medicine*, 49, 2008.

[81] Y. K. *et al.* Dewaraja. MIRD Pamphlet No. 23: Quantitative SPECT for Patient-Specific 3-Dimensional Dosimetry in Internal Radionuclide Therapy. *Journal of Nuclear Medicine*, 53(8):1310–1325, 2012.

[82] Y. K. *et al.* Dewaraja. Use of Integrated SPECT/CT Imaging for Tumour Dosimetry in I-131 Radioimmunotherapy: A Pilot Patient Study. *Cancer Biotherapy and Radiopharmaceuticals*, 24(4):417–426, 2009.

[83] H. M. Hudson and R. S. Larkin. Accelerated image reconstruction using ordered subsets of projection data. *IEEE Transactions on Medical Imaging*, 13:601–609, 1994.

[84] L. A. Shepp and Y. Vardi. Maximum likelihood reconstruction for emission tomography. *IEEE Transactions on Medical Imaging*, pages 113–122, 1982.

[85] M. Lyra and A. Ploussi. Filtering in SPECT Image Reconstruction. *International Journal of Biomedical Imaging*, 2011.

[86] U. J. Schoepf L. L. Geyer and F. G. Meinel. State of the Art: Iterative CT Reconstruction Techniques. *Radiology*, 276(2), 2015.

[87] J. Ramez *et al. Proceedings of the 8th International Conference on Computational Science, Part I*, chapter Effective Emission Tomography Image Reconstruction Algorithms for SPECT Data, pages 741–748. ICCS '08. Springer-Verlag, 2008.

[88] J. C. Dickson *et al.* The impact of reconstruction method on the quantification of DaTSCAN images. *European Journal of Nuclear Medicine and Molecular Imaging*, 37(1):23–35, 2010.

[89] C. Marcassa and O. Zoccarato. Advances in image reconstruction software in nuclear cardiology: Is all that glitters gold. *Journal of Nuclear Cardiology*, 24(1):142–144, 2016.

[90] Douglas J. Wagenaar *et al.* Advantages of semiconductor CZT for medical imaging. *Proceedings of SPIE - The International Society for Optical Engineering*, 6707, 2007.

[91] Y. Takahashi *et al. Annals of Nuclear Medicine*, 27(1), 2013.

[92] Kromek. DMatrix-Nuclear Imager Gamma Spectroscopy Detector. `http://www.kromek.com/index.php/medical/all-medical-products/dmatrix`, .

[93] E. Vernon *et al.* ASIC for High Rate 3D Position Sensitive Detectors. *IEEE Transactions on Nuclear Science*, 57(3), 2010.

[94] MATLAB. `https://uk.mathworks.com/products/matlab.html`.

[95] J. C. Kim *et al.* Charge sharing in common-grid pixelated CdZnTe detectors. *Nuclear Instruments and Methods in Physics Research A*, 2011.

[96] Q. Zhang *et al.* Progress in the Development of CdZnTe Unipolar Detectors for Different Anode Geometries and Data Corrections. *Sensors*, 2013.

[97] A. Shor *et al.* Gamma spectroscopy with pixelated cdznte detectors. *IEEE Transactions on Nuclear Science*, 51(3), 2004.

[98] D. C. Radford. Radware software package, 2000.

[99] M.-M Bé *et al.* Table of radionuclides, Vol.1 - A = 1 to 150. *Monographie BIPM-5 Bureau International des Poids et Mesures*, 2004.

[100] M.-M Bé *et al.* Table of radionuclides, Vol.2 - A = 151 to 242. *Monographie BIPM-5 Bureau International des Poids et Mesures*, 2004.

[101] N. J. Zaluzec. Analytical formulae for calculations of x-ray detector solid angles in the scanning and scanning/transmission analytical electron microscope. *Microscopy and Microanalysis*, 20(4), 2014.

[102] GAMOS. Geant4-based Architecture for Medicine-Oriented Simulations. `http://fismed.ciemat.es/GAMOS/gamos.php`.

[103] Wolfmet of M&I Materials Ltd. Excellence in tungsten. `https://www.mimaterials.com/`.

[104] Wolfmet a product of M&I Materials. Innovation for Personalised Cancer Treatment with Wolfmet 3D Tungsten Collimator and DEPICT Project. `https://www.wolfmet.com/wp-content/uploads/2017/07/Wolfmet-3D-and-DEPICT-Case-Study-1.pdf`, 2017.

[105] D. Autret *et al.* Impact of collimator characteristics on quantitative I-131 imaging. *European Journal of Nuclear Medicine and Molecular Imaging*, 32, 2005.

[106] J. Gear and G. D. Flux. Design Optimisation of 3D Printed Parallel-Hole Tungsten Collimators for High activity I-131 Imaging. *European Journal of Nuclear Medicine and Molecular Imaging*, 43(1), 2016.

[107] J. Gear *et al.* Characterisation of the attenuation properties of 3D-printed tungsten for use in gamma camera collimation. *European Journal of Nuclear Medicine and Molecular Imaging Physics*, 6(6), 2019.

[108] The Association of Electrical Equipment and Medical Imaging Manufacturers. NEMA NU 1-2012 Performance Measurements of Gamma Cameras. *National Electrical Manufacturers Association*, 2012.

[109] Y.Yamashita *et al.* Measurement of effective atomic numbers using energy-resolved computed tomography. *Journal of Nuclear Science and Technology*, 51(10):1256–1263, 2014.

[110] Biodex. Jaszczak SPECT Phantom. `http://www.biodex.com/nuclear-medicine/products/pet-positron-emission-tomography/pet-phantoms/jaszczak-spect-phantom`.

[111] DICOM Digital Imaging and Communications in Medicine. `https://www.dicomstandard.org/`.

[112] OsiriX. OsiriX DICOM Viewer. `https://www.osirix-viewer.com/`.

[113] M. W. Groch and W. D. Erwin. SPECT in the Year 2000: Basic Principles. *Journal of Nuclear Medicine Technology*, 28(4), 2000.

[114] A. Formiconi, D. Gunter, and E. Vanzi. A design strategy for suppression of hole-pattern artifacts in high-energy collimators. *IEEE Transactions on Nuclear Science*, 53:1179 – 1187, 2006.

[115] Y. K. Dewaraja, M. Ljungberg, and K. F. Koral. Accuracy of ^{131}I Tumor Quantification in Radioimmunotherapy Using SPECT Imaging with an Ultra-High-Energy Collimator: Monte Carlo Study. *Journal of Nuclear Medicine*, 2000.

[116] Marconi Medical System Inc. Picker thyroid phantom part 3602, 35 cc volume.

[117] G. Popovenius and J. Jonklaas. Thyroid Nodules. *Medical Clinics of North America*, 2012.

[118] Y. Li *et al.* Quantification of radioactivity by planar gamma camera iamges, a promoted method of absorbed dose in the thyroid after iodine-131 treatment. *Scientific Reports*, 8(10167), 2018.

[119] High Technology Sources Limited. `http://hightechsource.co.uk/`.

[120] Velmex Inc. Velmex VXM Controllers Control Motion on Multiples Axis. `https://www.velmex.com/Products/Controls/VXM_Controller.html`.

[121] K. Ogawa *et al.* A practical method for position-dependent compton-scatter correction in single photon emission ct. *IEEE Transactions on Medical Imaging*, 10(3):408 – 412, 1991.

[122] K. F. Koral. SPECT dual-energy-window Compton correction: scatter multipler required for quantification. *Journal of Nuclear Medicine*, 31(1), 1990.

[123] Martinos Center for Biomedical Imaging Massachusetts General Hospital (MGH) Harvard University. NiftyRec 2.0 Tomography Toolbox. `http://niftyrec.scienceontheweb.net/wordpress/`.

[124] Velmex Inc. Rotary Tables. `https://www.velmex.com/Products/Rotary_Tables/index.html`.

[125] M. Kalke and S. Siltanen. Sinogram Interpolation Method for Sparse-Angle Tomography. *Applied Mathematics*, 5(3), 2014.

[126] Mark Taylor. TOPCAT Tool for OPerations on Catalogues And Tables. `http://www.star.bris.ac.uk/~mbt/topcat/`.

[127] D. G. Politte and D. L. Snyder. The use of constraints to eliminate artifacts in maximum-likelihood image estimation for emission tomography. *IEEE Transactions on Nuclear Science*, 1988.

[128] E. Grassi *et al.* Impact of a commercial 3D OSEM reconstruction algorithm on the 177Lu activity quantification of SPECT/CT imaging in a Molecular Radiotherapy trial. *Radiology and Diagnostic Imaging*, 1, 2017.

[129] A. Gaitanis *et al.* PET image reconstruction: A stopping rule for the MLEM algorithm based on properties of the updating coefficients. *Computerized Medical Imaging and Graphics*, 2010.

[130] A. Rahmim and J. Tang. Noise propagation in resolution modeled PET imaging and its impact on detectability. *Physics in Medicine and Biology*, 58, 2013.

[131] G. D. Flux *et al.* Opportunities for research in molecular radiotherapy. *The British Journal of Radiology*, 97(1071), 2017.

[132] B. Rojas *et al.* Eight years of growth and change in UK molecular radiotherapy with implications for the future: Internal Dosimetry Users Group survey results from 2007 to 2015. *Nuclear Medicine Communications*, 38:201–204, 2015.

[133] National Institue of Health and Care Excellence. Lutetium (177Lu) oxodotreotide for treating unresectable or metastatic neuroendocrine tumours. *Technology Appraisal Guidance*, 2018.

[134] C. Lozza *et al.* Peptides in Receptor-Mediated Radiotherapy: From Design to the Clinical Application in Cancers. *Frontiers in Oncology*, 2013.

[135] J. J. Zaknun *et al.* The joint IAEA, EANM and SNMMI practical guidance on peptide receptor radionuclide therapy (PRRNT) in neuroendocrine tumours. *European Journal of Nuclear Medicine and Molecular Imaging*, 2013.

[136] J. Kunikowska *et al.* Clinical results of radionuclide therapy of neuroendocrine tumours with ^{90}y-dotatate and tandem ^{90}y/^{177}lu-dotatate: which is a better therapy option? *European Journal of Nuclear Medicine and Molecular Imaging*, 38(10), 2011.

[137] C. L. Wright *et al.* Theranostic Imaging of Yttrium-90. *Biomed Research International*, 2015.

[138] M. G. Stabin *et al.* Bremsstrahlung Radiation Dose in Yttrium-90 Therapy Applications. *Journal of Nuclear Medicine*, 1994.

[139] Cancer Research UK. Prostate cancer incidence statistics. `https://www.cancerresearchuk.org/health-professional/cancer-statistics/statistics-by-cancer-type/prostate-cancer/incidence#heading-Five`.

[140] C. Parker *et al.* Alpha emitter radium-223 and survival in metastatic prostate cancer. *The New England Journal of Medicine*, 369:213 – 223, 2013.

[141] European Medicine Agency. Radium 223 Xofigo (223 Ra dichloride) summary of product characteristics. `https://www.ema.europa.eu/documents/product-information/xofigo-epar-product-information_en.pdf`.

[142] G. D. Flux. Imaging and dosimetry for radium-223: the potential for personalized treatment. *The British Journal of Radiology*, 90(1077), 2017.

[143] D. E. Cullen *et al.* Tables and Graphs of Photo-Interaction Cross Section from 10 eV to 100 GeV Derived from the LLNL Evaluated Photon Data Library (EPDL), UCRL-50400, Part A: Z = 1 to 50, Part B Z = 51 to 100. *Lawrence Livermore National Laboratory*, 1989.

[144] D. E. Cullen. EPDL97: the Evaluated Photon Data Library, "97 Version". *Lawrence Livermore National Laboratory*, 1997.

[145] S. T. Perkins D. E. Cullen and S. M. Seltzer. Tables and Graphs of Electron Interaction Cross Sections 10 eV to 100 GeV Derived from the LLNL Evaluated Electron Data Library (EEDL) Z = 1 - 100. *Lawrence Livermore National Laboratory*, 1991.

[146] D. R. White *et al.* Tissue substitutes in radiation dosimetry and measurement report 44. *Journal of the International Commission on Radiation Units and Measurements*, 23, 1989.

[147] ROOT. Data Analysis Framework. `https://root.cern.ch/`.

[148] V. Tunninen *et al.* ^{99m}Tc-Sestamibi/^{123}I Subtraction SPECT/CT in Parathyroid Scintigraphy: Is additional Pinhole Imaging Useful? *International Journal of Molecular Imaging*, 2017.

[149] A. P. Robinson. The influence of triple energy window scatter correction on activity quantification for ^{177}Lu molecular radiotherapy. *Physics in Medicine & Biology*, 61, 2016.

[150] A. Patel. An Experimental Investigation to Assess the Feasibility of Imaging Medical

Radioisotopes with the ProSPECTus Compton Camera. *PhD Thesis, University of Liverpool*, 2016.

[151] G. El Fakhri *et al.* Absolute activity quantification in simultaneous ^{123}I/^{99m}Tc brain SPECT. *Journal of Nuclear Medicine*, 42(2), 2001.

[152] J. Ouyang *et al.* Quantitative simultaneous ^{99m}Tc/^{123}I cardiac SPECT using MC-JOSEM. *Medical Physics*, 36(2), 2009.

[153] L. Strigari *et al.* The evidence base for the use of internal dosimetry in the clinical practice of molecular radiotherapy. *European Journal of Nuclear Medicine and Molecular Imaging*, 2014.

[154] U.S. National Library of Medicine. First-in-human Study of BAY2287411 Injection, a Thorium-227 Labeled Antibody-chelator Conjugate, in Patients With Tumors Known to Express Mesothelin. `https://clinicaltrials.gov/ct2/show/NCT03507452`.

[155] S. L. George *et al.* Individualised ^{131}I-mIBG therapy in the management of refractory and relapsed neuroblastoma. *Nuclear Medicine Communications*, 37(5), 2016.